Kondo Collapse and Revival by Pulsed Light

Dissertation
zur
Erlangung des Doktorgrades (Dr. rer. nat.)
der
Mathematisch-Naturwissenschaftlichen Fakultät
der
Rheinischen Friedrich-Wilhelms-Universität Bonn

von
Francisco Costa Meirinhos
aus
Porto, Portugal

Bonn, February 2023

Angefertigt mit Genehmigung der Mathematisch-Naturwissenschaftlichen Fakultät der Rheinischen Friedrich-Wilhelms-Universität Bonn

1. Gutachter:	Prof. Dr. Johann Kroha
2. Gutachter:	Prof. Dr. David J. Luitz
Tag der Promotion:	29.06.2023
Erscheinungsjahr:	2024

Abstract

The search and characterisation of new quantum phases of matter has recently been intensified by the application of terahertz (THz) spectroscopy in the time domain to heavy-fermion systems. It was experimentally shown that a single-cycle THz pulse disrupts the strongly interacting Kondo regime of heavy-fermion compounds such as $CeCu_{6-x}Au_x$, which recover after a characteristic delay time, accompanied by the emission of a temporally confined THz echo. The transient nature of such non-equilibrium dynamics leads to new and exciting many-body physics, raising questions about the established properties of quasiparticles.

In this thesis, the theoretical description of these heavy-fermion non-equilibrium dynamics is developed. The electronic part of the system is captured by an Anderson lattice model and described by non-equilibrium dynamical mean-field theory and the non-crossing approximation. Such heavy-fermion systems already constitute a challenging problem in thermal equilibrium due to the electronic and spin degrees of freedom being fundamentally entangled. The non-equilibrium drive is a quantised Gaussian pulse of THz light coupled to the heavy-fermion system by a dipole interaction. The release of excess energy during the relaxation dynamics following excitation is treated beyond the typical Markovian master equation, with relaxation to ambient temperature possible via radiative recombination and electronic particle-exchange channels. The long-time dynamics associated with the driven-dissipative strongly-interacting lattice system are resolved at the level of two-point functions via an adaptive algorithm, and temporal aspects regarding the revival of the Kondo regime following its destruction by the pulse of radiation are discussed.

Acknowledgements

A doctoral degree does not happen in a vacuum, and this work is the fruit of the involvement of numerous people with whom I was incredibly fortunate to have crossed paths.

First and foremost, I would like to thank my supervisor, *the* Hans, for the opportunity of working on such fascinating and challenging topics. I am particularly thankful for the great freedom I was entrusted with, as well as his consistent support, insight, and patience in guiding our research route.

Secondly, I want to thank my fellow *enslaved-by-the-slaves* comrades, Tim and Micha, for all the countless hours of discussions, puzzlement and dismay. In part, this work is as much mine as theirs. I must also extend my gratitude to my office mate Michael, who had to put up with my jeremiads and lent a hand and more in the very last stretch. And also to Marvin, dragged as well into so many *spurious* problems, and to the rest of our group, that always made our work environment such a bubbly and exciting place.

Many thanks to the *old Gods*, Lai for opening the door to my short and fruitful stay at Fudan University, warm-welcomed and made possible by prof. Xiaopeng Li, and Ammar for questioning the allegedly obvious. A word of appreciation as well to the holy trinity Weiß-Zündorf-Wißkirchen of the Physikalisches Institut, who made sure everything always ran smoothly, and to Prof. David Luitz for affably accepting to be on my thesis committee.

Lastly, a big shout out to my partner in crime, Ghassan, and so many friends who were a vital source of sanity and festivity. To all my educators, and to my brother, parents and Mariana, for all the love and everything else.

Contents

Introduction

> Why would anyone still want to study a physical phenomenon that was discovered in the 1930s, explained in the 1960s and has been the subject of numerous reviews since the 1970s?

The introspective question [1] posed in the 2000s regarding the *revival* of the Kondo effect in the field of condensed-matter physics is, two decades later, still remarkably contemporary. Despite the physics behind the single-impurity Kondo effect being well understood, the ubiquitousness of the effect in strongly interacting matter provides a fertile ground of "irresistible" [2] rich physics, which still poses many challenges for theoreticians and experimentalists alike.

The *Kondo effect* first revealed itself in measurements of the resistivity of (impure) gold, which was found [3] to increase at very low temperatures. Even though this perplexing observation was linked to the concentration of impurities in the material, it was at odds with the then-existing models of resistivity: the motion of conduction electrons is hampered by their scattering with impurities and lattice vibrations and it was supposed to decrease monotonically with temperature, reaching a finite value at zero temperature, related to the lattice imperfections. Jun Kondo showed [4] that the spin-scattering originating from an anti-ferromagnetic coupling between a magnetic impurity and the conduction electrons of the metal becomes the dominant scattering channel at low temperatures, resulting in a logarithmic increase of the resistivity as the temperature is lowered. Despite Kondo's perturbative treatment explaining the rise in resistivity, it resulted in a diverging scattering rate below a specific temperature, now referred to as the Kondo temperature T_K, which sets the *crossover* energy scale for which the Kondo effect manifests itself. The logarithmic divergence also appeared in other physical quantities, such as susceptibility or specific heat, and efforts to eliminate it led to many advances in physics, such as the numerical or perturbative renormalisation groups. In the end, the *many-body* system was found to be a *local* Fermi liquid[1] at near-zero temperature, with a scattering rate proportional to the square of the temperature, and the impurity spin being fully screened and forming a spin-singlet with the conduction electrons.

Despite a well-established theoretical understanding of the *single-impurity* Kondo effect, other kindred manifestations, such as when a larger density of magnetic impurities is present, are still a matter of study. In heavy-fermion compounds, neighbouring impurities can interact via the Ruderman–Kittel–Kasuya–Yosida coupling mechanism, favouring a magnetically ordered phase and directly competing with the Kondo screening of the magnetic impurities, responsible for a (lattice-coherent) *heavy* Fermi-liquid phase, with an effective electron mass possibly thousands of times larger than the bare one [6]. Although Doniach's picture [7] offers a good

[1] A Fermi liquid describes an interacting system of electrons as a system of (weakly interacting) fermionic quasiparticles. A fundamental element in Fermi liquid theory is the concept of quasiparticles, long-lived and low-energy excitations of the Fermi liquid that carry the bare electron charge and spin but whose effective mass is renormalised by interactions [5]. These quasiparticles are generated from adiabatically turning on the Coulomb interaction between particles of a charged Fermi gas and are a suitable approximation to describe conduction electrons in ordinary metals.

qualitative explanation of the competition between the two phases, questions such as how the Kondo lattice coherence forms and changes with temperature [8], or the fate of the Kondo cloud [9] or of the heavy quasiparticles [10–12] at the quantum critical point, which separates both quantum phases, are still heavily debated.

Whereas the field of strongly-interacting electrons – encompassing, e.g., Kondo physics, spin liquids, superconductivity – has been at the forefront of modern theoretical and experimental research, the last decade has seen a steady increase in the study of *non-equilibrium* phenomena, namely concerning the dynamics of interacting electrons. Arguably, this shift was made possible theoretically through a renewed interest in – and irreverence towards – problems once deemed too "violent" to be treated with quantum field theory, and experimentally by advances in the techniques and instrumentation of ultrafast measurement. In particular, recent experiments with time-resolved spectroscopy [12–15] have cast new light onto the yet unsettled questions about heavy-fermion compounds. The intricate non-equilibrium dynamics observed, related to the collapse and subsequent *revival* of the Kondo effect, following irradiation by an electromagnetic pulse, warrants a detailed theoretical study. However, due to the difficulty of resolving the low temperatures and long timescales characteristic of Kondo systems, non-equilibrium theoretical studies were mainly confined to quasi-equilibrium or quantum-dot configurations [16–19]. Such difficulties stem from the strongly interacting character of Kondo physics and were addressed by combining and extending varied field-theoretical and numerical[2] methods in order to uncover the physics intrinsic to heavy-fermion systems.

I Quantum Many-Body Systems in Non-Equilibrium

Virtually all systems found in nature are in a state of non-equilibrium – an indispensable prerequisite of life – and will likely remain so until the heat-death of the universe. The distribution of a non-equilibrium state, described by a density matrix $\hat{\rho}$, is best understood by what it is *not*: a Gibbs ensemble

$$\hat{\rho} \neq \frac{e^{-\beta \hat{H}}}{\operatorname{tr} e^{-\beta \hat{H}}} \ ,$$

or associated generalisations [22]. These maximise entropy under dynamical constraints, depending only on the values of a few conserved charges, such as energy [23], with the former arising for a system described by a time-independent Hamiltonian $\hat{H}$ in thermal equilibrium with an infinitely large heat reservoir at inverse temperature β. At the macroscopic scale, however, many systems are *near* thermal equilibrium – keeping no memory about their past and being described by Gibbs ensembles. This is perhaps expected for macroscopic classical systems due to the large phase space available for fast particle collisions that nonlinearly scramble the system's information through its constituents, resulting in a memoryless ensemble. More surprisingly, despite the linearity and reversibility of time evolution in Quantum Mechanics, these also appear to be the dynamical fixed point, or asymptotic state, for most quantum many-body systems. This is behind the success of thermal quantum field theory – paired with statistical physics and a profound knowledge of many-body and physical processes – explaining the physics of emergent phenomena and properties of commonly found states of matter. A non-equilibrium setting brings further challenges, such as incorporating non-trivial initial conditions and time-dependent Hamiltonians, identifying different non-equilibrium regimes and

[2] Despite the solemn words of the "pope" [20] Philip Anderson, reprehending the then – and now – status of the field of condensed-matter, where he remarks [21] a "prejudice in favour of heavy computer use and the existence of the oxymoron 'computational physics'", bridging the world of many-body physics and transient dynamics without recourse to some sort of numerics appears to be a task worthy only of his apostolic successor.

their timescales, or understanding the influence of external, time-dependent fields. Moreover, systems in non-equilibrium lack underlying solid physical principles found in thermal equilibrium, which facilitate the development of theoretical techniques, such as time translational invariance, conservation of energy and/or particle number, or the principle of minimum energy, where the total energy of a system with fixed entropy is minimised.

An attempt to condense all of the relevant works of non-equilibrium quantum field theory appropriately into a handful of pages would be nothing less than a Sisyphean task, and in view of the extensiveness and comprehensiveness of the field, Chapter 1 aims to be a modest, self-contained introduction. Nevertheless, it lays the foundation on which the thesis rests and is driven by one of the foundational questions of the field: how to calculate – from first principles – experimentally-accessible observables of quantum systems in *non-equilibrium*. Non-equilibrium quantum field theory is intimately related with *time evolution*, arguably the most fundamental transformation in quantum physics. Barring grand questions, such as how the irreversibility of time in the macroscopic world arises from a time-reversible microscopic quantum world, its utilitarian goal is to describe the time evolution of a system from some initial, arbitrary state via its transient dynamics to its long-time, asymptotic state.

A path-integral formulation of non-equilibrium quantum field theory is developed for a closed system by specifying a density matrix, encoding its initial condition, and the system's Hamiltonian, which entirely generates its unitary dynamics. Different initial density matrices are encoded by different time contours, namely the Schwinger, Keldysh or Konstantinov-Perel' contour, which arise naturally when calculating observables perturbatively, a necessity since interacting quantum field theories generally do not have closed-form solutions. The n-particle irreducible effective action formalism is introduced to go beyond bare perturbative expansions, which display spurious error growth with time in non-equilibrium regimes [24] and fail in being controllable approximations or ensuring conservation laws. Namely, stationarity conditions of the two-particle irreducible effective action yield self-consistent equations for the one-point (mean-fields) and two-point functions (Green functions), resulting in a conserving theory, valid for all orders of the perturbative expansion and fully general regarding arbitrarily fast or slow modulation of the system parameters or external fields. As such, non-equilibrium dynamics are studied through these two-point functions, which encode spectral and statistical information and can be used to understand coherence and decoherence, and calculate any physical observable related to single-particle excitations, such as densities and currents.

Interacting theories typically do not have closed-form solutions and require perturbative expansions when calculating n-point functions. This thesis focuses on the study of strongly-interacting matter, where it is common to come across conditions where the Coulomb interaction is the largest energy scale in the system, and perturbative expansions fail – whether due to non-convergence of the perturbative series or failure of Wick's theorem due to the Hamiltonian operators not satisfying *canonical* commutation relations. In Chapter 2, the method of auxiliary particles is introduced, which, compared to alternative ways [25] of tackling these issues, directly allows the construction of a path integral and perturbative expansions, and hence access to the whole machinery of quantum field theory. The addition of auxiliary particles and subsequent truncation of the enlarged Hilbert space results in distinctive properties of auxiliary-particle two-point functions. These encompass unusual equations of motion in non-equilibrium regimes and non-trivial two-point function components related to thermal initial conditions.

The equations of motion of two-point functions in non-equilibrium are 2-time integrod-ifferential equations, which are highly nonlinear and typically scale at least cubically with time due to their 2-time and integral nature. Reducing the number of numerical steps – a significant bottleneck for studying long-time dynamics – required for integrating the equations of motion can dramatically increase the accessible integration time. In Chapter 3, the technique

of adaptivity, common in the solution of standard ordinary differential equations, is extended to integrodifferential equations, and some other techniques to reduce computational complexity are presented.

II Optically Driven, Non-Equilibrium Heavy-Fermion Systems

A measurement always requires some sort of interaction with matter, unavoidably driving the system out of equilibrium, however varying exactly *how much*. In weak perturbation regimes, where the system's response is proportional to the perturbation, linear-response theory [26] can successfully describe the underlying physics, as the interactions of excited states with the rest of the system are neglected. However, much deeper insight into the behaviour of matter can be obtained with stronger perturbations, driving the system out of equilibrium and generating nonlinear responses, requiring the more refined quantum field theory. An example is through optical or terahertz (THz) spectroscopy, which, beyond the technological prospects of manipulating conduction and optical properties through the interplay of matter and radiation [27, 28], is playing an ever-increasing role in providing an understanding of the microscopic processes and quasiparticle dynamics that determine the physics of complex materials such as strongly-interacting materials.

The prototypical strongly-interacting materials are heavy-fermion compounds, a class of metals formed between actinide/rare-earth elements and transition/noble metals. The interplay of localisation, due to strong Coulomb interaction within valence electrons of the former and itineracy of the conduction electrons, leads to exotic quantum behaviour, such as Kondo, anti-ferromagnetic and superconductor physics – all characteristic of heavy-fermion compounds. These are also particularly rich in low-energy excitations such as collective lattice (phonon), electronic (plasmon) and many-body (e.g., Kondo) excitations, typically in the THz[3] regime. In the past, experiments probed these compounds with near-infrared or optical light pulses. However, such photons carried too much energy and tended to over-excite the system by either overheating or destroying any low-energy excitation – a problem which has been overcome by THz spectroscopy, which uses photons with up to a hundred times less energy and hence can target only low-energy excitations.

In particular, the heavy-fermion compound $CeCu_6$ responded [12] to an incident ultrafast THz pulse by the emission of a time-delayed reflex pulse. It was understood that such an "echo" response arose from the reconstruction of the Kondo regime following its destruction by the incident pulse. This intriguing observation was the *driving force* behind this thesis, which aims at a complete microscopic description of the transient collapse and subsequent revival of Kondo lattice coherence by a single-pulse of quantum radiation, far away from the quantum critical point and deep in the heavy Fermi liquid phase. At first glance, a heavy-fermion lattice driven by a single pulse of radiation may look like an innocuous theoretical problem. However, it is well-known that heavy-fermion problems are already some of the most demanding in thermal equilibrium. Moreover, in this non-equilibrium setting, several more obstacles are present, namely modelling a travelling pulse of quantum radiation and the predestined necessity of coupling the system to reservoirs. Moreover, there is also the technical problem of resolving previously inaccessible low temperatures and long timescales required for the emergence of Kondo physics. In Chapter 4, this problem is set out in greater detail, with a closer inspection of the time-resolved spectroscopy experiment [12] and the microscopic model and phenomenology

[3] According to Planck's law, every physical body in thermal equilibrium spontaneously emits electromagnetic radiation. Chances are that this thesis's medium mainly radiates THz ($\sim 10^{12}$ Hz) photons, given an ambient temperature of roughly 300 K on the Earth's surface.

that describes the low-energy physics of $CeCu_6$. The difficulty of solving the microscopic models of such systems is rooted in the failure of many-body perturbative expansions due to the Coulomb interaction strength vastly exceeding the other energy scales – an ideal playground for *auxiliary particles*. This system is to be perturbed by a single Gaussian pulse of THz radiation, which arrives, destroys the heavy quasiparticles and then flies away, carrying information about the interaction. Without dissipative dynamics, the interaction of the external pulse of radiation with matter could deposit excess energy into the system, which would heat up due to being closed. Dissipative dynamics also appear to be at odds with the Hamiltonian formulation of quantum mechanics, which is unitary. A naive quantisation of classical dissipative mechanics can even lead to the decay of the fundamental Heisenberg uncertainty relation [29]. However, a "system plus reservoir" approach can describe dissipative dynamics by introducing an environment, a reservoir of infinitely many modes the system can couple with, but cannot renormalise due to its vastness. This introduces quantum scattering channels through which information/energy of the system is irreversibly lost, allowing the excess energy to be dissipated into the environment and bringing the formulation closer to experimental settings.

Due to the THz pulse matching the timescales associated with Kondo physics, no separation of timescales can alleviate the non-equilibrium formulation, which must be kept fully general. Despite the field-theoretical framework introduced being adequate to describe such non-separable regimes, the low-energy auxiliary-particle Hamiltonian that captures a general heavy-fermion system with a *drive by* quantum radiation is still far too complicated to be solved. It is plagued by the same mathematical intractability of interacting quantum systems encountered by Paul Dirac almost a century ago,

> The underlying physical laws necessary for the mathematical theory of a large part of physics and the whole of chemistry are thus completely known, and the difficulty is only that the exact application of these laws leads to equations much too complicated to be soluble. [30]

Theoreticians are thus forced into simplifying approximations that reduce the complexity of the problem, coming to a workable set of equations. A common tactic is first to try to describe the physics in a classical limit, and in Chapter 5, the problem is solved at the saddle point. This approximation shackles quantum fluctuations and dramatically simplifies the problem, at the cost of being only an educated guess of the underlying Kondo physics. Then, as perhaps foreseen, one must go beyond the classical limit, leading to Chapter 6 and a concoction of all the previous chapters. However, the unruliness of quantum fluctuations complicates the theory exponentially, which must yet somehow be tamed: in the complex world of strongly-interacting matter, no model is *correct*, and the art is in constructing a theory that is *not* wrong. An indispensable approximation to lattice systems is provided by dynamical mean-field theory, where the problem is mapped to an effective interacting single-site. However, a solution of strong interactions in a single site also requires some approximation or truncation of its perturbative series, as it does not have a closed form. For that, the non-crossing approximation, known to reproduce Kondo physics qualitatively, is employed. Finally, the dynamics of the driven-dissipative heavy-fermion lattice system can be resolved, and long-time temporal coherence aspects of Kondo physics are investigated.

Summary of manuscripts and publications

The contents of Chapter 2 appear in

> F. Meirinhos, M. Kajan, T. Bode, and J. Kroha, *Auxiliary particles in closed and open systems*, in preparation

The contents of Chapter 3 appear in

> [32] F. Meirinhos, M. Kajan, J. Kroha, and T. Bode, "Adaptive Numerical Solution of Kadanoff-Baym Equations", SciPost Phys. Core **5** (2022) DOI: 10.21468/SciPostPhysCore.5.2.030

Non-thesis research: I have also contributed to the following publications. These are excluded from the remainder of this thesis.

> L. R. Gorjão and F. Meirinhos, "Kramersmoyal: kramers–moyal coefficients for stochastic processes", Journal of Open Source Software **4** (2019) DOI: 10.21105/joss.01693
>
> T. Bode, M. Kajan, F. Meirinhos, and J. Kroha, *Non-markovian dynamics of open photon condensates*, in preparation

Summary of open source contributions

The advice that "software is just another kind of experimental apparatus and should be built, checked, and used as carefully as any physical apparatus" [33] was regarded throughout the code development, and as much intensity and *commit*ment were invested in these implementations as in the theory presented in this thesis. Only then would it be possible to ascertain that the obtained results are *true* and not artefacts of either bugs or unidentified numerical limitations. As such, the entirety of the code and experiments used to generate the results presented is open-source and adequately tagged for full reproducibility:

- https://doi.org/10.60507/FK2/Q2VE6X
  A Julia implementation of an adaptive two-time Volterra integrodifferential equation solver presented in Chapter 3, as well as the Wigner-Ville transform presented in Chapter 1.
- https://doi.org/10.60507/FK2/C0YZ1B
  A Julia implementation of the Kondo problems presented in Chapter 5 and Chapter 6.

The source code for this thesis document is available at:
https://doi.org/10.60507/FK2/S27IOB

Part I

Quantum Many-Body Systems in Non-Equilibrium

Chapter 1

Non-equilibrium quantum field theory

The time-evolution operator $\hat{U}$

$$\hat{U}(t,t') = \mathbb{T}\left[e^{-i\int_{t'}^{t} \mathrm{d}\bar{t}\,\hat{H}(\bar{t})}\right] \qquad \text{for } t > t' \ , \tag{1.1}$$

where $\hat{H}(t)$ is a (time-dependent) Hamiltonian and $\mathbb{T}$ the time-ordering operator, generates the time evolution of wavefunctions $|\Psi(t)\rangle = \hat{U}(t,t')\,|\Psi(t')\rangle$ or density matrices $\hat{\rho}(t) = \hat{U}(t,t')\hat{\rho}(t')\hat{U}(t',t)$, for all times t. Similarly to the wave function of a quantum system, a density matrix scales, at worst, exponentially with system size and, despite describing a quantum ensemble of particles exactly, can be impractical for the calculation of observables. This difficulty is addressed by non-equilibrium quantum field theory, which can directly reformulate the quantum problem and its time evolution in terms of the observables of interest, typically objects of much lower dimensionality.

1.1 The Schwinger contour

The time-ordering operator $\mathbb{T}$ is not an operator in the quantum-mechanical, conventional sense – associated with an observable – but rather establishes a rule on how to arrange products of operators which depend on time: given a time-grid $t_1 < t_2 < \ldots < t_n$

$$\mathbb{T}\left[\hat{H}(t_{P(\ell)})\ldots\hat{H}(t_{P(2)})\hat{H}(t_{P(1)})\right] = \hat{H}(t_\ell)\ldots\hat{H}(t_2)\hat{H}(t_1) \ , \tag{1.2}$$

for all permutations P of $\{1,2,\ldots,\ell\}$. For commuting Hamiltonian operators $\left[\hat{H}(t_i),\hat{H}(t_j)\right] = 0$, $\mathbb{T}$ has no influence on (1.1) and the integral can be evaluated directly. However, in general, Hamiltonian operators at different times do not commute, and $\hat{U}(t,t')$ is the continuous limit of an infinite product of locally constant Hamiltonian operators

$$\hat{U}(t,t') \equiv \lim_{N\to\infty} e^{-i\hat{H}(t)\delta t}e^{-i\hat{H}(t-\delta t)\delta t}\ldots e^{-i\hat{H}\left(t-(N-1)\delta t\right)\delta t} \ , \tag{1.3}$$

where $\delta t = (t-t')/(N-1)$ is some infinitesimal time-step. From the group property that

$$\hat{U}(t,t')\hat{U}(t',t) = \hat{\mathbb{1}} \ , \tag{1.4}$$

it can be inferred through a decomposition akin to (1.3) that

$$\hat{U}(t,t') = \bar{\mathbb{T}}\left[e^{+i\int_{t}^{t'} \mathrm{d}\bar{t}\,\hat{H}(\bar{t})}\right] \qquad \text{for } t < t' \ , \tag{1.5}$$

where $\bar{\mathbb{T}}$ is the anti-time-ordering operator, ordering the operators in the reverse order of (1.2).

A time-dependent observable $O(t)$ is obtained by calculating the ensemble average of its associated operator $\hat{O}(t)$ in the Heisenberg picture,

$$O(t) = \left\langle \hat{O}(t) \right\rangle \coloneqq \frac{\mathrm{tr}\left\{\hat{\rho}(t_0)\hat{O}(t)\right\}}{\mathrm{tr}\left\{\hat{\rho}(t_0)\right\}} = \frac{\mathrm{tr}\left\{\hat{\rho}(t_0)\hat{U}(t_0,t)\hat{O}(t)\hat{U}(t,t_0)\right\}}{\mathrm{tr}\left\{\hat{\rho}(t_0)\right\}} , \tag{1.6}$$

where $\hat{\rho}(t_0)$ is the initial density matrix – describing an arbitrary interacting or non-interacting state at $t = t_0$, with the trace taken over the Hilbert space on which the Hamiltonian acts. Note that – despite the abuse of notation – the operator $\hat{O}$ retains a time argument, which solely records the instance of time that the (constant-in-time) Schrödinger operator should act on. By defining an oriented time path $\gamma = (t_0, t) \oplus (t, t_0)$, the ensemble average can directly be written as a path-ordered product of operators on γ,

$$\left\langle \hat{O}(t) \right\rangle = \frac{\mathrm{tr}\left\{\hat{\rho}(t_0)\mathbb{T}_\gamma\left[e^{-i\int_\gamma \mathrm{d}\bar{t}\,\hat{H}(\bar{t})}\hat{O}(t)\right]\right\}}{\mathrm{tr}\left\{\hat{\rho}(t_0)\right\}} , \tag{1.7}$$

where $\mathbb{T}_\gamma$ is a time-ordering operator, rearranging the operators by their *chronological* order on γ, i.e., preceding operators on the contour on the right. Finally, due to (1.4), the path in the denominator can be extended to γ yielding

$$\left\langle \hat{O}(t) \right\rangle = \frac{\mathrm{tr}\left\{\hat{\rho}(t_0)\mathbb{T}_\gamma\left[e^{-i\int_\gamma \mathrm{d}\bar{t}\,\hat{H}(\bar{t})}\hat{O}(t)\right]\right\}}{\mathrm{tr}\left\{\hat{\rho}(t_0)\mathbb{T}_\gamma\left[e^{-i\int_\gamma \mathrm{d}\bar{t}\,\hat{H}(\bar{t})}\right]\right\}} . \tag{1.8}$$

The dynamics of the system are then entirely determined by its initial state together with the Hamiltonian, and the calculation of an observable is realised by evolving the initial state forward and then backwards in time, resulting in the ubiquitous closed-time Schwinger [34] contour. It is possible to eliminate the backward branch of the contour [35] in a system in equilibrium, as the ground state in the distant future is known. However, this does not hold in non-equilibrium systems since there is no guarantee that the system can return to its ground state.

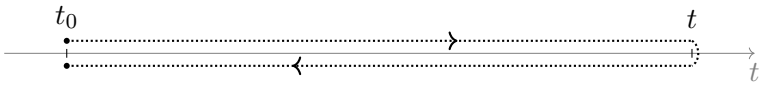

Figure 1.1: The Schwinger contour. Note that the forward (denoted by subscript $(-)$) and backward (denoted by a subscript $(+)$) branches are only displaced for graphical purposes. In addition, generally $\hat{O}(t_+)$ can be different from $\hat{O}(t_-)$ for any $t \in \gamma$.

1.2 Interacting initial conditions

Unlike in a many-body interacting system at large times $t \gg t_0$, where it generally holds that it no longer contains information related to its initial state, i.e., the initial *correlations* of the system have decayed with time, the transient dynamics during early times $t \gtrsim t_0$ are primarily

dominated by the system's initial state at time t_0, encoded by the initial density matrix $\hat{\rho}(t_0)$. This time t_0 typically serves as an actual boundary between the past – formally a preparatory stage for an interacting state – and the onset of a qualitatively different process – for example, a sudden change in the environment or coupling to an external field. A fundamental problem of starting from an interacting state – containing non-Gaussian correlations – is that it is incompatible with the Wick decomposition [36]: if the density matrix is not separable into a product of Gaussian operators, the expectation value of a product of operators does not factorise into a product of expectation values of pairs of operators.

1.2.1 The Keldysh contour

This problem was at first[1] resolved by adiabatically switching on the interactions from a non-interacting state at a very distant past [38]. The interacting density matrix $\hat{\rho}(t_0)$ is generated through the adiabatic switch

$$\hat{\rho}(t_0) = \hat{U}(t_0, -\infty)\hat{\rho}(t_{-\infty})\hat{U}(-\infty, t_0) \ , \tag{1.9}$$

where $\hat{\rho}(t_{-\infty})$ is a non-interacting density matrix, and $\hat{U}$ evolves with the Hamiltonian

$$\hat{H}(t) = \begin{cases} \hat{h}_0 + e^{-\eta|t-t_0|}\hat{h}_{\text{int}} \ , & t < t_0 \\ \hat{h}_0 + \hat{h}_{\text{int}} \ , & \text{otherwise} \ , \end{cases} \tag{1.10}$$

where $\hat{h}_0$ and $\hat{h}_{\text{int}}$ are the non-interacting and interacting parts of the Hamiltonian, and η is an infinitesimal positive number. Substituting this definition of $\hat{\rho}(t_0)$ in (1.6) will result in an extension of the contour γ. Furthermore, γ can be made independent of t, owing to (1.4), by inserting $\hat{\mathbb{1}} \equiv \hat{U}(t, +\infty)\hat{U}(+\infty, t)$ after $\hat{O}(t)$ in the same equation. These operations extend the path beyond t, to infinity and back, transforming the original Schwinger contour into the Keldysh contour.

A tangential concept [39] to the adiabatic switch is the idea that any admissible *initial* state of the system, at $t = t_0$, is the outcome of some preparatory stage. Specifically, this initial state is but an *intermediate* state, which some antecedent state arrived at, with the observatory stage of the system, at $t > t_0$, following coherently after the (historical) state preparation.

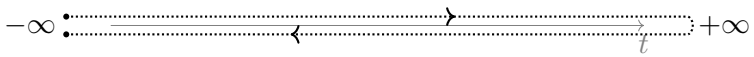

(a) Original contour [38]

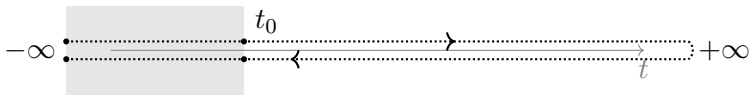

(b) Time-partitioned contour [39]

Figure 1.2: The Keldysh contour is also often called the Schwinger-Keldysh contour. The shaded region denotes the preparatory stage, starting in some distant past.

1.2.2 The Konstantinov-Perel' contour

For an interacting thermal initial state, a far more practical – and arguably less artificial – approach is preparing the initial state through time evolution in the complex-time plane [36, 40].

[1] Refer to [37] and references therein for a historical overview of the theoretical development concerning the inclusion of interacting initial conditions.

For an interacting system in thermodynamic equilibrium with a reservoir at inverse temperature β and chemical potential μ, the density matrix is given by [41]

$$\hat{\rho}(t_0) = \frac{e^{-\beta(\hat{\mathcal{H}}-\mu\hat{N})}}{\operatorname{tr} e^{-\beta(\hat{\mathcal{H}}-\mu\hat{N})}} = \frac{e^{-i\int_{t_0}^{t_0-i\beta}\mathrm{d}\bar{z}\,(\hat{\mathcal{H}}-\mu\hat{N})}}{\operatorname{tr} e^{-i\int_{t_0}^{t_0-i\beta}\mathrm{d}\bar{z}\,(\hat{\mathcal{H}}-\mu\hat{N})}}\ , \tag{1.11}$$

where $\hat{\mathcal{H}}$ is the Hamiltonian for the system in equilibrium and $\hat{N}$ is the particle-number operator. Denoting the path $(t_0, t_0 - i\beta) \coloneqq \gamma^M$, the ensemble average (1.8) can be written as

$$\left\langle \hat{O}(z) \right\rangle = \frac{\operatorname{tr}\left\{ e^{-i\int_{\gamma^M}\mathrm{d}\bar{z}\,(\hat{\mathcal{H}}-\mu\hat{N})}\mathbb{T}_\gamma\left[e^{-i\int_\gamma \mathrm{d}\bar{z}\,\hat{H}(\bar{z})}\hat{O}(z)\right]\right\}}{\operatorname{tr}\left\{ e^{-i\int_{\gamma^M}\mathrm{d}\bar{z}\,(\hat{\mathcal{H}}-\mu\hat{N})}\mathbb{T}_\gamma\left[e^{-i\int_\gamma \mathrm{d}\bar{t}\,\hat{H}(\bar{t})}\right]\right\}}\ . \tag{1.12}$$

The superscript M stands for Matsubara, a formalism [42] for systems in thermal equilibrium where the density matrix is treated as the (imaginary-)time-evolution operator. Defining a new oriented time path $\gamma = \gamma \oplus \gamma^M$, the cyclic property of the trace allows the integral over γ^M to be brought inside $\mathbb{T}_\gamma$,

$$\left\langle \hat{O}(z) \right\rangle = \frac{\operatorname{tr}\left\{ \mathbb{T}_\gamma\left[e^{-i\int_\gamma \mathrm{d}\bar{z}\,\hat{H}(\bar{z})}\hat{O}(z)\right]\right\}}{\operatorname{tr}\left\{ \mathbb{T}_\gamma\left[e^{-i\int_\gamma \mathrm{d}\bar{z}\,\hat{H}(\bar{z})}\right]\right\}}, \tag{1.13}$$

where

$$\hat{H}(z) = \begin{cases} \hat{\mathcal{H}} - \mu\hat{N}\ , & z \in \gamma^M \\ \hat{H}(z)\ , & \text{otherwise}\ . \end{cases} \tag{1.14}$$

Note that despite the ensemble average (1.8) having been originally formulated for an operator with time arguments on the real-time contour, the real-time t is promoted to a complex time z and (1.13) is fully general for any $z \in \gamma$. While technically not required, the path γ can also be made independent of z by inserting $\hat{\mathbb{1}} \equiv \hat{U}(z, +\infty)\hat{U}(+\infty, z)$ after $\hat{O}(z)$ on the right-hand-side of (1.6), resulting in the Konstantinov-Perel' contour, shown in Figure 1.3.

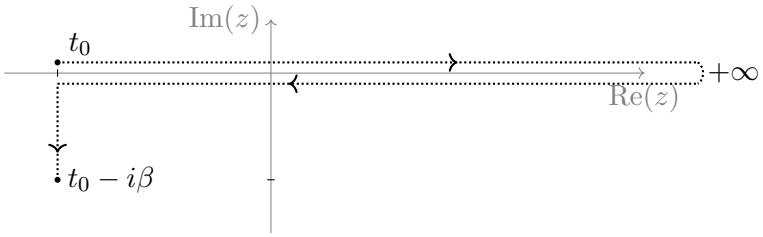

Figure 1.3: The Konstantinov-Perel' contour. There is no agreed terminology for the name of this contour, also often called the Kadanoff-Baym contour. Note that the forward (+) and backwards (−) branches are defined at $\operatorname{Im} z = 0$ and only displaced for graphical purposes.

Even though appearing trivial in its form, transforming the thermal density matrix into a part of the contour has a critical technical outcome. By incorporating the thermal averaging into the contour, perturbative expansions (via Wick's decomposition) within a thermal theory are

well defined. Moreover, this general formulation embodies the Keldysh [38] and Matsubara [42] formalism. Due to being a positive semi-definite operator, the density matrix has a form [43]

$$\hat{\rho} = \frac{e^{-\hat{S}}}{\operatorname{tr} e^{-\hat{S}}} \ , \tag{1.15}$$

which suggests that further manipulation of the time contour inside the ensemble average could appropriately account for initial non-thermal interacting states. However, the treatment of such arbitrary initial conditions [24, 40, 44, 45] is beyond the scope of this text.

1.3 Contour-ordered Green functions

One of the central motivations behind the development of non-equilibrium quantum field theory is the calculation of n-point functions, also known as Green functions – terms which will be used interchangeably. 2-point functions are fundamental objects of many-body theories, describing *single-particle* excitations or statistical distributions of particles, and encode the greater part of the experimentally-accessible observables. The prototypical non-equilibrium Green function is the (2-point) contour-ordered ensemble average

$$G_{ji}(z, z') = -i\left\langle \mathbb{T}_\gamma \left[\hat{c}_j(z)\hat{c}_i^\dagger(z')\right]\right\rangle \ , \tag{1.16}$$

for $(z, z') \in \gamma$, where $\hat{c}^\dagger$ and $\hat{c}$ are creation and annihilation operators, respectively, and the indices of the operators describe some quantum number, depending on the system under consideration. Due to the algebra of the operators,

$$\mathbb{T}_\gamma \left[\hat{c}_j(z)\hat{c}_i^\dagger(z')\right] = \begin{cases} \hat{c}_j(z)\hat{c}_i^\dagger(z') & \text{if } z \succ z' \ , \\ \xi\hat{c}_i^\dagger(z')\hat{c}_j(z) & \text{if } z \prec z' \ , \end{cases} \tag{1.17}$$

where $\xi = 1$ for bosonic ($\mathbb{C}$-number algebra) and $\xi = -1$ for fermionic (Grassmann-number algebra) operators. The contour-ordered Green function can then be decomposed as

$$\begin{aligned} G_{ji}(z, z') &= \Theta_\gamma(z, z')\left[-i\left\langle \hat{c}_j(z)\hat{c}_i^\dagger(z')\right\rangle\right] + \Theta_\gamma(z', z)\left[-i\xi\left\langle \hat{c}_i^\dagger(z')\hat{c}_j(z)\right\rangle\right] \\ &= \Theta_\gamma(z, z')G_{ji}^{>}(z, z') + \Theta_\gamma(z', z)G_{ji}^{<}(z, z') \ , \end{aligned} \tag{1.18}$$

where $\Theta_\gamma(z, z')$ is a generalised Heaviside step function[2] on the γ contour,

$$\Theta_\gamma(z, z') = \begin{cases} 1 \ , & z \succ z' \\ 0 \ , & \text{otherwise} \ . \end{cases} \tag{1.20}$$

The so-called *greater* ($G^>$) and *lesser* ($G^<$) components owe their names to the decomposition of the contour-ordered Green function – which equals $G^>$ when $z \succ z'$ or $G^<$ when $z \prec z'$ on

[2] The generalised Dirac delta function $\delta_\gamma(z, z') \coloneqq \frac{\mathrm{d}}{\mathrm{d}z}\Theta_\gamma(z, z')$ on the contour is given by

$$\delta_\gamma(z, z') = \begin{cases} +\delta(t - t') & \text{if } (z \to t, z' \to t') \text{ are in the forward Keldysh branch,} \\ -\delta(t - t') & \text{if } (z \to t, z' \to t') \text{ are in the backward Keldysh branch,} \\ +i\delta(\tau - \tau') & \text{if } (z \to -i\tau, z' \to -i\tau') \text{ are in the Matsubara branch,} \\ 0 & \text{otherwise} \ . \end{cases} \tag{1.19}$$

the contour γ. Note, however, that the time arguments of $G^{\gtrless}$ do not have to fulfil such time constraints: $G^{\gtrless}$ are defined for *all* values $(z, z') \in \gamma$. In physical terms, the characterisation of single-particle dynamics is fully encoded in $G^{<}$ and $G^{>}$, which describe amplitudes related to the propagation of a hole or particle in a fermionic many-body system, respectively. Note that the (anti-)commutation of particles holds for all times $G^{>}(z, z) - G^{<}(z, z) = -i$.

1.3.1 Components of contour-ordered Green functions

Depending on the contour branches the operators act on, the contour-ordered Green function can be decomposed into different *components*. For (z, z') lying on the Konstantinov-Perel' contour (Figure 1.3), the components of $G(z, z')$ read

$$\begin{aligned} G(z, z') &= \begin{pmatrix} G(t_-, t'_-) & G(t_-, t'_+) & G(t_-, t_0 - i\tau') \\ G(t_+, t'_-) & G(t_+, t'_+) & G(t_+, t_0 - i\tau') \\ G(t_0 - i\tau, t'_-) & G(t_0 - i\tau, t'_+) & G(t_0 - i\tau, t_0 - i\tau') \end{pmatrix} \\ &= \begin{pmatrix} \Theta(t - t')G^{>}(t, t') + \Theta(t' - t)G^{<}(t, t') & G^{>}(t, t') & G^{\rceil}(t, \tau') \\ G^{<}(t, t') & \Theta(t - t')G^{<}(t, t') + \Theta(t' - t)G^{>}(t, t') & G^{\rceil}(t, \tau') \\ G^{\lceil}(\tau, t) & G^{\lceil}(\tau, t) & \mathcal{G}(\tau, \tau') \end{pmatrix}, \end{aligned} \tag{1.21}$$

with $(t_0 - i\tau, t_0 - i\tau')$ lying on the imaginary time branch and (t_-, t'_-) and (t_+, t'_+) on horizontal time forward and backwards branches, respectively, and the relation[3] $\hat{O}(t_-) = \hat{O}(t_+)$ being employed in the last equality. As a result, the distinction between horizontal branches in the time arguments of the Green functions is dropped since $G^{\gtrless}(t_-, z') = G^{\gtrless}(t_+, z')$ and $G^{\gtrless}(z, t'_-) = G^{\gtrless}(z, t'_+)$. The two time branches are simply a formal outcome of unitary time evolution – forward and backward evolution brings the state back to its original state – and can be dropped once operator precedence (1.16) is considered. This is also expected physically since there is just a single time branch in the description of reality, as can be observed in the definition of the time-evolution operator (1.1).

The contour-ordered Green function on the Konstantiv-Perel' contour then contains 5 independent components, which can be divided into three groups: $\mathcal{G}(\tau, \tau')$, $\left\{G^{<}(t, t'), G^{>}(t, t')\right\}$ and $\left\{G^{\rceil}(t, \tau'), G^{\lceil}(\tau, t')\right\}$. First is the *Matsubara* Green function, which contains information about the system in its initial thermal equilibrium stage. It is hence decoupled from the other four components, which describe dynamics in real-time, and determines their initial conditions. The second group is the Keldysh Green functions, which carry information about single-particle correlations in real-time. The third group are the mixed Green functions, which carry information about vestigial single-particle thermal correlations in the system. These usually decay with time, except in specific integrable systems or meta-stable states [40]. Note that the components of $G(z, z')$ for (z, z') on the Keldysh contour (Figure 1.2) are the same as the Keldysh components of $G(z, z')$ on the Konstantinov-Perel' contour (Figure 1.3).

1.3.2 Interpretability of Keldysh Green functions

The Wigner basis

There is a lack of interpretability of 2-point functions in real time. Whereas in equilibrium, by definition, they display time-translation symmetry and can be described in a frequency basis

[3] For most systems of interest, the Hamiltonian is the same whether the time argument is the upper or lower branch, $\hat{U}(t_-, t'_-) = \hat{U}(t_+, t'_+)$, and the relation $\hat{O}(t_-) = \hat{O}(t_+)$ similarly holds for operators in the Heisenberg picture.

that directly relates to the system's energy spectrum, it is not immediately intuitive how to interpret a non-equilibrium Keldysh Green function. The Wigner basis

$$G(T,\tau)_{\mathrm{W}} = G(T+\tau/2, T-\tau/2) \ , \tag{1.22}$$

is obtained by rotating and squeezing the real-time coordinates (t,t')

$$\begin{pmatrix} \sqrt{2} & 0 \\ 0 & \frac{1}{\sqrt{2}} \end{pmatrix} \cdot \begin{pmatrix} \cos\frac{\pi}{4} & -\sin\frac{\pi}{4} \\ \sin\frac{\pi}{4} & \cos\frac{\pi}{4} \end{pmatrix} \cdot \begin{pmatrix} t \\ t' \end{pmatrix} = \begin{pmatrix} 1 & -1 \\ \frac{1}{2} & \frac{1}{2} \end{pmatrix} \cdot \begin{pmatrix} t \\ t' \end{pmatrix} =: \begin{pmatrix} \tau \\ T \end{pmatrix} \ , \tag{1.23}$$

for which T is called the *centre-of-mass* time and τ the *relative* time, and their derivatives are given by

$$\partial_T = \partial_t + \partial_{t'}, \quad \partial_\tau = \frac{\partial_t - \partial_{t'}}{2} \ . \tag{1.24}$$

Since equilibrium physics is characterised by time-translation invariance – i.e., independence in T – equilibrium 2-point functions are just dependant on τ, and are commonly expressed in the dual Fourier basis ω. The Wigner-Ville transform

$$G(T,\omega)_{\tilde{\mathrm{W}}} = \int_{-\infty}^{+\infty} \mathrm{d}\tau \, e^{i\omega\tau} G(T,\tau)_{\mathrm{W}} = \int_{-\infty}^{+\infty} \mathrm{d}\tau \, e^{i\omega\tau} \left[\int_{-\infty}^{+\infty} \frac{\mathrm{d}\omega'}{2\pi} e^{-i\omega'\tau} G(T,\omega')_{\tilde{\mathrm{W}}} \right] \ , \tag{1.25}$$

provides a convenient linear transformation, where it is possible to establish generalisations of equilibrium properties or interpret non-equilibrium 2-point functions from the viewpoint of equilibrium 2-point functions. Note, however, that Wigner-Ville-transformed functions are *non-causal* since at each time-slice T the frequencies ω contain information from times *before* and *after* T. As such, when far from stationarity, interpretation of Wigner-Ville-transformed 2-point functions must be taken with a grain, or rock, of salt.

Other contour representations

Even though the greater/lesser components are the natural decompositions of the contour-ordered Green function (1.18), other representations of non-equilibrium Green functions exist. A possible representation is given by

$$\rho_{ji}(z,z') = -i \left\langle \left[c_j(z), c_i^\dagger(z') \right]_{-\xi} \right\rangle \equiv G^{>}_{ji}(z,z') - G^{<}_{ji}(z,z') \tag{1.26a}$$

$$F_{ji}(z,z') = \frac{1}{2} \left\langle \left[c_j(z), c_i^\dagger(z') \right]_{\xi} \right\rangle \equiv \frac{i}{2} \left(G^{>}_{ji}(z,z') + G^{<}_{ji}(z,z') \right) \ , \tag{1.26b}$$

where ρ and F are coined as the *spectral* and *statistical* functions, respectively. Unlike $G^{\gtrless}$, which describe the propagation of a hole/particle excitation, the spectral function roughly encodes the probability density of the available physical states (excitations), and the statistical function encodes the occupation of these states. This interpretation is particularly appropriate for fermionic particles in equilibrium, where Wigner-Ville-transformed $\rho(\cdot,\omega)_{\tilde{\mathrm{W}}}$ is positive definite everywhere with its integral over all ω equalling 1, and can be thought of as the probability density of an excitation having some energy ω. Note the alternative definition of the contour-ordered Green function

$$G(z,z') \equiv \frac{1}{2} \operatorname{sgn}_\gamma(z-z') \rho(z,z') - iF(z,z') \ . \tag{1.27}$$

Another standard representation, however conceptually very similar, for non-equilibrium Green functions in the real-time coordinates (t, t') can be obtained via the Keldysh rotation [46, 47]

$$G^{\mathrm{R}}(t,t') = \Theta(t-t')\left[G^{>}(t,t') - G^{<}(t,t')\right] \tag{1.28a}$$
$$G^{\mathrm{A}}(t,t') = \Theta(t'-t)\left[G^{<}(t,t') - G^{>}(t,t')\right] \tag{1.28b}$$
$$G^{\mathrm{K}}(t,t') = G^{>}(t,t') + G^{<}(t,t') \ , \tag{1.28c}$$

where the superscripts R, A and K stand for *retarded*, *advanced* and *Keldysh*, respectively. The retarded and advanced functions carry spectral information, and the Keldysh function statistical information about the system's single-particle excitations. There is also some historical importance due to the strong connection of the retarded and advanced with the Matsubara Green function in equilibrium (Section 2.3.1).

The fluctuation-dissipation relation

After its excitation and subsequent relaxation stage[4], a non-equilibrium system will evolve towards a stationary state – which is understood as displaying some time-translational invariance. However, this does not necessarily imply that the system has *thermalised* and can be described by a Gibbs distribution (1.11), with counterexamples found in, e.g., non-equilibrium steady-states, metastable or Floquet states. Notably, by construction (1.1), non-equilibrium time evolution is unitary and cannot lose information about its initial state, which is at odds with the fundamental property of thermal systems being memoryless. Furthermore, the concept of temperature (and associated statistical distributions) is also completely absent from the formalism – despite temperature possibly being encoded in the initial density matrix, it is no longer a well-defined property of the system for $t > t_0$. Nonetheless, it has often been observed that a system *can* reach a state displaying identical features to thermal systems, for which an estimate of the effective temperature of the system – or generalised statistical distribution can be determined, assuming that a fluctuation-dissipation relation holds.

The fluctuation-dissipation relation establishes a deep relation between a system's statistical (fluctuation) and spectral (dissipation) information in thermal equilibrium. This is encoded in the Kubo-Martin-Schwinger (KMS) relations, for which the (anti-)periodicity $\mathcal{G}(\tau,\tau) = \xi\mathcal{G}(\tau+\beta,\tau')$ of Matsubara Green functions holds[5]. Satisfying the KMS conditions for (1.27) in a Wigner-Ville-transformed (1.25) basis yields

$$-\frac{1}{2}\rho(\cdot,\omega)_{\tilde{\mathrm{W}}} - iF(\cdot,\omega)_{\tilde{\mathrm{W}}} = \xi e^{-\beta\omega}\left[\frac{1}{2}\rho(\cdot,\omega)_{\tilde{\mathrm{W}}} - iF(\cdot,\omega)_{\tilde{\mathrm{W}}}\right] \ , \tag{1.29}$$

for which the *fluctuation-dissipation relation* reads

$$F(\cdot,\omega)_{\tilde{\mathrm{W}}} = i\left[\frac{1}{2} + \xi n(\omega)\right]\rho(\cdot,\omega)_{\tilde{\mathrm{W}}} \ , \tag{1.30}$$

where $n(\omega)$ is the Bose-Einstein distribution for bosonic or Fermi-Dirac for fermionic 2-point functions. Note that this delicate balance – or interdependence – between occupations and spectra results from the KMS boundary conditions, which holds only for systems in thermal equilibrium. Despite generally the absence of analogous boundary conditions in non-equilibrium,

[4] Refer to [24, 48, 49] for discussions on the characteristic timescales of non-equilibrium dynamics.

[5] Note that the argument τ in Matsubara Green functions denotes the imaginary time $i\tau$ in the Konstantinov-Perel' contour (Figure 1.3) and not the relative time τ of the Wigner basis.

the relation can be observed for systems that have thermalised, motivating a generalisation of the fluctuation-dissipation relation

$$F(T,\omega)_{\tilde{\mathrm{W}}} = i\left[\frac{1}{2} + \xi n(T,\omega)_{\tilde{\mathrm{W}}}\right]\rho(T,\omega)_{\tilde{\mathrm{W}}} \ , \tag{1.31}$$

where $n(T,\omega)_{\tilde{\mathrm{W}}}$ describes a time-dependant distribution function and $\rho(T,\omega)_{\tilde{\mathrm{W}}}$ is a generalisation of the equilibrium spectral function that can roughly describe how the spectral density changes with the centre-of-mass time T.

Separation of timescales

A common, albeit non-general, feature in non-equilibrium 2-point functions is the notion of *fast* and *slow* variables[6]. A separation of timescales [51] is found when the scale Λ of the of time-evolution – with $\Lambda \to \infty$ for a system in a stationary state – is much larger than the inverse of the width of the spectral features Ω

$$\left|\frac{\partial_T G(T,\omega)_{\tilde{\mathrm{W}}}}{G(T,\omega)_{\tilde{\mathrm{W}}}}\right| < \Lambda^{-1} \ , \qquad \left|\frac{\partial_\omega G(T,\omega)_{\tilde{\mathrm{W}}}}{G(T,\omega)_{\tilde{\mathrm{W}}}}\right| < \Omega^{-1} \ . \tag{1.33}$$

For example, by expressing time-integrals as a Moyal product (with the exponentials emerging from the Wigner rotation followed by expressing the translations via their generator, i.e., $f(T+s) = e^{s\,\partial_T} f(T)$)

$$\int \mathrm{d}\bar{t}\, A(t,\bar{t})B(\bar{t},t') = e^{\frac{i}{2}\left[\partial_T^A\partial_\omega^B - \partial_T^B\partial_\omega^A\right]} A(T,\omega)_{\tilde{\mathrm{W}}} B(T,\omega)_{\tilde{\mathrm{W}}} \overset{\Lambda\gg\Omega^{-1}}{\approx} A(T,\omega)_{\tilde{\mathrm{W}}} B(T,\omega)_{\tilde{\mathrm{W}}} \ , \tag{1.34}$$

convolutions between 2-point functions are reduced to local frequency products in centre-of-mass time. Despite breaking causality (similarly to (1.31)), for very slow transients, the non-equilibrium problem is reduced to a quasi-equilibrium problem, which can greatly reduce the complexity of resolving non-equilibrium dynamics.

1.3.3 The Langreth rules

The prescriptions for decoding simple convolutions or products of contour-ordered Green functions into their constituting components are known as the Langreth rules. The principal ingredient for their derivation is the decomposition (1.18), with generalisations of these "contour calculus" rules presented in [52].

For a simple contour-ordered product

$$C(z,z') = A(z,z')B(z',z) = \Theta_\gamma(z,z')A^>(z,z')B^<(z',z) + \Theta_\gamma(z',z)A^<(z,z')B^>(z',z) \ , \tag{1.35}$$

the components' products read

$$C^{\gtrless}(z,z') = A^{\gtrless}(z,z')B^{\lessgtr}(z',z) \ . \tag{1.36}$$

However, the resulting $C^{\gtrless}$ is not a proper greater/lesser Green function as it does not fulfil the symmetry relation (Section 3.5.1) associated with these functions.

[6] Consider a non-interacting 2-point function of a particle with energy ω_0 and average particle number $\bar{n}$

$$G(T,\tau)_{\mathrm{W}} = -i\left[\Theta_\gamma(\tau) + \xi\bar{n}\right] e^{i\omega_0\tau} \ . \tag{1.32}$$

This function has a fast dependence in τ and (infinitely) slow dependence in T. Adding a small disturbance $\omega_0 \to \omega_0 + \Delta\omega(T)$ will result in some dependence in T, however *slower* than in τ [50].

The components of the simplest contour-ordered convolution

$$\begin{aligned} C(z,z') &= \int_\gamma \mathrm{d}\bar{z}\, A(z,\bar{z})B(\bar{z},z') \\ &= \Theta_\gamma(z,z')\int_{z'}^{z} \mathrm{d}\bar{z}\, A^{>}(z,\bar{z})B^{>}(\bar{z},z') + \Theta_\gamma(z',z)\int_{z}^{z'} \mathrm{d}\bar{z}\, A^{<}(z,\bar{z})B^{<}(\bar{z},z') \\ &\quad + \int_{t_0}^{\min_\gamma(z,z')} \mathrm{d}\bar{z}\, A^{>}(z,\bar{z})B^{<}(\bar{z},z') + \int_{\max_\gamma(z,z')}^{t_0-i\beta} \mathrm{d}\bar{z}\, A^{<}(z,\bar{z})B^{>}(\bar{z},z') \ , \end{aligned} \tag{1.37}$$

with $\min_\gamma(z,z')$ and $\max_\gamma(z,z')$ are min and max functions generalised to the contour, with the arguments being compared by their *precedence* in the contour, read

$$C^{\rceil}(t,\tau') = \int_{t_0}^{t} \mathrm{d}\bar{t}\, \left[A^{>}(t,\bar{t}) - A^{<}(t,\bar{t})\right] B^{\rceil}(\bar{t},\tau') - i\int_0^\beta \mathrm{d}\bar{\tau}\, A^{\rceil}(t,\bar{\tau})B(\bar{\tau},\tau') \ , \tag{1.38a}$$

$$C^{\lceil}(\tau,t') = -\int_{t_0}^{t'} \mathrm{d}\bar{t}\, A^{\lceil}(\tau,\bar{t})\left[B^{>}(\bar{t},t') - B^{<}(\bar{t},t')\right] - i\int_0^\beta \mathrm{d}\bar{\tau}\, A(\tau,\bar{\tau})B^{\lceil}(\bar{\tau},t') \ , \tag{1.38b}$$

$$\begin{aligned} C^{\gtrless}(t,t') &= \int_{t_0}^{t} \mathrm{d}\bar{t}\, \left[A^{>}(t,\bar{t}) - A^{<}(t,\bar{t})\right] B^{\gtrless}(\bar{t},t') - \int_{t_0}^{t'} \mathrm{d}\bar{t}\, A^{\gtrless}(t,\bar{t})\left[B^{>}(\bar{t},t') - B^{<}(\bar{t},t')\right] \\ &\quad - i\int_0^\beta \mathrm{d}\tau A^{\rceil}(t,\tau)B^{\lceil}(\tau,t') \ . \end{aligned} \tag{1.38c}$$

1.3.4 Calculation of contour-ordered Green-functions

Initial conditions

For problems on the Konstantinov-Perel' contour, the initial conditions of the Keldysh and mixed Green functions are implicitly determined by the Matsubara Green function $\mathcal{G}(\tau,\tau')$

$$\begin{aligned} G^{<}(t_0,t_0) &= \mathcal{G}(0,0^+) \ , & G^{>}(t_0,t_0) &= \mathcal{G}(0^+,0) \ , \\ G^{\rceil}(t_0,\tau') &= \mathcal{G}(0,\tau') \ , & G^{\lceil}(\tau,t_0) &= \mathcal{G}(\tau,0) \ . \end{aligned} \tag{1.39}$$

Problems with contours such as Figure 1.2a have their initial conditions explicitly determined by $\hat{\rho}(t_0)$. For problems with contours such as Figure 1.2b, their initial conditions are Green functions defined for all times smaller than t_0. For example, for thermal initial conditions, the preparatory stage of the system can be obtained via an inverse Wigner-Ville transform (cf. (1.25)) of the equilibrium 2-point function $G^{\gtrless}(\omega)$, calculated in real frequency (cf. Section 2.3.2)

$$G^{\gtrless}(T < t_0, \tau)_{\mathrm{W}} = \int \frac{\mathrm{d}\omega}{2\pi} e^{-i\omega\tau} G^{\gtrless}(\omega) \ , \tag{1.40}$$

followed by an inverse Wigner rotation (cf. (1.22)). Encoding the system's initial condition in such a manner precludes the use of mixed Green functions and can greatly simplify the complexity of the problem.

Equations of motion

Contour-ordered Green functions are nothing more than ensemble averages of operators in the Heisenberg picture, which obey the equations of motion

$$\frac{\mathrm{d}}{\mathrm{d}t}\left\langle \hat{O}(t)\right\rangle = \frac{\mathrm{d}}{\mathrm{d}t}\left\langle \hat{U}(t_0,t)\hat{O}(t)\hat{U}(t,t_0)\right\rangle = i\left\langle \left[\hat{H},\hat{O}(t)\right]\right\rangle + \dots \tag{1.41}$$

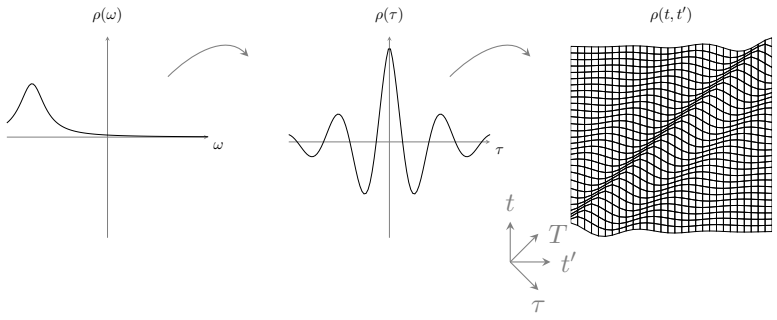

Figure 1.4: An inverse Wigner-Ville transformation followed by an inverse Wigner rotation of an equilibrium spectral function $\rho(\omega)$.

Nonetheless, calculating Green functions for an interacting $\hat{H}$ in this manner results in an infinite hierarchy of differential equations, with an ever-increasing order of operator averages. This hierarchy is known as Martin-Schwinger's, and while theoretically describing any many-body system exactly, it constitutes an intractable problem. Truncating the hierarchy via bare perturbative schemes in non-equilibrium settings can violate conservation laws due to spurious *secular* terms, which grow with time [24]. It also may not preserve non-linear features of the theory, which are necessary for coherent effects [53]. This non-linearity – e.g., self-consistency in the equations describing the system's dynamics – is ultimately related to the emergence of *universality*, where for $t \gg t_0$ the dynamics should be insensitive to the initial conditions, and the system may thermalise. A more sophisticated approach is required to address these issues appropriately.

1.4 Non-equilibrium two-particle-irreducible effective action

The n-particle-irreducible (nPI) effective actions are a class of field theories that provide practical and systematic approximations for classical [54] and quantum physics [24]. Their main advantage is that, unlike in bare perturbative approaches where all connected diagrams (graphs) contribute to the perturbative expansion, in nPI approaches, only nPI diagrams do – these are graphs that do not become disconnected once n lines are cut. Despite still being of perturbative nature, nPI approaches resum an infinite number of diagrams belonging to a particular class. The 2PI effective action is the simplest action [55] that both generates the non-linearity needed for the *universality* requirement of non-equilibrium theories and eliminates the spurious *secular* terms present in bare perturbative schemes. These ensure a *conserving* – also known as Φ-derivable [56, 57] – approximation where a series of conservation laws, such as conservation of particle number are fulfilled, despite truncations of the perturbative series.

1.4.1 Path-integral construction

The starting point is the construction of a functional path-integral representation of the partition function (cf. (1.8))

$$Z = \mathrm{tr}\left\{\hat{\rho}(t_0)\mathbb{T}_\gamma\left[e^{-i\int_\gamma \mathrm{d}\bar{t}\,\hat{H}(\bar{t})}\right]\right\} . \tag{1.42}$$

For the sake of brevity, γ is taken as the Keldysh contour (Figure 1.2a) – other contours, such as Konstantinov-Perel's (Figure 1.3) follows a similar derivation, however with more contour degrees

of freedom (Section 1.3.1). Considering a *normal-ordered*[7] Hamiltonian $H(t) = H\left[\hat{b}^\dagger(t), \hat{b}(t), t\right]$, the path integral is formulated via a Trotter-type limiting decomposition (1.3) of (1.42). A complete set

$$\mathbb{1} = \int \mathrm{d}\big[\phi^*, \phi\big]\ e^{-|\phi|^2}\, |\phi\rangle\, \langle\phi| \ , \tag{1.43}$$

of appropriately time-labelled coherent states[8] are inserted between the time-evolution operators of the Trotterized form of the partition function, with $\mathrm{d}[\phi^*, \phi] = \frac{\mathrm{d}\phi^*\, \mathrm{d}\phi}{2\pi i}$ for complex scalar and $\mathrm{d}[\phi^*, \phi] = \mathrm{d}\phi^*\, \mathrm{d}\phi$ for Grassmann fields. Expressing the trace as

$$\mathrm{tr}\, \hat{O} = \int \mathrm{d}\big[\phi^*, \phi\big]\ e^{-|\phi|^2}\, \langle\phi|\hat{O}|\phi\rangle \ , \tag{1.44}$$

this results in the discrete path-integral formulation

$$Z = \int \lim_{N\to\infty} \prod_{j=0}^{N-1} \mathrm{d}\Big[\phi^*_{j_+}, \phi_{j_+}\Big]\, \mathrm{d}\Big[\phi^*_{j_-}, \phi_{j_-}\Big]\, \langle\phi_{1_-}|\hat{\rho}(t_{-\infty})|\phi_{1_+}\rangle\, e^{iS[\phi]} \ , \tag{1.45}$$

with,

$$S[\phi] = \textstyle\sum_{j=1}^{N-1} \delta t_j \left[\left(+i\phi^*_{j_-} \frac{\phi_{j_-} - \phi_{j_- - 1}}{\delta t_j} - H\left[\phi^*_{j_-}, \phi_{j_- - 1}\right]\right) - \left(-i\phi^*_{j_+} \frac{\phi_{j_+} - \phi_{j_+ - 1}}{\delta t_j} - H\left[\phi^*_{j_+}, \phi_{j_+ - 1}\right]\right)\right] + i\phi^*_{(N-1)_+}\phi_{(N-1)_-} \ , \tag{1.46}$$

where $\delta t_j = t_j - t_{j-1}$ and $j_\mp$ denotes j-th Trotter slice, and the $-$ and $+$ subscripts denote the time forward and backward branches of the Keldysh contour, respectively. In the limit $N \to \infty$, ϕ is promoted to a *field* $\phi(z)$. The appearance of the last term in the discrete action S arises at the inflexion of the contour. Here, the field at $\phi(t_{N_-})$ and $\phi(t_{N_+})$ is indistinguishable, and hence there is no time evolution operator between the associated coherent states. The initial distribution of the system is encoded by $\hat{\rho}(t_0)$, for which can be shown [46, 47] that $\langle\phi_{0_-}|\hat{\rho}(t_0)|\phi_{0_+}\rangle = \exp\left(\xi\phi^*_{0_-}\phi_{0_+}\rho\right)$. Even though the Keldysh action in continuum form

$$S[\phi] = \int_\gamma \mathrm{d}z\, \phi^*(z) G^{-1}(z, z)\phi(z) \ , \tag{1.47}$$

where

$$G^{-1}(z, z') = \delta_\gamma(z, z')\left[i\partial_z - H(z)\right] \ , \tag{1.48}$$

appears to have both contour branches decoupled, that they are connected through the boundary terms of the discrete action. On a similar vein, $\delta_\gamma(z, z')$ is not a proper Dirac δ-distribution. The *causal* construction of the path-integral connects the fields between adjacent Trotterized slices of the path-integrals (1.46) and is technically defined as $\delta_\gamma(z, z' + 0^+)$.

1.4.2 Two-particle-irreducible effective action construction

Omitting the explicit dependence on the initial average and sourcing ϕ, considering it to be a multi-component field, the cumulant generating function W is defined as

$$Z\left[\boldsymbol{j}, \boldsymbol{K}\right] = \int D\boldsymbol{\phi} \exp\left\{i\left[S\left[\boldsymbol{\phi}\right] + \left(\boldsymbol{\phi}^*_z \boldsymbol{j}_z + \boldsymbol{j}^*_z \boldsymbol{\phi}_z\right) + \boldsymbol{\phi}^*_z \boldsymbol{K}_{zz'} \boldsymbol{\phi}_{z'}\right]\right\} \equiv e^{i\, W[\boldsymbol{j}, \boldsymbol{K}]} \ , \tag{1.49}$$

[7] A normal-ordered product of operators has all creation operators to the left of the annihilation operators.

[8] A coherent state $|\phi\rangle := e^{\xi\phi\hat{b}^\dagger}\, |0\rangle$ is the eigenstate of the annihilation operator $\hat{b}\, |\phi\rangle = \phi\, |\phi\rangle$, where $|0\rangle$ denotes the vacuum, with $\xi = 1$ for a complex scalar and $\xi = -1$ for a complex Grassmann number ϕ.

The n-point functions can be generated through functional derivatives with respect to the 1- and 2-point external source fields $\boldsymbol{j}$ and $\boldsymbol{K}$, obeying the same algebra as $\boldsymbol{\phi}$. Note the DeWitt notation where repeated, and continuous indices are integrated and summed over

$$\boldsymbol{j}_z\boldsymbol{\phi}_z = \sum_i \int_\gamma \mathrm{d}z\, j_i(z)\phi_i(z) \ . \tag{1.50}$$

The cumulant-generating functional $W\left[\boldsymbol{j},\boldsymbol{K}\right]$ generates the 1- and 2-point functions via

$$\xi\frac{\delta}{i\delta j_i(z)} iW\left[\boldsymbol{j},\boldsymbol{K}\right] = \overline{\phi^*}_i(z) \ , \tag{1.51a}$$

$$\frac{\delta}{i\delta j_i^*(z)} iW\left[\boldsymbol{j},\boldsymbol{K}\right] = \overline{\phi}_i(z) \ , \tag{1.51b}$$

$$\xi\frac{\delta}{i\delta K_{ij}(z,z')} iW\left[\boldsymbol{j},\boldsymbol{K}\right] \equiv iG_{ij}(z,z') \ , \tag{1.51c}$$

where the ξ factor arises due to the anti-commutative algebra of complex Grassmann fields (cf. (1.16)). Note that $G_{ij}(z,z')$ is not a second cumulant but a second *moment* of the quantum distribution. Even though these distinctions are often awkwardly overlooked[9] in many-body physics, there is an important distinction when characterising *correlations*, which becomes especially relevant for higher-order-point functions. Cumulants are the objects that describe *de facto* n-point interactions as they cannot be factorised into products of lower-order interactions. This has the formal consequence that when expressing an n-point interaction as a sum of graphs (Feynman diagrams), only *connected* graphs are considered. These cumulants are termed connected[10] n-point functions, $G^{(\mathrm{connected})}(z_1,\ldots,z_n)$, and are calculated via

$$\xi^n\frac{\delta}{i\delta j_{i_1}(z)}\cdots\frac{\delta}{i\delta j^*_{i_{2n}}(z_{2n})} iW\left[\boldsymbol{j},\boldsymbol{K}\right] = iG^{(\mathrm{connected})}_{i_1,\ldots,i_{2n}}(z_1,\ldots,z_{2n}) \ , \tag{1.52}$$

for which the alternative expression

$$G^{(\mathrm{connected})}_{ij}(z,z') = -i\xi\left[\frac{\delta}{i\delta K_{ij}(z,z')} iW\left[\boldsymbol{j},\boldsymbol{K}\right] - \overline{\phi}_i(z)\overline{\phi^*}_j(z')\right] \tag{1.53}$$

is deduced. The superscript (connected) will be dropped, and all n-point functions from this point onwards are considered connected.

In analogy with transformations in thermodynamics, a new generating functional describing the same physics can be formulated [53] depending on the conjugate variables $\overline{\boldsymbol{\phi}}$ and $\boldsymbol{G}$. The so-called two-particle-irreducible (2PI) effective action $\Gamma\left[\overline{\boldsymbol{\phi}},\boldsymbol{G}\right]$ is obtained through the triple Legendre transform

$$\begin{aligned}\Gamma\left[\overline{\boldsymbol{\phi}},\boldsymbol{G}\right] &= W\left[\boldsymbol{j},\boldsymbol{K}\right] - \textstyle\int_\gamma \mathrm{d}z\, \frac{\delta W[\boldsymbol{j},\boldsymbol{K}]}{\delta j_i(z)} j_i(z) - \int_\gamma \mathrm{d}z\, \frac{\delta W[\boldsymbol{j},\boldsymbol{K}]}{\delta j_i^*(z)} j_i^*(z) - \int_\gamma \mathrm{d}z\,\mathrm{d}z'\, \frac{\delta W[\boldsymbol{j},\boldsymbol{K}]}{\delta K_{ij}(z,z')} K_{ji}(z',z) \\ &= W\left[\boldsymbol{j},\boldsymbol{K}\right] - \overline{\boldsymbol{\phi}^*}_z\boldsymbol{j}_z - \boldsymbol{j}^*_z\overline{\boldsymbol{\phi}}_z - \overline{\boldsymbol{\phi}^*}_z\boldsymbol{K}_{zz'}\overline{\boldsymbol{\phi}}_{z'} - i\boldsymbol{G}_{zz'}\boldsymbol{K}_{z'z} \ .\end{aligned} \tag{1.54}$$

[9] This is rooted in the fact that in the absence of mean-fields – i.e., vanishing 1-point functions – the second cumulant and moment are identical. This equality always holds for 2-point functions of fermionic or bosonic fields with no condensate part. However, it does not generally hold for higher-order-point functions.

[10] In the jargon of field-theory, this terminology is intimately related to the linked-cluster theorem, where perturbative corrections to the nth cumulant are determined by connected graphs with n lines. Note that vacuum bubble diagrams are factored out through derivatives of $W\left[\boldsymbol{j},\boldsymbol{K}\right]$. Notwithstanding, n-point functions can still have disconnected contributions, i.e., products of lower-order point diagrams, which ought to be removed, resulting in *connected* n-point functions.

Apart from the advantageous functional dependence on the observables of interest, the 2PI effective action obeys a variational principle for vanishing sources $\boldsymbol{j}$ and $\boldsymbol{K}$. In this limit, the sourceless physical system is recovered, and the equation of motion for the 2-point functions is encoded as a stationary condition of the effective action,

$$\frac{\delta\Gamma\left[\overline{\boldsymbol{\phi}},\boldsymbol{G}\right]}{\delta\overline{\phi}_k(z)} = -\xi j_k^*(z) - \int_\gamma \mathrm{d}z'\,\overline{\phi^*}_i(z')K_{ik}(z',z) \tag{1.55a}$$

$$\frac{\delta\Gamma\left[\overline{\boldsymbol{\phi}},\boldsymbol{G}\right]}{\delta\overline{\phi^*}_k(z)} = -j_k(z) - \int_\gamma \mathrm{d}z'\,K_{kj}(z,z')\overline{\phi}_j(z') \tag{1.55b}$$

$$\frac{\delta\Gamma\left[\overline{\boldsymbol{\phi}},\boldsymbol{G}\right]}{\delta G_{kk'}(z,z')} = -iK_{k'k}(z',z)\ . \tag{1.55c}$$

The *effective action*, consisting of a classical action plus quantum corrections, is obtained by expanding [58] the original quantum fields $\boldsymbol{\phi}$ as a classical plus a fluctuation term $\boldsymbol{\phi} = \overline{\boldsymbol{\phi}} + \boldsymbol{\varphi}$,

$$\begin{aligned} e^{i\Gamma\left[\overline{\boldsymbol{\phi}},\boldsymbol{G}\right]} &= \exp\left\{iW\left[\boldsymbol{j},\boldsymbol{K}\right] - i\left(\overline{\boldsymbol{\phi}^*}_z\boldsymbol{j}_z + \boldsymbol{j}_z^*\overline{\boldsymbol{\phi}}_z + \overline{\boldsymbol{\phi}^*}_z\boldsymbol{K}_{zz'}\overline{\boldsymbol{\phi}}_{z'} + i\boldsymbol{G}_{zz'}\boldsymbol{K}_{z'z}\right)\right\} \\ &= \int D\boldsymbol{\varphi}\exp\left\{i\left[S\left[\overline{\boldsymbol{\phi}}+\boldsymbol{\varphi}\right] + \boldsymbol{\varphi}_z^*(\boldsymbol{j}_z + \boldsymbol{K}_{zz'}\overline{\boldsymbol{\phi}}_{z'}) + (\boldsymbol{j}_z^* + \overline{\boldsymbol{\phi}^*}_{z'}\boldsymbol{K}_{z'z})\boldsymbol{\varphi}_z + \boldsymbol{\varphi}_z^*\boldsymbol{K}_{zz'}\boldsymbol{\varphi}_{z'}\right]\right\} e^{\boldsymbol{K}_{zz'}\boldsymbol{G}_{z'z}}\ . \end{aligned} \tag{1.56}$$

At their core, nPI methods, much like most perturbative theoretical techniques, are based on splitting the action into a non-interacting part (bilinear in the fields) and an interacting part,

$$S\left[\boldsymbol{\phi}\right] = S_0\left[\boldsymbol{\phi}\right] + S_{\mathrm{int}}\left[\boldsymbol{\phi}\right] = \boldsymbol{\phi}_z^*\boldsymbol{G}^{-1}_{0_{zz'}}\boldsymbol{\phi}_{z'} + S_{\mathrm{int}}\left[\boldsymbol{\phi}\right]\ , \tag{1.57}$$

where

$$\boldsymbol{G}^{-1}_{0_{zz'}} = \delta_\gamma(z,z')\left[i\partial_z\mathbb{1} - \boldsymbol{h}_0(z)\right]\ , \tag{1.58}$$

and $\boldsymbol{h}_0(z)$ is the non-interacting part of the Hamiltonian $\boldsymbol{H}(z)$. For the sake of brevity, consider vanishing 1-point functions $\overline{\boldsymbol{\phi}} = \overline{\boldsymbol{\phi}^*} = 0$. The one-loop order 2PI effective action is obtained by discarding the interacting part and evaluating the complex Gaussian integral [24, 59, 60]

$$\Gamma^{(1\mathrm{loop})}\left[\boldsymbol{G}\right] = -i\xi\,\mathrm{tr}\log\left[i\left(\boldsymbol{G}_0^{-1} - \boldsymbol{K}\right)\right] - i\xi\,\mathrm{tr}\,\boldsymbol{K}\boldsymbol{G} = i\xi\,\mathrm{tr}\log i\boldsymbol{G} - i\xi\,\mathrm{tr}\left[\boldsymbol{G}_0^{-1}\boldsymbol{G}\right] + \mathrm{const}\ , \tag{1.59}$$

where (1.55c) was used to remove the explicit dependency on $\boldsymbol{K}$. Going beyond one loop, the 2PI effective action reads

$$\Gamma\left[\boldsymbol{G}\right] = i\xi\,\mathrm{tr}\log i\boldsymbol{G} - i\xi\,\mathrm{tr}\left[\boldsymbol{G}_0^{-1}\boldsymbol{G}\right] + \Gamma_2\left[\boldsymbol{G}\right] + \mathrm{const}\ . \tag{1.60}$$

The functional $\Gamma_2\left[\boldsymbol{G}\right]$ contains all contributions beyond one-loop, i.e., the sum of all scattering effects due to interactions (Section 1.4.4). For a theory with both bosonic (complex scalar) and fermionic (complex Grassmann) fields, the 2PI effective action can be written as

$$\Gamma\left[\boldsymbol{G},\boldsymbol{D}\right] = +i\,\mathrm{tr}\ln i\boldsymbol{G} - i\,\mathrm{tr}\,\boldsymbol{G}_0^{-1}\boldsymbol{G} - i\,\mathrm{tr}\ln i\boldsymbol{D} + i\,\mathrm{tr}\,\boldsymbol{D}_0^{-1}\boldsymbol{D} + \Gamma_2\left[\boldsymbol{G},\boldsymbol{D}\right] + \mathrm{const}\ , \tag{1.61}$$

where $\boldsymbol{G}$ denotes 2-point bosonic functions and $\boldsymbol{D}$ the fermionic 2-point functions, assuming that 1-point bosonic functions vanish.

1.4.3 Contour Dyson and Kadanoff-Baym equations

Deriving the equations of motion for the 1-point and 2-point functions through a variational procedure ensures that the global symmetries and conservation laws of the effective action are preserved. For vanishing source fields, these are given by the stationarity conditions of the 2PI effective action:

$$\frac{\delta\Gamma\left[\boldsymbol{G},\boldsymbol{D}\right]}{\delta\boldsymbol{G}} = 0 \ , \quad \frac{\delta\Gamma\left[\boldsymbol{G},\boldsymbol{D}\right]}{\delta\boldsymbol{D}} = 0 \ . \tag{1.62}$$

Notably, one finds the Dyson equations for the 2-point functions

$$G_{ij}^{-1}(z,z') = G_{0,ij}^{-1}(z,z';\overline{\phi}) - \Pi_{ij}(z,z';\overline{\phi},\boldsymbol{G},\boldsymbol{D}) \tag{1.63a}$$

$$D_{ij}^{-1}(z,z') = D_{0,ij}^{-1}(z,z';\overline{\phi}) - \Sigma_{ij}(z,z';\overline{\phi},\boldsymbol{G},\boldsymbol{D}) \ , \tag{1.63b}$$

where the self-energies $\boldsymbol{\Pi}$ and $\boldsymbol{\Sigma}$ are defined as

$$\Pi_{ij}(z,z') \equiv +i\frac{\delta\Gamma_2\left[\boldsymbol{G},\boldsymbol{D}\right]}{\delta G_{ji}(z',z)} \tag{1.64a}$$

$$\Sigma_{ij}(z,z') \equiv -i\frac{\delta\Gamma_2\left[\boldsymbol{G},\boldsymbol{D}\right]}{\delta G_{ji}(z',z)} \ . \tag{1.64b}$$

The Dyson equations are of little use for time-dependent non-equilibrium problems due to requiring the inversion of dense operators. While appropriate in equilibrium problems, where owing to time-translation invariance (Section 1.3.2), the equations become diagonal in the Fourier basis and can easily be inverted, this is far from the case in non-equilibrium where there is no symmetry in time. However, noting that

$$\boldsymbol{G}_{z\bar{z}}^{-1}\boldsymbol{G}_{\bar{z}z'} = \mathbb{1}_{zz'} \Leftrightarrow \int_{\bar{z}} G_{ik}^{-1}(z,\bar{z})G_{kj}(\bar{z},z') = \delta_\gamma(z,z')\delta_{ij} \ , \tag{1.65}$$

the equations can be transformed into an initial value problem:

$$\boldsymbol{G}_{0_{z\bar{z}}}^{-1}\boldsymbol{G}_{\bar{z}z'} = \mathbb{1}_{zz'} + \boldsymbol{\Pi}_{z\bar{z}}\boldsymbol{G}_{\bar{z}z'} \ , \tag{1.66a}$$

$$\boldsymbol{G}_{z\bar{z}}\boldsymbol{G}_{0_{\bar{z}z'}}^{-1} = \mathbb{1}_{zz'} + \boldsymbol{G}_{z\bar{z}}\boldsymbol{\Pi}_{\bar{z}z'} \ . \tag{1.66b}$$

Given the form of the inverse non-interacting 2-point functions (1.58), the resulting equations of motion are two-time integrodifferential equations, also known as the Kadanoff-Baym equations:

$$\left[i\vec{\partial}_z\mathbb{1} - \boldsymbol{h}_0(z)\right]\boldsymbol{G}(z,z') = \delta_\gamma(z,z')\mathbb{1} + \int_\gamma \mathrm{d}\bar{z}\,\boldsymbol{\Pi}(z,\bar{z})\boldsymbol{G}(\bar{z},z') \tag{1.67a}$$

$$\boldsymbol{G}(z,z')\left[-i\overleftarrow{\partial}_{z'}\mathbb{1} - \boldsymbol{h}_0(z')\right] = \delta_\gamma(z,z')\mathbb{1} + \int_\gamma \mathrm{d}\bar{z}\,\boldsymbol{G}(z,\bar{z})\boldsymbol{\Pi}(\bar{z},z') \ . \tag{1.67b}$$

The equations of motion for $\boldsymbol{D}(z,z')$ follow a similar derivation and structure.

A distinct feature of Kadanoff-Baym equations is their non-Markovian structure, evident from the integrals on the right-hand side of the integrodifferential equations (1.67). The appearance of such *memory* effects is a formal consequence that dynamics of (2-point) correlations can be fully described with knowledge from all other (2-point) correlations. This is a natural trade-off from the reduction of the state space from, e.g., the differential equations (1.41) generating the Martin-Schwinger hierarchy – with Markovian structure but dependence on *all* n-point functions. Similar to the equations generated by the hierarchy, the Kadanoff-Baym equations are formally exact. However, in practical terms, the exact calculation of Γ_2, which generates the self-energies, is an intractable problem.

1.4.4 Two-particle-irreducible loop expansion

Being a Legendre transform of the cumulant generating functional W, the 2PI effective action is an exact method and, in principle, contains the full information about the system. However, due to the great complexity of evaluating the Γ_2 functional exactly, approximations to the 2PI effective action arise from the truncation of Γ_2. By definition, Γ_2 contains all closed, topologically distinct, 2PI diagrams constructed from the bare vertices of the theory. This can succinctly [61] be expressed through

$$\Gamma_2\left[\boldsymbol{G},\boldsymbol{D}\right] = -i\left\langle \sum_{n=1}^{\infty} \frac{(iS_{\mathrm{int}})^n}{n!} \right\rangle_{\boldsymbol{G},\boldsymbol{D}\,\&2\mathrm{PI}}, \tag{1.68}$$

where $\langle\rangle_{\boldsymbol{G},\boldsymbol{D}\,\&2\mathrm{PI}}$ denotes that Wick's decomposition[11] is used to express the products of field operators into sums of products of pairs of field operators (2-point functions), that these 2-point functions are the connected Green functions $\boldsymbol{G}$ and $\boldsymbol{D}$, and that only 2PI vacuum bubble (closed) diagrams are considered.

The simplest Γ_2 truncation scheme is the loop expansion. This essentially mimics a coupling expansion, i.e., a perturbation expansion in powers of the interaction vertex, where a small coupling parameter $|V_0| \lesssim 1$ is required for convergence of the series. Since the Γ_2 diagrams are composed of the full, interacting $\boldsymbol{G}$ and $\boldsymbol{D}$, the self-consistency arising from the back-coupling to the self-energies (1.67) sums arbitrarily high powers of the coupling term. For illustrative purposes, consider S_{int}, containing the vertices of some theory with 3 quantum fields – c, f and b – in diagrammatical form:

$$iS_{\mathrm{int}} = \int_{\gamma} \mathrm{d}\bar{z}\left[V_0 c^*(\bar{z}) b^*(\bar{z}) f(\bar{z}) + \mathrm{h.\,c.}\right] =$$

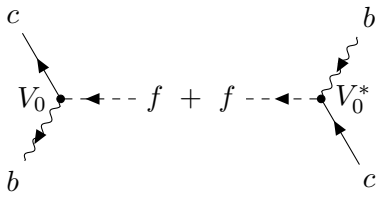

(1.69)

Given a specific power of iS_{int}, the vertices are connected in all possible ways, and all non-2PI diagrams are discarded, resulting in

$$\Gamma_2 = -i$$

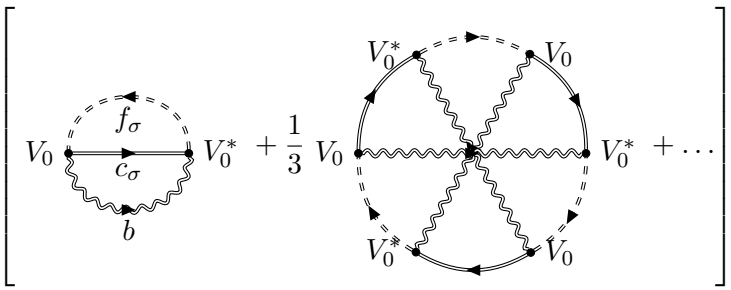

(1.70)

It can also be argued that due to the small coupling, higher-order diagrams will have a smaller contribution to the physics of the problem; hence, only the lowest order terms of Γ_2 have to be taken into account. Self-energy diagrams must be 1PI, which is fulfilled as the functional derivative required to calculate the self-energies (1.64a) amounts to cutting one line of the Γ_2 function graphs, which are 2PI by construction.

[11] The Wick theorem or decomposition is neatly understood in the path-integral formalism: for a *Gaussian* distribution – i.e., a non-interacting theory, any high-order moment can be decomposed in products of second moments (or cumulants). That is, $\langle X_1 X_2 \ldots X_{n-1} X_n\rangle = \sum_{p_n} \prod_{\{i,j\}\in p} \langle X_i X_j\rangle$ for even n and zero for odd n, where p_n denotes all possible ways of arranging $\{1,\ldots,n\}$ in pairs $\{i,j\}$.

Chapter 2

Auxiliary particles in non-equilibrium

The introduction of auxiliary particles dates back to the foundational work of Abrikosov [62], which introduced a faithful representation of spin-1/2 operators in terms of auxiliary fermionic operators. Unlike the former, which obey the SU(2) algebra and are incompatible with Wick's theorem, the latter obey canonical commutation relations and fully support standard diagrammatic techniques and saddle-point theories. Especially relevant to this thesis are the posterior works [63, 64] which introduced auxiliary bosonic particles to study *impurity* fermionic particles f subject to infinitely strong Coulomb repulsion. In such systems, the Coulomb interaction term can be dropped out of the Hamiltonian provided that the operator constraint

$$\sum_{\sigma} \hat{f}_{\sigma}^{\dagger} \hat{f}_{\sigma} \leq \hat{\mathbb{1}} \ , \tag{2.1}$$

holds, where σ denotes the local degrees of freedom of f, such as spin. Such non-holonomic constraints are of difficult analytic implementation but can be turned into holonomic constraints via the introduction of an auxiliary bosonic particle

$$\hat{f}_{\sigma}^{\dagger} \to \hat{f}_{\sigma}^{\dagger} \hat{b} \ , \tag{2.2}$$

while still retaining the original fermionic character

$$\left\{ \hat{f}_{\sigma}, \hat{f}_{\sigma'}^{\dagger} \right\} \to \left\{ \hat{b}^{\dagger} \hat{f}_{\sigma}, \hat{f}_{\sigma'}^{\dagger} \hat{b} \right\} \stackrel{!}{=} \delta_{\sigma\sigma'} \ , \tag{2.3}$$

if the operators are subject to the operator constraint

$$\hat{Q} := \hat{b}^{\dagger} \hat{b} + \sum_{\sigma} \hat{f}_{\sigma}^{\dagger} \hat{f}_{\sigma} = \hat{\mathbb{1}} \ . \tag{2.4}$$

Auxiliary-particle mappings such as (2.2) are generally not unique – in fact, for certain problems, there may be an infinite number of possible equivalent representations. However, this equivalence between representations can break down when approximations – such as diagrammatic truncations – are employed [25]. Since virtually any analytic calculation requires approximations, it is important that the auxiliary-particle mapping has a somewhat physical foundation. Only then can it be possible to infer whether the resulting approximation captures the relevant physical processes and is valid. These questions will be later explored regarding the physics resulting from saddle-point (Chapter 5) or diagrammatic truncations (Chapter 6) of theories relying on auxiliary particles.

Even though the use of auxiliary particles in non-equilibrium settings dates back to works in the early 1990s [65, 66], a proper extension to all contour-ordered Green function components was yet lacking. Despite modern attempts [67] at extending the formalism to the Konstantinov-Perel' contour (Figure 1.3), the auxiliary-particle formalism can be made much more transparent and complete, especially regarding thermal Green functions, which are necessary as initial conditions in the study of systems driven out of thermal equilibrium (Section 1.3.1).

2.1 Abrikosov's projection

The addition of auxiliary particles enlarges the original – or physical – Hilbert space with unphysical degrees of freedom which must be *projected* out. This is carried out by enforcing the constraint (2.4) via a projection technique [68], which generalized Abrikosov's [62] original proposal. Consider the grand-canonical ensemble related to the auxiliary-particle charge Q and associated chemical potential λ or fugacity $\zeta = e^{-\beta\lambda}$. By construction – or virtue of the Hamiltonian, each auxiliary-particle Fock space is disjoint, $\left[\hat{Q}, \hat{H}\right] = 0$, and hence the grand-canonical partition Z_ζ can be written as a sum over *canonical* partition functions $Z_Q \coloneqq \mathrm{tr}_{\mathcal{H}_Q} \hat{\rho}_0$,

$$Z_\zeta = \mathrm{tr}\left[\zeta^{\hat{Q}-\hat{\mathbb{1}}}\,\hat{\rho}_0\right] = \sum_{Q=0}^{\infty} \zeta^{Q-1} \operatorname*{tr}_{\mathcal{H}_Q} \hat{\rho}_0 = \zeta^{-1}\left[Z_0 + \zeta Z_1 + \mathcal{O}(\zeta^2)\right] \,, \tag{2.5}$$

where $\mathcal{H}_Q$ denotes the Hilbert space of the system in the auxiliary-particle Fock sector with charge Q. The grand-canonical ensemble average of some operator $\hat{O}$

$$\langle \hat{O} \rangle_\zeta \coloneqq \frac{\sum_{Q=0}^{\infty} \zeta^{Q-1}\, \mathrm{tr}_{\mathcal{H}_Q}\left[\hat{\rho}_0\, \hat{O}\right]}{Z_\zeta} \,, \tag{2.6}$$

can be related to the *physical* (constrained to the $\mathcal{H}_{Q=1}$ sector) canonical ensemble average via the fugacity limit

$$\langle \hat{O} \rangle_{\text{physical}} \coloneqq \frac{\mathrm{tr}_{\mathcal{H}_1}\left[\hat{\rho}_0\, \hat{O}\right]}{\mathrm{tr}_{\mathcal{H}_1}\, \hat{\rho}_0} \overset{!}{\equiv} \lim_{\zeta\to 0} \frac{\langle \hat{O}\, \hat{Q} \rangle_\zeta}{\langle \hat{Q} \rangle_\zeta} = \lim_{\zeta\to 0} \frac{\cancelto{0}{\mathrm{tr}_{\mathcal{H}_0}\left[\hat{\rho}_0 \hat{O} \hat{Q}\right]} + \zeta\, \mathrm{tr}_{\mathcal{H}_1}\left[\hat{\rho}_0\, \hat{O}\, \hat{Q}\right] + \mathcal{O}(\zeta^2)}{\cancelto{0}{\mathrm{tr}_{\mathcal{H}_0}\left[\hat{\rho}_0 \hat{Q}\right]} + \zeta\, \mathrm{tr}_{\mathcal{H}_1}\left[\hat{\rho}_0\, \hat{Q}\right] + \mathcal{O}(\zeta^2)} \,. \tag{2.7}$$

This equation is at the heart of the formalism and relates a canonical ensemble average in a constrained Hilbert space with an unconstrained grand canonical one, taken in some particular limit. All its constituents play an essential role – for example, $\langle Q \rangle_\zeta$ is not *just* another constant and will play a critical role in determining leading-order diagrams.

Note that an impurity operator $\hat{O}_{\text{imp}}$ acting on the physical Hilbert space must be transformed to an operator acting on the enlarged Hilbert space, e.g., the prototypical $\hat{O}_{\text{imp}} = \hat{f}^\dagger \hat{f} \equiv \hat{f}^\dagger \hat{b} \hat{b}^\dagger \hat{f}$. Such *normal-ordered* auxiliary-particle operators annihilate the $Q = 0$ sector by construction due to the presence of an auxiliary-particle annihilation operator on the right. Because of this, $\hat{Q}$ can be dropped out of the numerator – since its purpose was to annihilate $\mathcal{H}_{Q=0}$, and the projection (2.7) reduces to

$$\langle \hat{O}_{\text{imp}} \rangle_{\text{physical}} \equiv \lim_{\zeta\to 0} \frac{\langle \hat{O}_{\text{imp}} \rangle_\zeta}{\langle \hat{Q} \rangle_\zeta} \,. \tag{2.8}$$

However, the same does *not* apply to non-impurity operators, and the projection (2.7) must be considered. Now that it is known how to orchestrate some grand-canonical ensemble averages to obtain a constrained canonical ensemble average, all remaining is to determine the expressions or equations of motion for said grand-canonical ensemble averages.

2.2 ζ-scaling of contour-ordered Green functions

The projection (2.7) solely requires grand-canonical ensemble averages in the $\zeta \to 0$ limit. For this reason, any expression that can be expanded in powers of ζ will be taken only to the leading order. The contour-ordered Green function (1.18) of auxiliary particles

$$\begin{aligned} G_\zeta(z,z') &= \Theta_\gamma(z,z')G^>_\zeta(z,z') + \Theta_\gamma(z',z)G^<_\zeta(z,z') \\ &= \Theta_\gamma(z,z')\frac{\mathrm{tr}_{\mathcal{H}_0}\left[\hat\rho_0\,(-i)\hat f(z)\hat f^\dagger(z')\right]+\mathcal{O}(\zeta)}{Z_\zeta} + \Theta_\gamma(z',z)\frac{\zeta\,\mathrm{tr}_{\mathcal{H}_1}\left[\hat\rho_0\,(-i\xi)\hat f^\dagger(z')\hat f(z)\right]+\mathcal{O}(\zeta^2)}{Z_\zeta} \\ &= \Theta_\gamma(z,z')\left[G^>_{\zeta,\mathcal{H}_0}(z,z')+\mathcal{O}(\zeta)\right] + \Theta_\gamma(z',z)\left[\zeta G^<_{\zeta,\mathcal{H}_1}(z,z')+\mathcal{O}(\zeta^2)\right]\ , \end{aligned} \tag{2.9}$$

now displays a key feature of the grand-canonical formalism: the greater and lesser components have *different* ζ-scaling. In the limit $\zeta \to 0$, the greater function is only traced in the $Q = 0$ sector, and as a result, it does not carry information about particle occupation and hence only spectral information. Similarly, spectral functions such as the retarded Green function reduce to

$$\lim_{\zeta\to0} G^R_\zeta(t,t') = \lim_{\zeta\to0}\Theta(t-t')\left[G^>_\zeta(t,t')-G^<_\zeta(t,t')\right] = \lim_{\zeta\to0}\Theta(t-t')G^>_\zeta(t,t')\ . \tag{2.10}$$

Note that this unusual result is not some esoteric property of auxiliary particles but simply a formal *consequence* of taking the grand-canonical ensemble average in the $\zeta \to 0$ limit, a requirement of the projection (2.7) to the physical Hilbert space. Note, however, that non-auxiliary-particle Green functions always scale as $\mathcal{O}(1)$ and hence do not fulfil such relations.

2.2.1 Kadanoff-Baym equations

The rather unusual $\zeta \to 0$ limit results in a modified set of Langreth rules (1.37) that directly enter the Kadanoff-Baym equations of motion (1.67) for ζ-scaled contour-ordered Green functions of auxiliary particles. This follows from keeping only the leading ζ terms of the ζ-decomposition of contour-ordered Green functions (2.9) and self-energies

$$\begin{aligned} \int_\gamma \mathrm{d}\bar z\,\Sigma_\zeta(z,\bar z)G_\zeta(\bar z,z') = \Theta_\gamma(z,z')\underbrace{\int_{z'}^{z}\mathrm{d}\bar z\,\Sigma^>_\zeta(z,\bar z)G^>_\zeta(\bar z,z')}_{\text{at least }\mathcal{O}(1)} + \Theta_\gamma(z',z)\underbrace{\int_{z}^{z'}\mathrm{d}\bar z\,\Sigma^<_\zeta(z,\bar z)G^<_\zeta(\bar z,z')}_{\text{at least }\mathcal{O}(\zeta^2)} \\ \underbrace{+\int_{t_0}^{\min_\gamma(z,z')}\mathrm{d}\bar z\,\Sigma^>_\zeta(z,\bar z)G^<_\zeta(\bar z,z') + \int_{\max_\gamma(z,z')}^{t_0-i\beta}\mathrm{d}\bar z\,\Sigma^<_\zeta(z,\bar z)G^>_\zeta(\bar z,z')}_{\text{at least }\mathcal{O}(\zeta)}\ . \end{aligned} \tag{2.11}$$

The following analyses will consider that the auxiliary-particle self-energies have at least the *same* ζ-scaling as the contour-ordered Green functions. Note, however, that the ζ-scaling of the self-energy of non-auxiliary particles is model-dependent and cannot be inferred a priori.

For a Green function with real-time arguments $(z, z') \to (t, t')$, the equations of motion reduce to

$$\lim_{\zeta\to 0}\left[i\partial_t - h_0(t)\right] G^{\gtrless}_\zeta(t,t') = \lim_{\zeta\to 0}\left\{\int_{t'}^{t} \mathrm{d}\bar{t}\, \Sigma^{\gtrless}_\zeta(t,\bar{t}) G^{\gtrless}_\zeta(\bar{t},t') + \mathcal{O}(\zeta)\right\} \tag{2.12a}$$

$$\begin{aligned}\lim_{\zeta\to 0}\left[i\partial_t - h_0(t)\right] G^{<}_\zeta(t,t') = \lim_{\zeta\to 0}\Bigg\{ &\int_{t_0}^{t} \mathrm{d}\bar{t}\, \Sigma^{>}_\zeta(t,\bar{t}) G^{<}_\zeta(\bar{t},t') - \int_{t_0}^{t'} \mathrm{d}\bar{t}\, \Sigma^{<}_\zeta(t,\bar{t}) G^{>}_\zeta(\bar{t},t') \\ &+ \int_{t_0}^{t_0-i\beta} \mathrm{d}\bar{\tau}\, \Sigma^{\rceil}_\zeta(t,\bar{\tau}) G^{\lceil}_\zeta(\bar{\tau},t') + \mathcal{O}(\zeta^2)\Bigg\} .\end{aligned} \tag{2.12b}$$

2.2.2 Gaussian initial conditions

For an arbitrary non-thermal initial density matrix, the thermal-branch integral of (2.12b) is zero – since, by definition, it only arises from the extension of the Keldysh contour to imaginary times for a thermal initial density matrix (Section 1.2.2). Despite the ζ-term appearing to be temperature dependent – which is a useful construction for Section 2.3, in the absence of a definition of temperature, as in arbitrary density matrices, this detail can be ignored as long as the proper ζ limit is considered. For a Gaussian initial density matrix $\hat{\rho}_0 = \kappa^{\hat{Q}}$, the boundary term in the path integral quantum field theory (Section 1.4.1) that encodes the initial distribution is instead the expectation value of $\lim_{\zeta\to 0} \zeta^{\hat{Q}}\kappa^{\hat{Q}}$ – due to a different definition of the ensemble average (cf. (2.6)), and the initial conditions read [46, 47, 69]

$$\lim_{\zeta\to 0} G^{>}_\zeta(t_0,t_0) = \lim_{\zeta\to 0}\left[-i\left(1 + \xi\frac{\zeta\kappa}{1-\zeta\kappa}\right)\right] = -i \tag{2.13a}$$

$$\lim_{\zeta\to 0} G^{<}_\zeta(t_0,t_0) = \lim_{\zeta\to 0}\left[-i\xi\frac{\zeta\kappa}{1-\zeta\kappa}\right] . \tag{2.13b}$$

2.3 λ-scaling of thermal Green functions

The application of the decomposition (2.9) equation of motion of the Matsubara Green function $\mathcal{G}_\zeta(\tau,\tau')$ truncates the thermal-branch integral in the $\zeta \to 0$ limit [67]. However, due to the convenient analytic properties of Matsubara frequencies, it is worthwhile to keep the full integral. For that, instead of treating the grand-canonical ensemble average as a ζ-expansion (2.6), consider the equivalent λ-expansion for an initial thermal density matrix

$$\langle\hat{O}\rangle_\zeta \equiv \langle\hat{O}\rangle_\lambda := \frac{\mathrm{tr}\left[e^{-\beta\left(\hat{\mathcal{H}}+\lambda\left(\hat{Q}-\hat{1}\right)\right)}\hat{O}\right]}{\mathrm{tr}\left[e^{-\beta\left(\hat{\mathcal{H}}+\lambda\left(\hat{Q}-\hat{1}\right)\right)}\right]} . \tag{2.14}$$

The auxiliary chemical potential enters directly in the non-interacting part of the auxiliary-particle Hamiltonian (cf. (1.14)), and the right-hand-side of the equation of motion follows standard Langreth rules (1.37)

$$\lim_{\lambda\to\infty}\left[-\partial_\tau - h_0 - \lambda\right]\mathcal{G}_\lambda(\tau,\tau') = i\delta(\tau-\tau') - i\lim_{\lambda\to\infty}\left\{\int_0^\beta \mathrm{d}\bar{\tau}\, \Sigma_\lambda(\tau,\bar{\tau})\mathcal{G}_\lambda(\bar{\tau},\tau')\right\} . \tag{2.15}$$

Note that Σ_λ here denotes the Matsubara self-energy $\Sigma_\lambda(\tau,\tau') \coloneqq \Sigma_\lambda(t_0-i\tau, t_0-i\tau')$. Leveraging the translational symmetry $\mathcal{G}_\lambda(\tau,\tau') \equiv \mathcal{G}_\lambda(\tau-\tau')$ and the (anti)periodicity $\mathcal{G}_\lambda(\tau+\beta,\tau') = \xi\,\mathcal{G}_\lambda(\tau,\tau')$ of the Matsubara functions – which follows directly from their definition (1.16), the imaginary-time integrals can be replaced by products in Matsubara frequencies $i\omega_n$

$$\mathcal{G}_\lambda(\tau) = \frac{i}{\beta}\sum_{i\omega_n} e^{-i\omega_n\tau}\mathcal{G}_\lambda(i\omega_n) \qquad \mathcal{G}_\lambda(i\omega_n) = -i\int_0^\beta \mathrm{d}\tau e^{i\omega_n\tau}\mathcal{G}_\lambda(\tau)\ , \tag{2.16}$$

where $i\omega_n = (2n)\pi/\beta$ or $i\omega_n = (2n+1)\pi/\beta$ for bosonic or fermionic Green functions, respectively. Thus,

$$\lim_{\zeta\to 0}\mathcal{G}_\zeta(i\omega_n) \equiv \lim_{\lambda\to\infty}\mathcal{G}_\lambda(i\omega_n) = \lim_{\lambda\to\infty}\left[i\omega_n - h_0 - \lambda - \Sigma_\lambda(i\omega_n)\right]^{-1}\ . \tag{2.17}$$

The mixed Green functions have similar properties in the imaginary time and hence can also be expressed in terms of Matsubara frequencies

$$\lim_{\lambda\to\infty}\left[i\partial_t - h(t)\right]G^{\rceil}_\lambda(t,i\omega_n) = \lim_{\lambda\to\infty}\left\{\int_{t_0}^t \mathrm{d}\bar{t}\,\left[\Sigma^{>}_\lambda(t,\bar{t}) - \Sigma^{<}_\lambda(t,\bar{t})\right]G^{\rceil}_\lambda(\bar{t},i\omega_n) + \Sigma^{\rceil}_\lambda(t,i\omega_n)\mathcal{G}_\lambda(i\omega_n)\right\}\ , \tag{2.18}$$

with an analogous equation of motion for $G^{\lceil}(i\omega_n,t)$.

2.3.1 Analytic continuation

A series of formal analytic relations between Green functions, namely the analytic continuation [70] of complex time arguments, such as the Matsubara time τ and frequencies $i\omega_n$ to real-time or frequency, can be obtained via the Lehmann representation, which is an expansion of the ensemble average over the complete set of eigenstates of the Hamiltonian. Consider the Lehmann representation of the mixed Green function (1.16)

$$\begin{aligned}
G^{\lceil}_\lambda(i\omega_n,t) &= -i\int_0^\beta \mathrm{d}\tau\, e^{+i\omega_n\tau}G^{\lceil}_\lambda(\tau,t) \\
&= -i\int_0^\beta \mathrm{d}\tau\, e^{+i\omega_n\tau}\left[-i\xi\frac{1}{Z}\sum_{nn'}\langle n|e^{-(\hat{\mathcal{H}}+\lambda\hat{Q})(\beta-\tau)}\hat{d}^\dagger|n'\rangle\,\langle n'|e^{-(\hat{\mathcal{H}}+\lambda\hat{Q})\tau}\hat{d}(t)|n\rangle\right] \\
&= -i\frac{1}{Z}\sum_{nn'}\langle n|\hat{d}^\dagger|n'\rangle\,\langle n'|\hat{d}(t)|n\rangle\, e^{-\beta E^\lambda_n}\left[-i\xi\int_0^\beta \mathrm{d}\tau\, e^{(+i\omega_n+E^\lambda_n-E^\lambda_{n'})\tau}\right] \\
&= -\frac{1}{Z}\sum_{nn'}\frac{\langle n'|\hat{d}^\dagger|n\rangle\,\langle n|\hat{d}(t)|n'\rangle}{i\omega_n + E^\lambda_n - E^\lambda_{n'}}\left[\xi e^{-\beta E^\lambda_{n'}} - e^{-\beta E^\lambda_n}\right]\ .
\end{aligned} \tag{2.19}$$

Likewise, it can be shown that $G^{\rceil}_\lambda(i\omega_n,t) = G^{\lceil}_\lambda\left(t,(i\omega_n)^*\right)^\dagger$ and hence only one of the two mixed Green functions needs to be considered. But more surprisingly, it also follows from the Lehmann representation that $G^{\rceil}_\lambda(i\omega_n,t_0) = \mathcal{G}_\lambda(i\omega_n)$. Similarly to the Matsubara Green function $\mathcal{G}_\lambda(z)$, the mixed Green functions are also analytical everywhere in the complex plane, except on the real axis, where they have a branch cut and $\mathcal{G}_\lambda(i\omega_n\to\omega\mp i\eta) \overset{!}{=} G^{A/R}_\lambda(\omega)$ [71]. So although appearing in form as greater/lesser Green functions, the analytically-continued mixed Green functions are instead related to the advanced/retarded Green functions. These would be equivalent to Wigner-Ville-transforming the ones presented in Section 1.3, assuming thermal equilibrium conditions.

2.3.2 Dyson and Kadanoff-Baym equations

Dyson equations

A solution of the Green functions in *real-frequency* can be obtained directly from the analytic continuation of the Matsubara Dyson equation (2.17)

$$\lim_{\lambda\to\infty} G^{A/R}_\lambda(\omega+\lambda) = \lim_{\lambda\to\infty}\left[\omega - h_0 - \Sigma^{A/R}_\lambda(\omega+\lambda)\right]^{-1} , \tag{2.20}$$

for which $G^A_\lambda(\omega)^\dagger = G^R_\lambda(\omega)$. The real-frequency greater/lesser Green functions are connected through the fluctuation-dissipation relation

$$\lim_{\lambda\to\infty} G^<_\lambda(\omega+\lambda) = \lim_{\lambda\to\infty} \xi\, e^{-\beta(\omega+\lambda)} G^>_\lambda(\omega+\lambda) . \tag{2.21}$$

However, due to the λ limit, the exponential term usually diverges *numerically* and, unlike standard thermal equilibrium techniques, both Green function components should be calculated independently. Whereas the real-frequency greater component in the λ-limit can be directly obtain through (2.10) and (2.20), the definition of the lesser component $G^<_\lambda(\omega+\lambda)$ follows from the property $a-b = a(b^{-1}-a^{-1})b$ and (2.21)

$$\begin{aligned} G^<_\lambda(\omega+\lambda) &\coloneqq G^R_\lambda(\omega+\lambda)\left[\xi\, e^{-\beta(\omega+\lambda)}\left(\Sigma^R_\lambda(\omega+\lambda) - \Sigma^A_\lambda(\omega+\lambda)\right)\right] G^A_\lambda(\omega+\lambda) \\ &= G^R_\lambda(\omega+\lambda)\Sigma^<_\lambda(\omega+\lambda)G^A_\lambda(\omega+\lambda) . \end{aligned} \tag{2.22}$$

Kadanoff-Baym equations

Similarly, the real-frequency mixed and complementary lesser Green function can be defined as

$$G^\rceil_\lambda(t,\omega) \coloneqq G^\rceil_\lambda(t, i\omega_n \to \omega + i\eta) \tag{2.23a}$$

$$G^<_\lambda(t,\omega) \coloneqq \xi\, e^{-\beta(\omega+\lambda)}\left[G^\rceil_\lambda(t,\omega) - G^\rceil_\lambda(t,\omega)^\dagger\right] , \tag{2.23b}$$

and follow the equations of motion

$$\lim_{\lambda\to\infty}\left[i\partial_t - h(t)\right] G^\rceil_\lambda(t,\omega) = \lim_{\substack{\zeta\to 0\\ \lambda\to\infty}}\left\{\int_{t_0}^t \mathrm{d}\bar{t}\, \Sigma^>_\zeta(t,\bar{t})G^\rceil_\lambda(\bar{t},\omega) + \Sigma^\rceil_\lambda(t,\omega)G^\rceil_\lambda(t_0,\omega) + \mathcal{O}(\zeta)\right\} \tag{2.24a}$$

$$\begin{aligned} \lim_{\lambda\to\infty}\left[i\partial_t - h(t)\right] G^<_\lambda(t,\omega) = \lim_{\substack{\zeta\to 0\\ \lambda\to\infty}}\Bigg\{ &\int_{t_0}^t \mathrm{d}\bar{t}\, \Sigma^>_\zeta(t,\bar{t})G^<_\lambda(\bar{t},\omega) \\ &+ \Sigma^<_\lambda(t,\omega)G^\rceil_\lambda(t_0,\omega)^\dagger + \Sigma^\rceil_\lambda(t,\omega)G^<_\lambda(t_0,\omega) + \mathcal{O}(\zeta^2)\Bigg\} . \end{aligned} \tag{2.24b}$$

Finally, the thermal collision integral appearing in the equation of motion (2.12b) of the lesser Green function $G_\zeta(t,t')$ can be calculated as

$$\begin{aligned} &\lim_{\zeta\to 0}\int_{t_0}^{t_0-i\beta} \mathrm{d}\bar{\tau}\, \Sigma^\rceil_\zeta(t,\bar{\tau})G^\lceil_\zeta(\bar{\tau},t') = \lim_{\lambda\to\infty}\frac{i}{\beta}\sum_{i\omega_n}\Sigma^\rceil_\lambda(t,i\omega_n)G^\lceil_\lambda(i\omega_n,t)e^{-i\omega_n 0^+} \\ &= \lim_{\lambda\to\infty}\int_{-\infty}^{+\infty}\frac{\mathrm{d}\omega}{2\pi}\left[\Sigma^<_\lambda(t,\omega+\lambda)G^\rceil(t',\omega+\lambda)^\dagger + \Sigma^\rceil_\lambda(t,\omega+\lambda)G^<(t',\omega+\lambda)\right] . \end{aligned} \tag{2.25}$$

2.3.3 Thermal initial conditions

Since the λ-scaling is formulated through a *thermal* density matrix, it is only valid for thermal-related observables. This is the case of thermal initial conditions (1.39) for the Kelysh greater/lesser components of the Konstantinov-Perel' contour (Figure 1.3), which read

$$\begin{aligned}
\lim_{\zeta\to 0} G^{>}_{\zeta}(t_0,t_0) &= \lim_{\lambda\to\infty} \mathcal{G}_\lambda(0^+,0) = \lim_{\lambda\to\infty} \frac{i}{\beta}\sum_n e^{-i\omega_n 0^+}\mathcal{G}_\lambda(i\omega_n) \\
&= \lim_{\lambda\to\infty}\int_{-\infty}^{+\infty}\frac{\mathrm{d}\omega}{2\pi}\left[1+\xi\, n(\omega)\right]\left[G^R_\lambda(\omega)-G^A_\lambda(\omega)\right] \qquad (2.26a)\\
&= \lim_{\lambda\to\infty}\int_{-\infty}^{+\infty}\frac{\mathrm{d}\omega}{2\pi}\left[G^R_\lambda(\omega+\lambda)-G^A_\lambda(\omega+\lambda)\right] + \lim_{\zeta\to 0}\mathcal{O}(\zeta) \\
\lim_{\zeta\to 0} G^{<}_{\zeta}(t_0,t_0) &= \lim_{\lambda\to\infty} \mathcal{G}_\lambda(0,0^+) = \lim_{\lambda\to\infty} \frac{i}{\beta}\sum_n e^{+i\omega_n 0^+}\mathcal{G}_\lambda(i\omega_n) \\
&= \lim_{\lambda\to\infty}\int_{-\infty}^{+\infty}\frac{\mathrm{d}\omega}{2\pi}\xi\, n(\omega)\left[G^R_\lambda(\omega)-G^A_\lambda(\omega)\right] \qquad (2.26b)\\
&= \lim_{\lambda\to\infty}\int_{-\infty}^{+\infty}\frac{\mathrm{d}\omega}{2\pi}\xi\, e^{-\beta(\omega+\lambda)}\left[G^R_\lambda(\omega+\lambda)-G^A_\lambda(\omega+\lambda)\right] + \lim_{\zeta\to 0}\mathcal{O}(\zeta^2)\ ,
\end{aligned}$$

where

$$\lim_{\lambda\to\infty} n\,(\omega+\lambda) = \lim_{\lambda\to\infty} e^{-\beta(\omega+\lambda)}\frac{1}{1-\xi\, e^{-\beta(\omega+\lambda)}} = \lim_{\zeta\to 0}\left[\zeta\, e^{-\beta\omega}+\mathcal{O}(\zeta^2)\right]\ . \qquad (2.27)$$

Note that the ζ-scaling is not *explicitly* encoded in the real-frequency Green functions, but on how the non-interacting energy of the auxiliary particles being at infinity effectively modifies the distribution functions.

The initial conditions for the mixed Green functions follow directly from the boundary condition (1.39) at $t = t_0$

$$G^{\rceil}_\lambda(t_0,\omega) = G^R_\lambda(\omega)\ , \qquad (2.28a)$$
$$G^{<}_\lambda(t_0,\omega) = G^{<}_\lambda(\omega)\ . \qquad (2.28b)$$

Chapter 3

Numerical solution of Kadanoff-Baym equations

Contribution statement This Chapter is based on the section "Numerical solution of Kadanoff-Baym equations" of the following article F. Meirinhos, M. Kajan, J. Kroha, and T. Bode, "Adaptive Numerical Solution of Kadanoff-Baym Equations", SciPost Phys. Core **5** (2022) DOI: 10.21468/SciPostPhysCore.5.2.030 which is presented here with minor editorial changes and with the formatting is adapted to match the thesis style. Such reproduction is permitted as the journal articles published by SciPost are licensed under the *Creative Commons Attribution 4.0 International (CC BY 4.0)* license, which allows adaptation, reproduction and redistribution of the original source for any purpose, as long as the licence terms are followed. In [32], the concept of adaptivity in the numerical solution of ordinary differential equations is extended to Kadanoff-Baym equations, which are two-time (integro)differential equations that arise as equations of motion of non-equilibrium 2-point functions. Ensuring the time-step size is large can dramatically increase the numerically-accessible integration times since the complexity of the numerical solution of Kadanoff-Baym equations scales at least cubically and quadratically in the number of time steps, regarding numerical operations and memory requirements, respectively. Following rather well-established literature on the numerical solution of non-stiff ordinary differential equations, adaptivity is implemented in the control of the time-step size and the order of the interpolation polynomials. The former ensures the time-step size is optimal – i.e., as large as possible – given the tolerance criteria, and the latter ensures the polynomial order that incurs the least amount of local error is chosen. This is achieved by mapping a discretised two-time to a one-time stepping scheme and standard adaptivity algorithms and heuristics. It is shown how an adaptive scheme in the numerical solution of 2-point functions in time has a significant edge over fixed step-size/order schemes at a minimal computational and implementation overhead. First, it is observed that an adaptive time-stepping scheme can successfully integrate an exactly solvable model in considerably fewer time steps than a fixed scheme while incurring a smaller global error. Second, it is shown that an adaptive time-stepper effectively changes the time-step size in time regions where, for example, a stronger drive is acting on the system, and the integrator should step slower to keep the local error small. In this example, an overall factor of 5 between the smallest and largest time step critically accelerates the numerical integration. This adaptiveness could be particularly beneficial in studying transients such as non-equilibrium quenches, where there is a violent change in the system at early times, which induces rapid changes and hence requires small time steps. Afterwards, this is typically followed by a pre-thermalisation regime, where the system changes slowly while evolving towards an equilibrium state. The evolution to

an equilibrium state should permit larger time steps since the dynamics are almost static in the centre-of-mass direction. Note, however, that the adaptivity is not formulated in Wigner coordinates (Section 1.3.2) and hence slow time evolution in the centre-of-mass direction cannot be fully leveraged. The versatility of the adaptive scheme is tested in several physical models, ranging from quantum to classical stochastic systems. Moreover, within the quantum systems, the adaptive algorithm is tested in fermionic tight-binding and Fermi-Hubbard models as well as in bosonic mixture and open boson dimer models. Within the publication [32], I was responsible for developing the adaptive scheme's idea, theory and numerical implementation. Furthermore, I wrote several parts of the text and took part in developing and analysing the examples provided. Specifically, within the section "Numerical solution of Kadanoff-Baym equations", transcribed in this Chapter, I was responsible for the entirety of its contents.

The computation of solutions to the Kadanoff-Baym equations consists formally in finding numerical solutions to an integrodifferential equation of the form

$$i\partial_t g(t,t') = h_0(t)g(t,t') + \int_{\gamma'} \mathrm{d}\bar{t}\, K(t,\bar{t})g(\bar{t},t') \;, \tag{3.1}$$

which, together with its adjoint, spans the entire (t,t') plane. Note that $g(t,t')$ and the kernel $K(t,t')$ are assumed to be either skew-Hermitian or symmetric with respect to their arguments. While at first glance (3.1) may look like a Fredholm integral equation [72], in physical systems the integrals $\int_{\gamma'} \mathrm{d}\bar{t}$ are always reduced to Volterra form, i.e. $\gamma' = [t_0, t]$ or $\gamma' = [t_0, t']$ (cf. (1.37)), the deeper reason for this being causality. Since K is usually a functional of g, (3.1) belongs to the class of generic non-linear Volterra integrodifferential equations (VIDE). For the rest of the analysis, assume that the integral kernel is smooth and non-singular, as the converse is rarely encountered in the class of physical problems considered here and would require problem-dependent modifications of the quadrature rules to be properly accounted for [73].

The fact that the VIDE (3.1) is defined on a two-dimensional domain has not only obfuscated its analysis it has also impeded a direct application of most existing numerical algorithms, which have primarily been focused on univariate VIDEs. An appropriate discretisation scheme is presented, which allows the application of general linear methods for solving the Kadanoff-Baym equations and an exposition of the variable Adams method, the preferred multi-step method for solving these equations.

3.1 Stepping Scheme for Kadanoff-Baym Equations

Due to the causal structure of the Volterra initial-value problem, the Kadanoff-Baym equation at the point (t,t') is only dependent on time arguments smaller or equal to (t,t'). By taking the Cartesian product of a (non-equidistant) one-dimensional grid

$$\mathcal{T} \coloneqq \{t_0 < t_1 < \ldots < t_i < \ldots < t_N\} \tag{3.2}$$

with itself, a symmetric mesh $\mathcal{T} \times \mathcal{T} = \big\{(t,t') \mid t \in \mathcal{T}, t' \in \mathcal{T}\big\}$ for the two-time domain is obtained. Within such a discretisation, the time-stepping procedure can be regarded as a fan-like stepping in the symmetric two-time mesh, as depicted in Figure 3.1. Accordingly, this can be understood as a system of *univariate*, vector-valued differential equations

$$\begin{aligned}
i\partial_{t_i}\mathbf{g}^v(t_i) &= h_0(t_i)\mathbf{g}^v(t_i) + (\mathbf{K}\circ\mathbf{g})^v(t_i) && \text{(vertical step)} \\
-i\partial_{t_i}\mathbf{g}^h(t_i) &= \mathbf{g}^h(t_i)h_0(t_i)^\dagger + (\mathbf{g}\circ\mathbf{K})^h(t_i) && \text{(horizontal step)} \\
i\partial_{t_i}\mathbf{g}^d(t_i) &= h_0(t_i)\mathbf{g}^d(t_i) - \mathbf{g}^d(t_i)h_0(t_i)^\dagger + (\mathbf{K}\circ\mathbf{g} - \mathbf{g}\circ\mathbf{K})^d(t_i) && \text{(diagonal step)} \;,
\end{aligned} \tag{3.3}$$

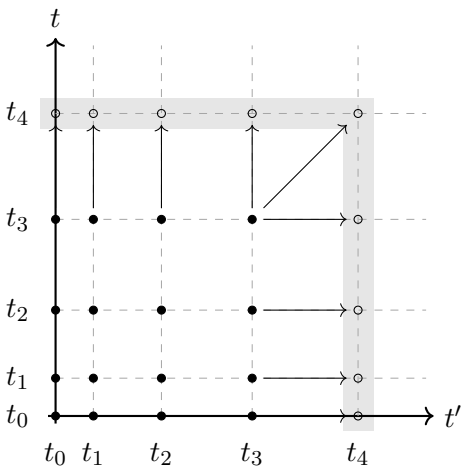

Figure 3.1: Time-stepping procedure for (1.67).

where

$$\begin{aligned} \mathbf{g}^v(t_i) &= \big[g(t_i,t_0), g(t_i,t_1), \ldots, g(t_i,t_i)\big] \ , \\ \mathbf{g}^h(t_i) &= \big[g(t_0,t_i), g(t_1,t_i), \ldots, g(t_i,t_i)\big] \ , \\ \mathbf{g}^d(t_i) &= \big[g(t_i,t_i)\big] \ , \end{aligned} \tag{3.4}$$

and $\circ$ denotes the element-wise Volterra integration

$$(\mathbf{A}\circ\mathbf{B})^v(t_i) = \left[\int_{\gamma'} \mathrm{d}\bar{t}\, A(t_i,\bar{t})B(\bar{t},t_0), \int_{\gamma'} \mathrm{d}\bar{t}\, A(t_i,\bar{t})B(\bar{t},t_1), \ldots, \int_{\gamma'} \mathrm{d}\bar{t}\, A(t_i,\bar{t})B(\bar{t},t_i)\right] \ , \tag{3.5}$$

with analogous definitions for the h and d components.

Kadanoff-Baym equations are set apart from univariate ordinary differential equations (ODEs) or VIDEs by the fact that their dimension grows with each time-step — the size of $\mathbf{g}^v(t)$ and $\mathbf{g}^d(t)$ grows by one when stepping from t_i to t_{i+1}. This requires a continued resizing of the equations and is one reason why such equations are not straightforwardly compatible with the extensive amount of available ODE solvers. Moreover, unlike population-growth problems, for example, where the size of the equations may also grow with time, the new equations that are added when solving Kadanoff-Baym equations have a *past*. This can be visualised via Figure 3.1 by noting that, for example, when stepping vertically or horizontally from $g(t_4,t_4)$, the right-hand side of the differential equations for the new elements in $\mathbf{g}^v(t)|_{t=t_4}$ and $\mathbf{g}^h(t)|_{t=t_4}$ involve in general non-zero terms at times $t < t_4$. For multi-step methods, in particular, this may necessitate additional care (cf. Section 3.3).

Viewing the Kadanoff-Baym integration procedure effectively as a one-time ODE problem has two main benefits: First, it opens up the possibility of applying virtually any general linear method to solve Kadanoff-Baym equations. And second, additional one-time functions such as mean fields (first cumulants) can be solved simultaneously and in a unified manner, allowing direct method implementations with well-defined local error estimations.

3.2 Univariate Volterra Integrodifferential Equations

Following the structure presented in (3.3), consider a univariate non-linear VIDE in standard form, i.e.

$$y'(t) = F[t, y(t)] + \int_{t_0}^{t} \mathrm{d}s\, K[t, s, y(s)] \ , \tag{3.6}$$

which can also be seen as a system of two equations, of which one is an ordinary differential equation and the other a Volterra integral equation,

$$\begin{aligned} y'(t) &= F[t, y(t)] + z(t) \ , \\ z(t) &= \int_{t_0}^{t} \mathrm{d}s\, K[t, s, y(s)] \ , \end{aligned} \tag{3.7}$$

subject to the initial condition

$$y(t_0) = y_0 \ . \tag{3.8}$$

In some cases, it is possible to solve such equations with analytic methods [72], yet this usually requires the integral kernel to have specific properties such as linearity $K\left[t, s, y(s)\right] = K(t, s)y(s)$, which is not the case for most physical systems of interest. Hence, one must resort to discrete methods.

While there are many methods one can employ to solve ODEs, *a priori*, there is no best method. Its choice strongly depends on factors such as stiffness, desired accuracy and function evaluation cost. A variable order and variable step size Adams (predictor-corrector) method provides a good trade-off between cost (two function evaluations per step) and overall accuracy, even when the number of equations is very large, as is indeed the case with Kadanoff-Baym equations, where the number of equations roughly equals the dimension of $G(t_0, t_0)$ times the number of time-steps.

In methods based on integration, (3.7) is integrated from t_n to t_{n+1}

$$y(t_{n+1}) = y(t_n) + \int_{t_n}^{t_{n+1}} \mathrm{d}s\, \left\{F[s, y(s)] + z(s)\right\} \ , \tag{3.9}$$

and the integrals are then evaluated with interpolating quadrature formulas. Here it becomes clear that the main computational bottleneck in solving these equations is in the computation of $z(t)$, which can be evaluated with a so-called direct quadrature method

$$z(t_n) = \int_{t_0}^{t} \mathrm{d}s\, K\left[t_n, s, y(s)\right] = \sum_{\ell=0}^{n-1} \int_{t_\ell}^{t_{\ell+1}} \mathrm{d}s\, K\left[t_n, s, y(s)\right] \ . \tag{3.10}$$

Nonetheless, it is possible to differentiate $z(t)$ further and treat $\left\{y'(t), z'(t)\right\}$ as a system of coupled differential equations [74], which would be more suitable in cases where the integral equation is stiff ($-\partial K/\partial y \gg 1$) [75]. It was opted for the former due to its more straightforward implementation and because most physical systems of interest do not satisfy such stiffness criterion.

3.3 Variable Adams method

The variable Adams method [76] is a predictor-corrector scheme where the integrand of (3.9) is approximated by a Newton polynomial, that is, an interpolation polynomial for previously computed points. A prediction y^*_{n+1} for the solution of $y(t_{n+1})$ (note that here * denotes the

prediction, not complex conjugation) is obtained via an explicit method with a $(k-1)$-th order polynomial

$$y_{n+1}^{*} = y_n + \int_{t_n}^{t_{n+1}} \mathrm{d}s \sum_{j=0}^{k-1} \left[\prod_{i=0}^{j-1} (s - t_{n-i}) \right] \delta^j \left\{ F\left[t_n, y(t_n)\right] + z(t_n) \right\} \ , \tag{3.11}$$

and the divided differences are defined recursively as

$$\begin{aligned} \delta^0 F\left[t_\ell, y(t_\ell)\right] &= F\left[t_\ell, y(t_\ell)\right] \ , \\ \delta^j F\left[t_\ell, y(t_\ell)\right] &= \frac{\delta^{j-1} F\left[t_\ell, y(t_\ell)\right] - \delta^{j-1} F\left[t_{\ell-1}, y(t_{\ell-1})\right]}{t_\ell - t_{\ell-j}} \ . \end{aligned} \tag{3.12}$$

The prediction for $y(t_{n+1})$ is now corrected via an implicit method, where the k-th order interpolation polynomial of the integrand depends on the predicted value y_{n+1}^{*}:

$$y_{n+1} = y_{n+1}^{*} + \int_{t_n}^{t_{n+1}} \mathrm{d}s \left[\prod_{i=0}^{k-1} (s - t_{n-i}) \right] \delta^k \left\{ F[t_{n+1}, y(t_{n+1})] + z(t_{n+1}) \right\} \ . \tag{3.13}$$

The integrals in (3.10) can be evaluated in the same predictor-corrector manner:

$$\begin{aligned} z_n^{*} &= \sum_{\ell=0}^{n-1} \int_{t_\ell}^{t_{\ell+1}} \mathrm{d}s \sum_{j=0}^{k-1} \left[\prod_{i=0}^{j-1} (s - t_{\ell-i}) \right] \delta^j K_n\left[t_\ell, y(t_\ell)\right] \ , \\ z_n &= z_n^{*} + \sum_{\ell=0}^{n-1} \int_{t_\ell}^{t_{\ell+1}} \mathrm{d}s \left[\prod_{i=0}^{k-1} (s - t_{\ell-i}) \right] \delta^k K_n\left[t_{\ell+1}, y(t_{\ell+1})\right] \ , \end{aligned} \tag{3.14}$$

with divided differences defined as

$$\begin{aligned} \delta^0 K_n\left[t_\ell, y(t_\ell)\right] &= K\left[t_n, t_\ell, y(t_\ell)\right] \ , \\ \delta^j K_n\left[t_\ell, y(t_\ell)\right] &= \frac{\delta^{j-1} K_n\left[t_\ell, y(t_\ell)\right] - \delta^{j-1} K_n\left[t_{\ell-1}, y(t_{\ell-1})\right]}{t_\ell - t_{\ell-j}} \ . \end{aligned} \tag{3.15}$$

The main difficulties when evaluating the predictor-corrector equations (3.11) and (3.13) are that it is challenging to obtain a closed formula for the integrals and that it is algorithmically expensive to calculate the divided differences via recursive formulas (3.12). While for equidistant time grids, the equations find a simple and compact form [76], in the non-equidistant case, the expressions rapidly become convoluted and complicated to implement. These problems can be circumvented by recurrence formulas [76], making the evaluation of the integrals and j-th derivatives more efficient.

In between time steps, an estimate of the local truncation error can be obtained by computing $\tilde{y}_{n+1} - y_{n+1}$, where $\tilde{y}_{n+1}$ is the result of the implicit step using a $(k+1)$-th order formula. It is assumed that as $k \to \infty$, the error approaches zero (in which case the integral quadrature formula is said to be *convergent*). A measure of this error satisfying specific tolerances is obtained via

$$le_k(n+1) := \frac{\tilde{y}_{n+1} - y_{n+1}}{\texttt{atol} + \texttt{rtol} \cdot \max\left(|y_n|, |y_{n+1}|\right)} \ , \tag{3.16}$$

for which the integration step is accepted if

$$\left\| le_k(n+1) \right\|_p \leq 1 \ , \tag{3.17}$$

and the norm is defined as

$$\|x\|_p = \left(\frac{1}{n} \sum_i^n \left| x^i \right|^p \right)^{\frac{1}{p}} , \tag{3.18}$$

where typically $p = 2$. Given this acceptance criterion, the roles of the tolerances `rtol` and `atol` in (3.16) can be better understood considering them separately under the infinity-norm. In this scenario, $-\log_{10}$ `rtol` controls the minimum number of correct digits between time steps, while `atol` is a threshold for the magnitude of the elements of y for which the minimum number of correct digits is guaranteed. This local error is then used to adjust both the step size $h_n \coloneqq (t_{n+1} - t_n)$ and the order k. The next time step is chosen as the largest possible step that still satisfies the local error being $\lesssim 1$. Given the current local error $\left\| le_k(n+1) \right\| \simeq C h_n^{k+1}$ for some constant C, and assuming that the subsequent error is maximal, i.e. $\left\| le_k(n+2) \right\| \simeq C h_{n+1}^{k+1} \approx 1$, the next time-step can be chosen optimally as [76]

$$h_{n+1} = h_n \left\| le_k(n+1) \right\|_p^{-\frac{1}{k+1}} . \tag{3.19}$$

Obtaining the optimal order k is slightly more involved, and the reader is referred to [76] for an excellent and self-contained explanation of heuristic mechanisms for order selection. However, regardless of the order k, the number of required function evaluations per time step is constant. Hence k is ideally set to a large value ($\gtrsim 5$) such that the integrator can take larger steps and the overall computational cost is reduced.

3.4 Volterra Integral Equations of the Second Kind

More elaborate self-energy approximations (GW, T-matrix [77], $1/\mathcal{N}$ [24]), which comprise resummations of particular classes of diagrams, require the solution of Volterra integral equations of the second kind [78]:

$$I(t,t') = \Phi(t,t') - \int_{\mathcal{C}} \mathrm{d}\bar{t}\, \Phi(t,\bar{t}) I(\bar{t},t') . \tag{3.20}$$

In the mentioned self-energy approximations, the kernel $K(t,t')$ of (3.1) then typically depends linearly on $I(t,t')$ and $\Phi(t,t')$ is a function of $g(t,t')$.

There are several ways of solving (3.20): by inversion of the triangular system of equations obtained when discretising in the same manner as in (3.3), by reduction to a VIDE through differentiation, or by iteration of the equation [79]. Since (3.20) has to be solved simultaneously with (3.1), reducing it to a VIDE would be ideal, yet this generally results in stiff equations [74] for which the variable Adams method (Section 3.3) is not appropriate. Therefore, to achieve congruity with the method previously presented, (3.20) is solved iteratively at every predictor and corrector step, i.e. following the same evolution procedure as depicted in Figure 3.1.

3.5 Leveraging Symmetries and Physical Properties

Leveraging symmetries and other physical properties of a system can significantly reduce the computational effort on top of what can be achieved by adaptive time-stepping.

3.5.1 Symmetries in the Two-Time Domain

Apart from the symmetries of the Hamiltonian, the two-time Green functions encountered in quantum and classical systems possess symmetries in the two-time domain (t,t'). For example,

in the quantum case, the numerical implementations are based on the greater and lesser Green functions that are skew-Hermitian in time,

$$\left[\boldsymbol{G}^{\lessgtr}(t,t')\right]^{\dagger} = -\boldsymbol{G}^{\lessgtr}(t',t) \ . \tag{3.21}$$

Hence, the solutions are entirely determined by either the upper- or lower-triangular elements, which essentially cuts in half the number of equations by requiring only the integration of $\mathbf{G}^d$ and either $\mathbf{G}^v$ or $\mathbf{G}^h$. However, similar relations hold for classical systems with different symmetry relations [32].

3.5.2 Memory truncation

The clustering decomposition principle [80] ensures that at a large-enough time separation of the physical operators, any n-point function factorises. In terms of *connected* 2-point functions, this has the signature of exponential or power-law *decay* in the relative-time direction (Section 1.3.2) for massive and massless fields, respectively [81]. This principle should hold for any stable, long-lived state, an example being thermalised systems [82] described by a Gibbs ensemble. This effect is likewise present in physical systems connected to some kind of reservoir (e.g. as in open quantum systems [69], or quantum impurity systems described by dynamical mean-field theory [83]). The VIDE can hence often be approximated by a Volterra *delay*-integrodifferential equation with

$$z(t) = \int_{t-\tau_{\text{cutoff}}}^{t} \mathrm{d}s\, K\left[t,s,y(s)\right] \ , \tag{3.22}$$

where τ_{cutoff} is some cut-off time. This is rooted in the fact that the physical Green functions in such systems display long-time decay and, thus

$$\left\| \int_{t-\tau_{\text{cutoff}}}^{t} \mathrm{d}s\, K\left[t,s,y(s)\right] \right\| \gg \left\| \int_{t_0}^{t-\tau_{\text{cutoff}}} \mathrm{d}s\, K\left[t,s,y(s)\right] \right\| \ . \tag{3.23}$$

Since one bottleneck when solving Kadanoff-Baym equations is in the evaluation of the integrals, introducing a cutoff time can dramatically reduce the computational complexity from $\mathcal{O}\left(n^2 k(n)\right)$ to $\mathcal{O}\left(n^2 k(N_{\tau_{\text{cutoff}}})\right)$ where n denotes the number of time-steps, $N_{\tau_{\text{cutoff}}}$ the number of time points in the interval $[t-\tau_{\text{cutoff}}, t]$ and k is the complexity of integrating the kernel as a function of the number of required time points. Moreover, these grid points can then also be excluded from future time evolution, which further reduces the overall complexity to $\mathcal{O}\left(nN_{\tau_{\text{cutoff}}} k(N_{\tau_{\text{cutoff}}})\right)$. This point and its relation to the generalised Kadanoff-Baym ansatz [84] are taken up again in our discussion of the Fermi-Hubbard model in [32].

The algorithm's sensitivity to values off the two-time diagonal can be explicitly adjusted via the parameter `atol`, irrespective of the nature of the decay of the Green functions away from the diagonal. For rapid (exponential) decay, e.g. in a driven system, a given value of this parameter will lead to a small number of grid points. The same tolerances for slow (algebraic) decay will result in more grid points.

Part II

Optically Driven, Non-Equilibrium Heavy-Fermion Systems

Chapter 4

Heavy-fermion systems driven by a terahertz light pulse

Heavy-fermion compounds boast an intricate phase diagram (Figure 4.1) due to the interplay of magnetic- and electric-ordering quantum fluctuations arising from a high concentration of localised valence electrons interacting with mobile conduction electrons. For example, in the heavy-fermion compound $CeCu_{6-x}Au_x$, there is a competition controlled by chemical doping between a heavy Fermi liquid and an anti-ferromagnetic phase, with a quantum critical point at $x = 0.1$ doping fraction [6]. The $CeCu_6$ compound is in a heavy Fermi liquid phase, and doping with Au atoms distorts the lattice and induces a reduction of the exchange coupling strength between the f and conduction electrons responsible for the Kondo effect, which tends to *locally* screen of the spin of valence f-electrons and is behind the heavy Fermi liquid phase (Section 4.1.1). The lattice distortion favours the *long-range* Ruderman–Kittel–Kasuya–Yosida (RKKY) interaction between neighbouring f-electrons, which tends to align anti-ferromagnetically the valence electrons in the lattice. Because of these quantum phases' inherent complexity and antagonist character, there is still an ongoing debate about the system's quasiparticles near or at the quantum critical point, where the phases can co-exist.

In the work [12], $CeCu_{6-x}Au_x$ was irradiated by an ultrafast[1] pulse of terahertz (THz) radiation. THz time-domain spectroscopy is one of the few experimental techniques that can temporally resolve the ultrafast dynamics of materials, which can be used to inspect and characterise their low-energy excitations. Unlike photo-emission experiments, which use intense ultraviolet radiation to eject photo-excited electrons, ultrafast THz spectroscopy only slightly stirs up the electrons with non-ionising radiation and evades the pitfalls of the former such as lattice distortion and heating, which would heavily disturb the delicate low-energy physics of these compounds. A pulse of linearly polarised THz light with a frequency range of 0.1–3 THz photoexcites a $CeCu_{6-x}Au_x$ sample, which initiates a dynamical response. Due to the penetration depth of THz fields in conductive mediums being only a few nanometers long, the reflected (instead of the transmitted) electric field is measured. For the anti-ferromagnetic compound $CeCu_5Au_1$, as well as for a test Pt mirror [85], only an instantaneous reflection of the pulse is observed (Figure 4.2). Such immediate response is, however, expected for any metallic compound and is simply the reflectivity caused by conduction electrons. However, for the heavy Fermi liquid $CeCu_6$, and the quantum critical $CeCu_{5.9}Au_{0.1}$ compounds, a delayed reflected pulse – or echo – appears (Figure 4.2).

[1]The ultrafast timescales are between the femtosecond (10^{-15} s) and the nanosecond (10^{-9} s), with one picosecond (10^{-12} s) being to one second as one second is to approximately 32000 years.

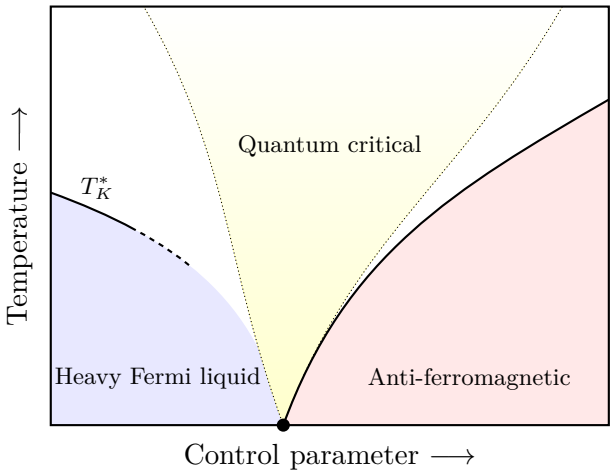

Figure 4.1: Phase diagram of heavy-fermion systems.

The delayed pulse does not show an exponential decay, as expected for weakly interacting or single-particle relaxation. Instead, it is a compact pulse, with a pronounced "dark time" of $\tau_{\text{echo}} \approx 6.2$ ps in $CeCu_6$ and $\tau_{\text{echo}} \approx 5.8$ ps in $CeCu_{5.9}Au_{0.1}$ after the instantaneous reflection. Furthermore, coherence time in metals is typically within femtosecond timescales [86], which hints at the relation of the echo with low-energy excitations with longer characteristic timescales. Namely, the delay time agrees[2] with the reported [10] compound's Kondo lattice-coherence temperature $\tau_{\text{echo}} \sim \frac{h}{k_B T_K^*} \approx 8$ ps, where h is the Planck's constant and k_B the Boltzmann constant, and is also strongly temperature dependent, vanishing at high temperatures, also in remarkable agreement with Kondo physics. Hence, a direct link was established between the origin of the echo and the Kondo quasiparticles characteristic of the heavy Fermi liquid phase of the heavy-fermion compound. The generation of the echo pulse was qualitatively described via a rate equation [12] which proposed it to be a response from the reconstruction of the Kondo lattice coherence after its destruction by the incident pulse. The THz radiation induces dipole interband transitions between the heavy $4f$ and the light $5d$ bands, which break the Kondo singlets. Due to an occupation-dependent transition rate specific to heavy Fermi liquid systems, the electrons' recombination can only occur after enough time has passed for the build-up of the Kondo lattice coherence, leading to a delayed response.

The importance of this class of experiments lies in directly addressing questions such as whether T_K^* vanishes or remains finite at the quantum critical point of $CeCu_{6-x}Au_x$ [6] and hence whether heavy quasiparticles survive or not criticality.

4.1 The Anderson lattice model

Ce compounds such as $CeCu_6$ are characterised by having valence electrons in the $4f$ shell of Ce. The seven orbitals of the $4f$ shell – each doubly degenerate due to the electrons' spin – are split in energy by spin-orbit coupling and crystal field effects and, when embedded in a lattice, create narrow valence bands due to the spatial confinement of the orbitals, with only a few

[2] The finite lifetime of Kondo quasiparticles can be related to the width of their excitation spectrum $k_B T_K$ (Section 4.1.1) via the time-energy uncertainty relation [87]. Its nature is very different from Heisenberg's uncertainty relations due to time not being an operator. However, despite its correctness being somewhat disputed, it is of great heuristic value. In this case, the uncertainty in the energy of Kondo quasiparticles leads to an uncertainty in the lifetime of its quasiparticles, related to the time for photon emission.

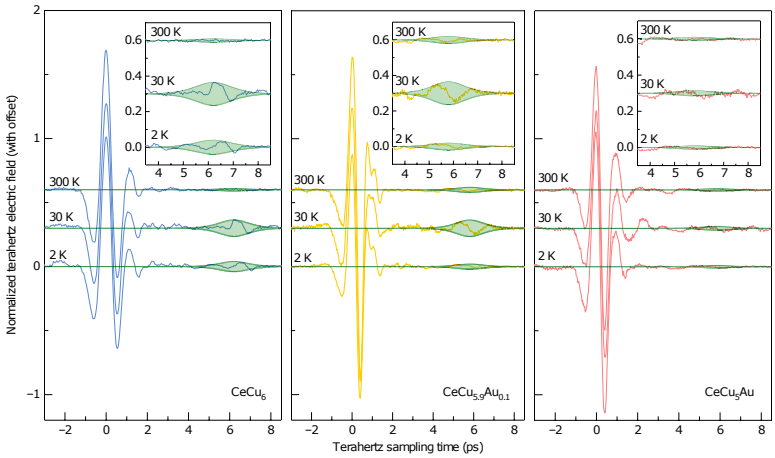

Figure 4.2: Time-resolved reflectivity of $CeCu_{6-x}Au_x$, colour matched with the phases of Figure 4.1. The instantaneous reflection occurs at sampling time 0, and the time-delayed reflected pulse is highlighted in the insets. Reproduced from [12], with permission.

bands left at the vicinity of the Fermi level in $CeCu_6$. In accordance with the valence of Ce in $CeCu_6$ [13], the $4f$ shell is considered to contain just one valence electron and, due to strong Coulomb repulsion – weakly screened on atomic length scales – only the lowest-lying doublet (Figure 4.3) is significantly occupied, with the physics stemming from considering the other doublets deemed unimportant at low temperatures.

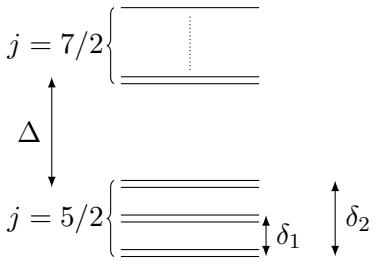

Figure 4.3: Schematic of f-orbital splitting in $CeCu_6$ [88]. Spin-orbit coupling splits the $4f$ orbitals of Ce in $j = 5/2$ and $j = 7/2$ multiplets, separated by $\Delta \approx 250$ meV [89]. Crystal field effects further split the $j = 5/2$ multiplet into three doublets separated by $\delta_1 = 7$ meV and $\delta_2 = 15$ meV.

The Coulomb interaction strength U in f-valence compounds is the largest energy scale, typically comparable with the conduction bandwidth [90]. As a result, the empty f^0 and singly-occupied f^1 state of the doublet are close in energy and much lower than the doubly-occupied f^2, which can be *projected out* in low-energy models. However, this is not universal, and for systems with larger energy separations between the f^0 and f^1 configuration, a $U \to \infty$ limit may not even be suitable for qualitative studies. Although initially introduced to describe the effects of a low concentration of magnetic impurities in metals, it is believed that the $U \to \infty$ limit of the Anderson lattice model [91] captures the essential low-energy physics of heavy-fermion compounds [92]

$$\hat{H}_{\mathrm{ALM}} = -\sum_{\langle i,j\rangle\sigma} t^c_{ij}\hat{c}^\dagger_{i\sigma}\hat{c}_{j\sigma} - \sum_{\langle i,j\rangle\sigma} t^f_{ij}\,|\sigma\rangle^f_i\,\langle\sigma|^f_j + \sum_{i\sigma}\varepsilon^f_0\,|\sigma\rangle^f_i\,\langle\sigma|^f_i + V_0\sum_{i\sigma}\left(\hat{c}^\dagger_{i\sigma}\,|0\rangle^f_i\,\langle\sigma|^f_i + \mathrm{h.c.}\right) . \tag{4.1}$$

This model describes the hybridisation of a band of non-interacting conduction electrons c (related to the extended s, p or d orbitals of the compound) with localised interacting electrons f. The f electrons are considered *localised* due $\varepsilon_0^f < 0$ and the spatial confinement of the f orbitals, resulting in a hopping strength $|t^f| \ll |t^c|$. The Anderson lattice model parameters of $CeCu_6$ were estimated [88] to be $\varepsilon_0^f = -1.61$ eV, $V_0 = 0.41$ eV and $U \sim 5$ eV, similar to the conduction bandwidth, which supports the doubly-occupied f-states to be projected out of the theory. The states $|0\rangle_i^f$ and $|\sigma\rangle_i^f$ represent, respectively, the empty f^0 and singly occupied f^1 configurations of an f-electron with spin σ on site the i.

The Hamiltonian is equivalently described in terms of creation/annihilation operators $\hat{f}$ acting on a *restricted* Hilbert space, subject to the operator constraint

$$\sum_\sigma \hat{f}_{i\sigma}^\dagger \hat{f}_{i\sigma} \leq 1 \ . \tag{4.2}$$

This inequality, challenging to implement due to the c-f hybridisation, can be turned into an equality by the addition of a new auxiliary particle (Chapter 2), a boson field b, with the projection operators of the Hamiltonian mapped to

$$|0\rangle_i^f \langle\sigma|_i^f \to \hat{b}_i^\dagger \hat{f}_{\sigma i} \ , \qquad |\sigma\rangle_i^f \langle\sigma|_i^f \to \hat{f}_{i\sigma}^\dagger \hat{f}_{i\sigma} \ . \tag{4.3}$$

Due to projection operators, the strong Coulomb repulsion character was built-in from the beginning, and thanks to the auxiliary-particle mapping, all particle operators satisfy canonical commutation relations and the hybridisation is promoted to a proper interaction, amenable to perturbative methods. The resulting Hamiltonian reads

$$H_{\text{ALM}} = -\sum_{\langle i,j\rangle\sigma} t_{ij}^c \hat{c}_{i\sigma}^\dagger \hat{c}_{j\sigma} - \sum_{\langle i,j\rangle\sigma} t_{ij}^f \hat{f}_{i\sigma}^\dagger \hat{b}_i \hat{b}_j^\dagger \hat{f}_{j\sigma} + \sum_{i\sigma} \varepsilon_0^f \hat{f}_{i\sigma}^\dagger \hat{f}_{i\sigma} + V_0 \sum_{i\sigma} \left(\hat{c}_{i\sigma}^\dagger \hat{b}_i^\dagger \hat{f}_{i\sigma} + \text{h. c.} \right) \ , \tag{4.4}$$

where the operator constraint

$$\hat{Q}_i = \hat{b}_i^\dagger \hat{b}_i + \sum_\sigma \hat{f}_{i\sigma}^\dagger \hat{f}_{i\sigma} = \hat{\mathbb{1}} \ , \tag{4.5}$$

must be enforced at all lattice sites i.

4.1.1 Phenomenology of Anderson-impurity models

For a *single*-impurity Anderson model, where there is just one f shell (denoted as the "impurity") in a sea of conduction c electrons, the model is characterised by the Kondo $|\varepsilon_0^f| \gg \Delta$ and the mixed-valence $\Delta \gtrsim |\varepsilon_0^f|$ regimes. In both regimes, the physics is dominated by the Coulomb repulsion, whose strength U is much larger than the hybridisation strength $W_0 = V_0^2 \rho_0^c(\varepsilon_F)$, where $\rho_0^c(\varepsilon_F)$ is the bare density of states of c-electrons at the Fermi energy. But while in the former, the f-shell average occupation is one, in the latter, the proximity of the f-shell bare energy to the Fermi energy leads to a mixed-valence regime, with an average occupation of less than one (i.e., possible loss of the "local moment").

The Kondo effect

Focusing on the Kondo regime, the strong Coulomb repulsion favours the f shell to be occupied by either a spin-up or spin-down electron, and a *sequential* tunnelling process between c and f electrons is energetically preferred. The Kondo temperature T_K

$$T_K = D \left(\frac{NW_0}{D} \right)^{1/N} \exp\left(\frac{\varepsilon_0^f}{NW_0} \right) \ , \tag{4.6}$$

where D is the half-bandwidth of c electrons and N is the degeneracy of the local moment [93], sets the energy scale for which the tunneling becomes *resonant*. As the temperature is lowered $T \lesssim T_K$, scattered electrons scatter again coherently with the impurity and become *correlated*. Quantum mechanically, an electron can hop out of the impurity, within a short timescale $\hbar/|\varepsilon_0^f|$ (Footnote 2) into the surface of the Fermi sphere, which populates the impurity level with another electron, possibly with a different spin [1]. The sequential spin-flip scattering between impurity electrons and excitations in the Fermi sea gives rise to a *many-body* resonance, which exhibits a sharp peak of width $\sim k_\mathrm{B}T_K$ in the impurity electrons' spectral function at the Fermi energy. The resonance is known as the Abrikosov-Suhl or Kondo resonance and is the smoking gun of the Kondo effect. At high temperatures, $k_\mathrm{B}T \gg U$, decoherence through thermal fluctuations washes out many-body coherent effects, and the physics is dominated by single-particle dynamics.

In a lattice of f and c- electrons, resonant scattering at each lattice site will generate a Kondo lattice-coherent resonance with width[3] $\sim k_\mathrm{B}T_K^*$ at the Fermi energy of the on-site spectral function of each f-electron. As these are embedded in a lattice, a coherent f-band is formed, with significant spectral density at the Fermi energy because of the resonance. This increases the number of mobile electrons in the system, and due to the local character of f-electrons, the band is mostly flat, resulting in a large effective mass of the charge carriers at low temperatures. These *heavy* itinerant electrons lead to an observable expansion of the Fermi volume, as the Fermi surface must expand to accommodate the additional number of indistinguishable electrons in the Fermi sea. This is, however, not general, as reported in [95]. Despite the RKKY interaction not being addressed in this thesis, the relation of its energy scale $E_\mathrm{RKKY} \sim J_K^2\rho_0^c(\varepsilon_F)$ [94] with the Kondo temperature can roughly estimate the phase of the heavy-fermion compound. For $k_\mathrm{B}T_K^* \gg E_\mathrm{RKKY}$ the system is in a heavy Fermi liquid phase and decreasing the exchange coupling $J_K \sim -2V^2\frac{U}{(U+\varepsilon_0^f)\varepsilon_0^f}$ [96] between c and f electrons can lead to $E_\mathrm{RKKY} \gg k_\mathrm{B}T_K^*$ and hence an anti-ferromagnetic phase.

4.2 Light-matter interaction

The literature has typically treated light-matter interactions in non-equilibrium many-body systems via the Peierls substitution, which dresses the electronic hopping matrix elements t_{ij} as

$$t_{ij} \to t_{ij} e^{i\int_{\boldsymbol{R}_i}^{\boldsymbol{R}_j} \mathrm{d}\boldsymbol{x}\cdot\boldsymbol{A}(\boldsymbol{x})} \,, \tag{4.7}$$

where $\boldsymbol{A}$ is the electromagnetic (EM) vector potential. Although a compact and elegant formulation – and even finding some uses in strong light-matter coupling scenarios, this formulation has some limitations. First, the light-matter coupling strength is fixed by the strength of the field and does not depend on material properties [97]. Second, it only couples light to non-local hopping elements and neglects local hoppings, such as light-induced orbital transitions. Moreover, $\boldsymbol{A}$ is typically considered a classical field, resulting in a semi-classical theory of light-matter interactions. Even though such semi-classical approximations can be appropriate for the study of some non-linear optics or laser theory [98], a *quantum* theory of light is required for classes of problem dealing with spontaneous/stimulated emission or coherent emission, such as super-radiance – with similar quantum effects expected from the interaction of an external pulse of THz radiation.

[3] Unlike the single-impurity Kondo temperature $k_\mathrm{B}T_K$, which is understood as the energy at which perturbative renormalisation group breaks down [94], there is not an agreed formula for the Kondo (lattice-)coherence temperature T_K^*.

4.2.1 Quantisation of the electromagnetic field

The canonical *quantisation* of a classical theory promotes the classical Poisson brackets, related to the canonical variables, to a commutator[4]. Regrettably, the condensed-matter literature awkwardly overlooks many important theoretical details of this procedure when quantising the EM field, such as the emergence of the Coulomb interaction from coupling the EM field to matter currents. The actual quantisation is also typically framed as an inexplicable replacement of scalar coefficients by quantum operators. Running the risk of falling down the rabbit hole on a by-now textbook problem, refer to [99] for a complete and rigorous quantisation of the EM field.

In a free region of space[5], i.e., in the absence of current densities, the EM vector potential $\boldsymbol{A}$ in the Coulomb gauge $\boldsymbol{\nabla}\cdot\boldsymbol{A}(\boldsymbol{x},t)=0$ is described by the wave-equation

$$-\nabla^2\boldsymbol{A}(\boldsymbol{x},t)+\frac{1}{c^2}\frac{\partial^2}{\partial t^2}\boldsymbol{A}(\boldsymbol{x},t)=\boldsymbol{0}\ , \tag{4.8}$$

with the total energy of the system given by

$$H_{\text{em}}=\frac{1}{2}\int \mathrm{d}\boldsymbol{x}\ \left(\varepsilon_0\boldsymbol{E}(\boldsymbol{x},t)^2+\frac{1}{\mu_0}\boldsymbol{B}(\boldsymbol{x},t)^2\right)\ , \tag{4.9}$$

where $\boldsymbol{E}(\boldsymbol{x},t)=-\frac{\partial}{\partial t}\boldsymbol{A}(\boldsymbol{x},t)$ and $\boldsymbol{B}(\boldsymbol{x},t)=\boldsymbol{\nabla}\times\boldsymbol{A}(\boldsymbol{x},t)$. Considering the field to be contained in a finite volume V and imposing periodic boundary conditions, the EM field can be *box quantised* [101]. The vector potential is expanded as a sum of the discrete modes and separated into two complex terms

$$\boldsymbol{A}(\boldsymbol{x},t)=\sum_{\boldsymbol{k}s}\boldsymbol{e}_{\boldsymbol{k}s}A_{\boldsymbol{k}s}(\boldsymbol{x},t)=\sum_{\boldsymbol{k}s}\boldsymbol{e}_{\boldsymbol{k}s}\left[A_{\boldsymbol{k}s}(t)\frac{e^{i\boldsymbol{k}\cdot\boldsymbol{x}}}{\sqrt{V}}+\text{h. c.}\right]\ , \tag{4.10}$$

where s denotes the polarisation and $\boldsymbol{e}_{\boldsymbol{k}s}$ are unit polarisation vectors which satisfy the orthogonality condition $\boldsymbol{e}_{\boldsymbol{k}s}\cdot\boldsymbol{e}_{\boldsymbol{k}s'}=\delta_{ss'}$ and the Coulomb gauge condition $\boldsymbol{k}\cdot\boldsymbol{e}_{\boldsymbol{k}s}=0$ in reciprocal space. Re-scaling the variable $A_{\boldsymbol{k}s}(t)=\sqrt{\frac{\hbar\omega_{\boldsymbol{k}}}{2\varepsilon_0}}a_{\boldsymbol{k}s}(t)$, the solution of (4.8)

$$\left(\tfrac{\partial^2}{\partial t^2}+\omega_{\boldsymbol{k}}^2\right)a_{\boldsymbol{k}s}(t)=0\ , \tag{4.11}$$

with $\omega_{\boldsymbol{k}}=c|\boldsymbol{k}|$, results [101] in an expression for the EM vector potential

$$\boldsymbol{A}(\boldsymbol{x},t)=\sum_{\boldsymbol{k}s}\sqrt{\frac{\hbar}{2\omega_{\boldsymbol{k}}\varepsilon_0 V}}\left[e^{i(\boldsymbol{k}\cdot\boldsymbol{x}-\omega_{\boldsymbol{k}}t)}\boldsymbol{e}_{\boldsymbol{k}s}a_{\boldsymbol{k}s}+\text{h. c.}\right]\coloneqq\sum_{\boldsymbol{k}s}\left[\tilde{\boldsymbol{A}}_{\boldsymbol{k}s}(\boldsymbol{x},t)a_{\boldsymbol{k}s}+\text{h. c.}\right]\ , \tag{4.12}$$

identical to a collection of quantised simple harmonic oscillators. The total energy (4.9) then reads

$$H_{\text{em}}=\sum_{\boldsymbol{k}s}\frac{\hbar\omega_{\boldsymbol{k}}}{2}\left(a_{\boldsymbol{k}s}^*a_{\boldsymbol{k}s}+a_{\boldsymbol{k}s}a_{\boldsymbol{k}s}^*\right)\ , \tag{4.13}$$

[4] In Maxwell's theory, the canonical variable is the vector potential $\boldsymbol{A}$ and its conjugate variable is the transverse electric field $E^{\perp}\coloneqq-\frac{\partial\boldsymbol{A}}{\partial t}$. Such relations closely resemble the momentum being the time-derivative of the position (up to a constant) of classical mechanics.

[5] Note $\boldsymbol{A}$ is given by the sum of the external $\boldsymbol{A}_{\text{ext}}$ and the internal $\boldsymbol{A}_{\text{int}}$ vector potential which is self-consistently generated by matter being composed of charged moving particles. It has been shown [100] that neglecting $\boldsymbol{A}_{\text{int}}$ can be inaccurate in metals, namely for light frequencies of $\boldsymbol{A}_{\text{ext}}$ typically in the *mid* to *near*-infrared region (roughly 30-300 THz). However, given the light-matter coupling of interest being in the *far*-infrared region – i.e., roughly two orders of magnitude lower in frequency, only $\boldsymbol{A}=\boldsymbol{A}_{\text{ext}}$ will be considered.

which is mathematically equivalent to the energy of a set of harmonic oscillators with frequency $\omega_{\boldsymbol{k}}$. Given the formal equivalence to oscillators, the quantisation of the EM field can heuristically be accomplished by promoting $a^*_{\boldsymbol{k}s}$ and $a_{\boldsymbol{k}}$ to mutually adjoint operators satisfying bosonic commutation relations

$$[\hat{a}_{\boldsymbol{k}s}, \hat{a}_{\boldsymbol{k}'s'}] = \left[\hat{a}^\dagger_{\boldsymbol{k}s}, \hat{a}^\dagger_{\boldsymbol{k}'s'}\right] = 0 \ , \qquad \left[\hat{a}_{\boldsymbol{k}s}, \hat{a}^\dagger_{\boldsymbol{k}'s'}\right] = \delta_{\boldsymbol{k}\boldsymbol{k}'}\delta_{ss'} \ . \tag{4.14}$$

These are the creation and annihilation operators of photons, the quanta (or excited states) of the quantised EM field, with total energy

$$\hat{H}_{\text{em}} = \sum_{\boldsymbol{k}s} \hbar\omega_{\boldsymbol{k}} \left(\hat{a}^\dagger_{\boldsymbol{k}s}\hat{a}_{\boldsymbol{k}s} + \frac{1}{2}\right) \ . \tag{4.15}$$

4.2.2 Anderson lattice model coupled to terahertz light

Light-matter coupling (dipole gauge)

The interaction between the EM and matter fields can be introduced via the *minimal coupling*, where the transformation of the momentum operator

$$-i\hbar\boldsymbol{\nabla} \to -i\hbar\boldsymbol{\nabla} + e\boldsymbol{A} \tag{4.16}$$

ensures Lorenz gauge invariance of the light-matter theory [99]. The projection of the continuum theory of electronic matter fields $\Psi(\boldsymbol{x})$ interacting with the EM field

$$\hat{H} = \hat{H}_{\text{em}} + \int \mathrm{d}\boldsymbol{x}\, \hat{\Psi}^\dagger(\boldsymbol{x}) \left[\frac{(-i\hbar\boldsymbol{\nabla} + e\boldsymbol{A})^2}{2m} + V(\boldsymbol{x})\right] \hat{\Psi}(\boldsymbol{x}) + \dots \ , \tag{4.17}$$

where into a low-energy electronic basis $\hat{\Psi}^\dagger(\boldsymbol{x}) = \sum_{i\mu} \psi_{i\mu}(\boldsymbol{x})\hat{c}_{i\mu}$, where $\psi_{i\mu}(\boldsymbol{x})$ denotes electronic Wannier functions and $\hat{c}_{i\mu}$ the annihilation operator of electrons with orbital μ localised at site i, hides subtle issues regarding the preservation of gauge invariance [102]. It is advised [97] first to project the matter fields and then add the minimal coupling through the unitary transformation $\hat{H} \to \hat{U}^\dagger\hat{H}\hat{U}$, where $\hat{U} = \exp\left[i\sum_{\boldsymbol{k}s}(\hat{a}_{\boldsymbol{k}s} + \hat{a}^\dagger_{\boldsymbol{k}s}) \int \mathrm{d}\boldsymbol{x}\, \hat{\Psi}^\dagger(\boldsymbol{x})\chi_{\boldsymbol{k}s}(\boldsymbol{x})\hat{\Psi}(\boldsymbol{x})\right]$ and $\boldsymbol{\nabla}\chi_{\boldsymbol{k}s}(\boldsymbol{x}) = e\tilde{\boldsymbol{A}}_{\boldsymbol{k}s}(\boldsymbol{x})$. As a result, the EM field couples linearly to matter

$$\hat{H} = \hat{H}_{\text{em}} + i\sum_{\boldsymbol{k}s}\sum_{ij}\sum_{\mu\nu} \hbar\omega_{\boldsymbol{k}}\chi^{\mu\nu,ij}_{\boldsymbol{k}s} \left(\hat{a}_{\boldsymbol{k}s} - \hat{a}^\dagger_{\boldsymbol{k}s}\right) \hat{c}^\dagger_{i\mu}\hat{c}_{i\nu} + \hat{H}_{\text{matter}} \ , \tag{4.18}$$

where $\chi^{\mu\nu,ij}_{\boldsymbol{k}s} = \int \mathrm{d}\boldsymbol{x}\, \psi^*_{i\mu}(\boldsymbol{x})\chi_{\boldsymbol{k}s}(\boldsymbol{x})\psi_{j\nu}(\boldsymbol{x})$, and can induce and intra- or inter-site photon-mediated hybridisation/hopping terms as well, to a smaller degree, shift the orbital energies. In addition, the EM field generates a quartic, self-interaction term between matter fields [97], which was dropped due to being relevant only for strong light-matter coupling regimes.

Dipole selection rules

Assuming that the wavelength of the EM field is much larger than the atom size – atomic radii are of the order of 10^{-10}m, whereas THz radiation is of the order 10^{-4}m – to a good approximation, the EM field does not change over the atomic scale. As such, $\chi_{\boldsymbol{k}s}(\boldsymbol{x}) \approx e\tilde{\boldsymbol{A}}_{\boldsymbol{k}s}(\boldsymbol{x}) \cdot \boldsymbol{x}$ and the light-matter matrix-element reads

$$\chi^{\mu\nu,ij}_{\boldsymbol{k}s} = e\sqrt{\frac{\hbar}{2\omega_{\boldsymbol{k}}\varepsilon_0 V}}\boldsymbol{e}_{\boldsymbol{k}s} \cdot \int \mathrm{d}\boldsymbol{x}\, \psi^*_{i\mu}(\boldsymbol{x})\, \boldsymbol{x}\, \psi_{j\nu}(\boldsymbol{x}) \tag{4.19}$$

Due to the position operator in the integral kernel, for same-site coupling $i = j$, to a good approximation, light couples only matter in orbitals with different parity, in agreement with the selection rule $\Delta L = 1$ for light-induced transitions in the "dipole approximation".

Considering the d conduction bands and $4f$ bands of Section 4.1, the coupling of the EM field induces on-site transitions between the two orbitals. Neglecting effects of light-induced inter-site hopping, the coupling of the EM field to the Anderson lattice model (4.4) reads

$$\hat{H} = \sum_{\boldsymbol{k}s} \hbar\omega_{\boldsymbol{k}} \hat{a}^\dagger_{\boldsymbol{k}s} \hat{a}_{\boldsymbol{k}s} + \hbar g_0 \sum_{\boldsymbol{k}s} i \left(\hat{a}_{\boldsymbol{k}s} - \hat{a}^\dagger_{\boldsymbol{k}s} \right) \sum_{i\sigma} \left(\hat{c}^\dagger_{i\sigma} \hat{b}^\dagger_i \hat{f}_{i\sigma} + \text{h. c.} \right) + \hat{H}_{\text{ALM}} \ , \tag{4.20}$$

where an approximation similar to Weisskopf-Wigner's [103], where the light-matter coupling strength is assumed constant for the frequencies of interest $g^{\mu\nu,ij}_{\boldsymbol{k}s} \coloneqq \omega_{\boldsymbol{k}s} \chi^{\mu\nu,ij}_{\boldsymbol{k}s} \overset{!}{=} g_0 \delta_{d,f} \delta_{ij}$ is considered. This is ultimately related to the light-matter interaction, to a good approximation, not transfering momentum between electrons, as the momentum carried by a THz photon $q \sim 10^{-1}$ m^{-1} is much smaller than the typical Fermi momentum $k_F \sim 10^6$ m^{-1} – for the interaction expressed in momentum basis $\hat{H}_{\text{int}} \sim i \sum_{\boldsymbol{k}\boldsymbol{q}\sigma} \left(\hat{a}_{\boldsymbol{q}} - \hat{a}^\dagger_{-\boldsymbol{q}} \right) \left(\hat{c}^\dagger_{\boldsymbol{k}+\boldsymbol{q}\sigma} \hat{f}_{\boldsymbol{k}\sigma} + \text{h. c.} \right) \sim i \sum_{\boldsymbol{q}} \left(\hat{a}_{\boldsymbol{q}} - \hat{a}^\dagger_{-\boldsymbol{q}} \right) \sum_{\boldsymbol{k}\sigma} \left(\hat{c}^\dagger_{\boldsymbol{k}\sigma} \hat{f}_{\boldsymbol{k}\sigma} \right)$.

4.3 Dissipative dynamics

A difficulty encountered in the theoretical description of driven non-equilibrium systems is that the work done by external fields is transformed into heat through quantum scattering mechanisms [104]. Beyond the low-energy toy models used to describe strongly interacting systems, real materials interact further with *dissipative*[6] channels such as background photons, phonons or other electronic bands, which can remove the excess energy deposited by external fields. Adding an environment can be critical in controlling the population of high-energy states or maintaining the system's internal energy conserved on average. This is especially important in *continuously* driven systems, where a balance between the action of the driving field and the dissipation of high-energy electrons is necessary to reach some kind of stationary state. For a *short* drive such as an ultrafast pulse, a finite amount of energy is deposited in the system, and stationarity can be reached without coupling to an environment. However, depending on the intensity of the injected pulse, the resulting heating of the system may be unwanted if thermal fluctuations entirely wash out low-energy quantum effects.

A reservoir in thermal equilibrium – or heat bath – is typically modelled [104, 108] as a set of independent fermionic or bosonic modes described by a time-dependent Gibbs ensemble (1.11) and coupled through exchange terms to the system's electronic degrees of freedom. In a scenario where the environment is a heat bath, and the system's Hamiltonian becomes static, its stationary state is likely to be described by a Gibbs ensemble at the same temperature as the reservoir [105], a process known as *thermalisation*. The timescale at which a system thermalises depends on the possible channels of thermalisation, which not only depend on the system-bath coupling strength but also on momentum, energy or particle conservation constraints specific to the material.

[6] For a proper understanding of the meaning of "dissipative" channels, one has to introduce *open* quantum systems and their dynamics, which is beyond the intended scope of this thesis. In modelling an open system, the system of interest S is coupled to a *reservoir* R, an environment with infinite degrees of freedom. Despite the system plus reservoir defining a *closed* system – with unitary dynamics generated by their joint Hamiltonian, it can be assumed that the system S will have a negligible influence on the reservoir R, which can be traced out [105–107]. The elimination of these degrees of freedom results in an *open* description of the system S, with irreversible dynamics, due to information loss – or *decoherence* – to the environment.

Beyond the canonical way of treating open quantum systems through master equations[7], *irreversible* dynamics can be obtained by integrating out the reservoir and replacing all reservoir-related 2-point functions in (1.61) by *non-interacting* 2-point functions. Reservoirs are, by construction, not renormalised by interactions with the system, and such a procedure will enforce the self-energy of reservoir 2-point functions to vanish, effectively blocking those degrees of freedom from being affected by the interaction with the system. In opposition, the system is coupled to and renormalised by the reservoir. Hence, due to the asymmetrical nature of the system-reservoir coupling, information from the system will be lost to the reservoir, generating irreversible dynamics.

4.3.1 Fermionic heat bath

The Büttiker model [110] couples an identical fermionic reservoir to each lattice site

$$\hat{H}_{\text{bath}} = \sum_{\ell} \sum_{i\sigma} \varepsilon^a_\ell \hat{a}^\dagger_{\ell i\sigma} \hat{a}_{\ell i\sigma} + \alpha \sum_{\ell} \sum_{i\sigma} \left(\hat{c}^\dagger_{i\sigma} \hat{a}_{\ell i\sigma} + \text{h. c.} \right) \ , \tag{4.21}$$

where $\hat{a}^\dagger_{\ell i\sigma}$ is a reservoir electron creation operator of a fermion with spin σ at site i with energy ε_ℓ. The heat bath is, by definition, site and spin diagonal, and upon integration, generates the additional *non-interacting* effective action term

$$iS^{\text{bath}}_{\text{eff}} = \int_\gamma \mathrm{d}z\, \mathrm{d}z' \sum_{i\sigma} c^*_{i\sigma}(z) \left[\alpha^2 \Delta_a(z,z') \right] c_{i\sigma}(z') \ , \tag{4.22}$$

which is effectively an additional hybridisation of conduction electrons. The lack of momentum conservation resulting from such coupling is crucial to allow the electrons' momenta to relax from the excitation by external fields. The heat bath 2-point function reads

$$\Delta_a(z,z') = \int_{-\infty}^{+\infty} \mathrm{d}\varepsilon\, \rho^a_0(\varepsilon) \left[-i \left(\Theta_\gamma(z,z') - f(\varepsilon) \right) e^{-i\varepsilon(z-z')} \right] \ , \tag{4.23}$$

where $\rho^a_0(\varepsilon) = \sum_\ell \delta(\varepsilon - \varepsilon^a_\ell)$ is the bath density of states and f is the Fermi-Dirac distribution. It is important that the environment is infinitely large and involves a continuum of frequencies for

[7] Under a *Markovian* approximation of the reservoir R, with short correlation times, and the assumption of it not being significantly affected by the interaction with the system S (for which the factorisation of the total density matrix $\hat{\rho}(t) \overset{!}{=} \hat{\rho}_S(t) \otimes \hat{\rho}_R$ can hold), the reservoir degrees of freedom are traced out [105–107] resulting in the quantum master equation

$$\partial_t \hat{\rho}_S = \hat{\mathcal{L}}\, \hat{\rho}_S = -i \left[\hat{H}, \hat{\rho}_S \right] + \mathcal{D}[\mathcal{L}] = -i \left[\hat{H}, \hat{\rho}_S \right] + \sum_\alpha \kappa_\alpha \left(\hat{L}_\alpha \hat{\rho}_S \hat{L}^\dagger_\alpha - \frac{1}{2} \left\{ \hat{L}^\dagger_\alpha \hat{L}_\alpha, \hat{\rho}_S \right\} \right) \ .$$

While the first part of the *Liouvillian* $\hat{\mathcal{L}}$ describes the unitary/coherent dynamics generated by Hamiltonian $\hat{H}$ – as encountered in the von Neumann equation, the second part $\mathcal{D}[\hat{\mathcal{L}}]$ describes the *dissipative* dynamics that result from the connection to the environment. The jump operator $\hat{L}_\alpha$ is the remnant system operator which was coupled to the environment and κ_α encodes an effective coupling strength to the environment. Note that a series of other approximations were employed in obtaining the κ_α, which generally can be time-dependent.

The transformation from the quantum master equation to a path integral formulation follows a similar procedure to Section 1.4.1 and can be found in detail in [109]. In short, the dissipator $\mathcal{D}[\hat{\mathcal{L}}]$ enters the Keldysh action (1.47) as

$$\sum_\alpha \kappa_\alpha \left\{ L_\alpha(t_-) L^*_\alpha(t_+) - \frac{1}{2} \left[L^*_\alpha(t_-) L_\alpha(t_-) + L^*_\alpha(t_+) L_\alpha(t_+) \right] \right\} \ ,$$

and couples the forward and backward branches of the contour, ultimately breaking the cancellation of the forward and backward action of the contour under unitary time evolution.

the bath Green functions to decay in time (cf. Section 6.2.3) and properly generate irreversible dynamics [105]. For a small system-bath coupling strength α, the effect of the bath on the original conduction electron bandwidth is negligible and the details of $\rho_0^a(\varepsilon)$ unimportant. As such, it is typically taken as a flat density of states or being the same as the conduction electrons' bare one. Due to the particle-exchange character of the coupling, the reservoir can also tune the total electronic particle number of the system.

4.3.2 Bosonic heat bath

Another way to incorporate dissipation into the electronic system is via baths of bosonic particles – typically phonons or photons. This kind of coupling allows energy exchange with the environment but, unlike the former, microscopically conserves electronic particle number due to the conservation of electronic charge. The resulting system-bath coupling is hence an interacting vertex and can introduce more interesting thermalisation transients [111] than their fermionic counterpart. As such, the inclusion of bosonic bath channels requires perturbative expansions, and hence it will be assumed that the system-bath coupling strength α is small[8].

Ohmic bath The Holstein model adds a minimal coupling between phonon modes and the electronic degrees of freedom and is used to describe the effects of vibrations in such systems [112]

$$\hat{H}_{\text{bath}} = \sum_{\ell}\sum_{i\sigma} \hbar\omega_\ell^a \hat{a}_{\ell i}^\dagger \hat{a}_{\ell i} + \alpha \sum_{\ell}\sum_{i\sigma} \left(\hat{c}_{i\sigma}^\dagger \hat{c}_{i\sigma} - \hat{\mathbb{1}}\right)\left(\hat{a}_{\ell i}^\dagger + \hat{a}_{\ell i}\right) \ , \tag{4.24}$$

where $\hat{a}_{\ell i}^\dagger$ is a reservoir phonon creation operator of a particle with frequency ω_ℓ at site i and α is the coupling strength between the phonon modes and the conduction electrons. By integrating out the phonon degrees of freedom, a dissipative channel enabling energy and momentum relaxation arises through a new *interacting* effective action term

$$iS_{\text{eff}}^{\text{bath}} = \int_\gamma \mathrm{d}z\,\mathrm{d}z' \sum_{i\sigma} \left[c_{i\sigma}^*(z)c_{i\sigma}(z) - 1\right] i\alpha^2 \left[\Pi_a(z,z') + \Pi_a(z',z)\right] \left[c_{i\sigma}^*(z')c_{i\sigma}(z') - 1\right] \ , \tag{4.25}$$

for which the lowest order loop expansion results in a self-energy contribution to the conduction electrons [113, 114]. The heat bath 2-point function reads

$$\Pi_a(z,z') = \int_{-\infty}^{+\infty} \mathrm{d}\varepsilon\, \rho_0^a(\varepsilon) \left[-i\left(\Theta_\gamma(z,z') + b(\varepsilon)\right) e^{-i\varepsilon(z-z')}\right] \ , \tag{4.26}$$

where

$$\rho_0^a(\varepsilon) = \sum_\ell \delta(\varepsilon - \omega_\ell^a) = \varepsilon \frac{\Lambda^2}{\varepsilon^2 + \Lambda^2}\Theta(\varepsilon) \tag{4.27}$$

is an ohmic density of states, linear at low frequencies and with a soft cut-off Λ and b is the Bose-Einstein distribution function. While in normal conductors, it is known that the thermalisation time is generally within dozens/hundreds of femtoseconds, it can go up to 100 picoseconds in heavy-fermion compounds. It has been hypothesized [115] that this is due to the suppression of electron-phonon scattering in the vicinity of the Fermi energy. Due to the flat bands near the Fermi energy, the Fermi velocity can be slower than the sound velocity, which in turn, suppresses the phase space available for the elastic scattering between electrons and phonons, dramatically increasing the thermalisation time via phonon scattering.

[8] Refer to [112] for strong system-bath couplings.

4.3.3 Photonic heat bath

Although the hypothesised suppression of phononic scattering in heavy-fermion compounds, another possible channel of bosonic thermalisation is through spontaneous emission. Namely, in heavy-fermion systems, electrons in the conduction band can fill holes in the valence band via the spontaneous emission of a photon, a process known as *radiative recombination*. This exchange arises due to the EM field coupling electronic states of different orbitals and, due to the small momentum carried by photons, transitions effectively not transferring momenta (Section 4.2.2).

Continuous-mode light

In quantum optics, the EM field is usually confined within a cavity, for which *box quantisation* results in a complete set of discrete modes. However, for optical experiments such as THz spectroscopy, there is no identifiable cavity, but rather light flowing from a source through some interaction region to a set of detectors. In the absence of a cavity, physical quantities such as the light-matter coupling strength (4.19) should hence not be determined by the quantisation volume. Moreover, real experiments are more accurately described by Gaussian beams of light instead of plane waves, and more quantitative calculations require a vastly different quantisation procedure [116]. To quantise the EM field in *free space* [117], the quantisation volume goes to infinity $V \to \infty$, such that the sum over the discrete modes

$$\sum_{\boldsymbol{k}} \to \frac{1}{\Delta k} \int \mathrm{d}\boldsymbol{k} \tag{4.28}$$

is converted to an integral, where $\Delta k = \frac{(2\pi)^3}{V}$, and the discrete-mode creation and annihilation operators are related to *continuous-mode* ones through

$$\hat{a}_{\boldsymbol{k}} \to \sqrt{\Delta k}\hat{a}(\boldsymbol{k}) \qquad \hat{a}^\dagger_{\boldsymbol{k}} \to \sqrt{\Delta k}\hat{a}^\dagger(\boldsymbol{k}) \ , \tag{4.29}$$

satisfying the continuous-mode commutation relation

$$\left[\hat{a}(\boldsymbol{k}), \hat{a}^\dagger(\boldsymbol{k}')\right] = \delta(\boldsymbol{k} - \boldsymbol{k}') \ . \tag{4.30}$$

The continuous-mode vector potential (4.12) reads

$$\hat{\boldsymbol{A}}(\boldsymbol{x}, t) = \int \frac{\mathrm{d}\boldsymbol{k}}{(2\pi)^{3/2}} \sum_s \sqrt{\frac{\hbar}{2\omega(\boldsymbol{k})\varepsilon_0}} \left[e^{i(\boldsymbol{k}\cdot\boldsymbol{x} - \omega(\boldsymbol{k})t)} \boldsymbol{e}_s(\boldsymbol{k})\hat{a}_s(\boldsymbol{k}) + \mathrm{h.\,c.}\right] \ , \tag{4.31}$$

and partitioning the integral into sections of the solid angle $\int \mathrm{d}\boldsymbol{k} \to \int \mathrm{d}k\, k^2 \sum_m \int \mathrm{d}\Omega_m$, with area $\Delta\Omega_m \equiv \int_{\Omega_m} \mathrm{d}\Omega$, results a decomposition of one-dimensional modes at $\boldsymbol{x} = 0$ in the limit $\Delta_m \to 0$ [118]

$$\hat{\boldsymbol{A}}(t) = \sum_{ms} \int_0^\infty \mathrm{d}\omega \sqrt{\frac{\hbar\omega\Delta\Omega_m}{16\pi^3\varepsilon_0 c^3}} \left[e^{-i\omega t} \boldsymbol{e}_{ms}\hat{a}_{ms}(\omega) + \mathrm{h.\,c.}\right] \ , \tag{4.32}$$

where $\hat{a}_{ms}(\omega)$ is an annihilation operator of a mode with frequency ω, solid angle section m and polarisation s. The bare Hamiltonian of the continuous-mode EM field reads

$$\hat{H}_{\mathrm{em}} = \sum_{ms} \int_0^\infty \mathrm{d}\omega\, \hbar\omega \hat{a}^\dagger_{ms}(\omega)\hat{a}_{ms}(\omega) \ , \tag{4.33}$$

where the vacuum energy was removed. The EM field vacuum (a state devoid of photons) contains an infinite amount of energy $E_{\mathrm{vac}} = \frac{1}{2}\sum_{ms}\int_0^\infty \mathrm{d}\omega\hbar\omega$ and is a result of vacuum fluctuations. However, this superficial divergence in free space is trivially removed as it simply defines the reference from which all energies must be calculated.

Photonic heat bath

The quantum nature of the EM field in free space generates an infinite number of modes that serve as a reservoir to which atoms can radiate. This kind of irreversible disappearance of light quanta cannot occur in a box since light cannot be lost by bouncing back (either physically or theoretically through periodic boundary conditions). In free space, (4.33) forms the bath into which the system (4.4) can radiate to

$$\hat{H}_{\text{bath}} = \hat{H}_{\text{em}} + \hbar g_0 \sqrt{\eta} \sum_{ms} \int \mathrm{d}\omega \, i \left(\hat{a}_{ms}(\omega) - \hat{a}^\dagger_{ms}(\omega) \right) \sum_{i\sigma} \left(\hat{c}^\dagger_{i\sigma} \hat{b}^\dagger_i \hat{f}_{i\sigma} + \text{h. c.} \right) \ , \tag{4.34}$$

where η is a dimensionless parameter characterising the strength of the coupling to the EM field environment. Note that the prefactors of g_0 in (4.34) are slightly different from the ones in (4.20). Integrating out the photonic degrees of freedom generates the new *interacting* effective action term

$$i S^{\text{bath}}_{\text{eff}} = \int_\gamma \mathrm{d}z \ \mathrm{d}z' \sum_{i\sigma} \left[c^*_{i\sigma}(z) b^*_i(z) f_{i\sigma}(z) + \text{h. c.} \right] \hbar^2 i g_0^2 \eta \left[\Pi_a(z,z') + \Pi_a(z',z) \right] \left[c^*_{i\sigma}(z') b^*_i(z') f_{i\sigma}(z') + \text{h. c.} \right] \ , \tag{4.35}$$

where $\Pi_a(z,z')$ is described by (4.26). Despite $\Lambda \to \infty$ in the EM field vacuum, a soft cut-off to the density of states is kept because the light-matter coupling was assumed to be constant in frequency, which must be remedied by a cut-off in the coupling to high-energy vacuum modes.

4.4 Travelling pulse of light

When a travelling pulse of quantum radiation interacts with non-linear quantum systems in free space, its photon number content or temporal mode ("wavepacket shape") may change due to quantum absorptive or dispersive effects. The main difficulty of treating such systems is that due to spontaneous emission, not only can the structure of the temporal mode change, the emission is, in general, not restricted to that specific mode [119]. The theoretical frameworks that treat the interaction of such travelling pulses of quantum radiation with quantum systems date back to the influential input-output theory [120]. Here, the *output* radiation (asymptotically free after interaction) can be related to the *input* radiation (asymptotically free before interaction) through the simple formula

$$\hat{a}_{\text{out}}(t) = \hat{a}_{\text{in}}(t) + g \, \hat{c}(t) \ , \tag{4.36}$$

where g denotes an effective coupling between some system (c) and radiation (a). However[9], this requires a series of considerations [120] incompatible with the system (4.4), namely the rotating wave approximation – in continuum systems, there are no characteristic slow and fast frequencies.

[9] Recent extensions [121] to this theory can describe an incident mode of radiation acting on some non-linear interacting system. The key idea is that a cavity driven by white noise (i.e., coupled to a Markovian environment) can be engineered to generate coloured noise [122], i.e. any arbitrary input radiation can be generated by choosing appropriate jump operators and manipulating the pump/loss rates (Footnote 7). A pulse of radiation interacting with a cavity is then treated as an open (cascaded [123]) quantum system, where an upstream pseudo-cavity leaks the *input* radiation that drives the cavity-system of interest, with the *output* radiation mode being acquired by some downstream pseudo-cavity. While this technique should, in principle, be able to model the interaction of a travelling pulse with an Anderson lattice model, the two pseudo-cavities mentioned above can only describe interaction with a single mode of the incident and outgoing radiation, with the rest of the modes being treated as loss. Hence, it can be used to examine the quantum contents of a specific output temporal mode after interaction with the system of interest. While the theory can be extended [124] to multi-input and output modes, it becomes prohibitively expensive as the number of modes grows.

Since the non-equilibrium field theory was framed concerning 2-point functions, related with ensemble averages, and not specific quantum states, the modelling of a travelling pulse in free space needs only to be resolved at the level of Green functions and can hence be reverse-engineered through the investigations of Section 1.3.2. Assuming a one-dimensional Gaussian pulse to be travelling along some direction, with a carrier frequency ω_0 and Gaussian envelope [125] $\xi_{\Omega_0}(t)$ centred at and T_0

$$\xi_{\Omega_0}(t) = \exp\left(-\frac{\Omega_0^2}{4}t^2\right) \ , \tag{4.37}$$

where Ω_0 denotes the frequency width of the pulse, the electric field pulse at $\boldsymbol{x} = 0$ (cf. (4.32)) reads

$$\hat{\boldsymbol{E}}(t) \approx \sum_s \sqrt{\frac{\hbar\omega_0^3 \Delta\Omega_{\mathrm{P}}}{16\pi^3\varepsilon_0 c^3}} e^{-i\omega_0 t}\xi_{\Omega_0}(t-T_0)\boldsymbol{e}_s(\omega_0)\hat{a}_s(\omega_0) + \mathrm{h.c.} \ , \tag{4.38}$$

assuming enveloping bandwidths much smaller than the carrier frequency and $\Delta\Omega_{\mathrm{P}}$ the solid angle covered by the pulse. The intensity at $\boldsymbol{x} = 0$, determined by the Poynting operator, for linearly polarised light [98]

$$\hat{I}(t) = 2\varepsilon_0 c\hat{\boldsymbol{E}}^-(t)\cdot\hat{\boldsymbol{E}}^+(t) \ , \tag{4.39}$$

where $\hat{\boldsymbol{E}}^{\pm}(t)$ denotes the forward and backward components of EM field of (4.38), respectively, is proportional to the number of photons

$$\hat{I}(t) = \frac{\hbar\omega_0}{\tilde{A}}\hat{a}^\dagger(\omega_0)\hat{a}(\omega_0)\left(\xi_{\Omega_0}(T-T_0)e^{-i\omega_0 t}\right)^*\left(\xi_{\Omega_0}(T-T_0)e^{-i\omega_0 t}\right) \ , \tag{4.40}$$

where $\tilde{A} = \frac{4\pi^3 c^2}{\Delta\Omega_P \omega_0^2}$. A generalisation of the Poynting operator to two times results in an expression for the lesser Green function of the pulse $i\,G^<_{a_0}(t,t')\big|_{t'\to t} \sim \frac{\tilde{A}}{\hbar\omega_0}\langle\hat{I}(t)\rangle$. In Wigner coordinates, it reads

$$G^<_{a_0}(T,\tau)_{\mathrm{W}} = -i\bar{n}_a\xi_{\sqrt{2}\Omega_0}(T-T_0)e^{-i\omega_0\tau}\xi_{\Omega_0/\sqrt{2}}(\tau) \ , \tag{4.41}$$

where $\bar{n}_a$ is the maximum number of photons in the Gaussian mode, $\xi_{\sqrt{2}\Omega_0}(T-T_0)$ controls the modulation of the occupation and $e^{-i\omega_0\tau}\xi_{\Omega_0/\sqrt{2}}(\tau)$ controls the spectral content of the Green function – its Fourier transform is a normalised Gaussian distribution with width $\Omega_0/\sqrt{2}$ centred at frequency ω_0[10]. Note that this implies that the pulse's distribution function is flat in frequency, which differs significantly from the ones found in thermal equilibrium, such as the Bose-Einstein distribution. While it would be possible to control the occupation by a time-dependent chemical potential and a Bose-Einstein distribution, this was not considered as that would mean that the field occupation has different spectral decompositions at different times. Since the pulse field can be considered non-interacting, the greater Green function

$$G^>_{a_0}(T,\tau)_{\mathrm{W}} = -i\left(1+\bar{n}_a\xi_{\sqrt{2}\Omega_0}(T-T_0)\right)e^{-i\omega_0\tau}\xi_{\Omega_0/\sqrt{2}}(\tau) \ , \tag{4.43}$$

[10]The spectral content of a photonic pulse being a Gaussian distribution contains the problem that for $\omega_0 < \Omega_0$, there is a significant portion of the photonic field with *unphysical* zero and negative energies. To eliminate this spectral region, the spectral information can instead be encoded by the half-Fourier transform

$$e^{-i\omega_0\tau}\xi_{\Omega_0/\sqrt{2}}(\tau) \to \int_0^{+\infty}\frac{\mathrm{d}\omega}{2\pi}e^{-i\omega\tau}\,\omega\int_{-\infty}^{+\infty}\mathrm{d}\tau'\,e^{+i\omega\tau'}\left[e^{-i\omega_0\tau'}\xi_{\Omega_0/\sqrt{2}}(\tau')\right] \ , \tag{4.42}$$

which ensures the photons always have positive energies.

ensures the spectral content of the pulse is constant in centre-of-mass time. The resulting equations of motion read[11]

$$\begin{aligned} i\partial_t G^<_{a_0}(t,t') &= \left(\omega_0 - i\frac{\Omega_0^2}{4}(t-t')\right) G^<_{a_0}(t,t') - i\frac{\Omega_0^2}{2}\left(\frac{t+t'}{2} - T_0\right) G^<_{a_0}(t,t') \\ i\partial_t G^>_{a_0}(t,t') &= \left(\omega_0 - i\frac{\Omega_0^2}{4}(t-t')\right) G^>_{a_0}(t,t') - i\frac{\Omega_0^2}{2}\left(\frac{t+t'}{2} - T_0\right) G^<_{a_0}(t,t') \end{aligned} \tag{4.44}$$

Note that the travelling pulse of light is only resolved at the level of 2-point functions, and expressions for higher-point functions would require further analysis.

The main challenge arising from a THz pulse interacting with a heavy-fermion system is the no separation of the timescales. The bandwidth of the pulse sets the duration of the interaction $\Omega_0 \not\ll k_{\mathrm{B}} T_K^*$, which is in the same scale as the Kondo coherence temperature. This results in proper non-equilibrium dynamics, which prevents the problem from being simplified, for example, by being cast into a quasi-static form (Section 1.3.2).

[11] These equations of motion have a striking similarity to those found in open quantum systems described by a quantum master equation (Footnote 7). Due to the difficulty of resolving the joint photon-system interactions, the standard technique is to integrate the photonic input field and study the resulting effective cavity. For a single-particle pumping $\hat{L} = \hat{a}^\dagger$ and loss $\hat{L} = \hat{a}$, with respective effective pump κ_p and loss rate κ_l, the equations of motion for a non-interacting Hamiltonian $\hat{H} = \omega_0 \hat{a}^\dagger \hat{a}$ read

$$\begin{aligned} i\partial_t G^<(t,t') &= \left[\omega_0 - \frac{i}{2}\left(\kappa_l(t) + \kappa_p(t)\right)\right] G^<(t,t') + i\kappa_p(t)\left[\Theta(t-t')G^<(t,t') + \Theta(t'-t)G^>(t,t')\right] \\ i\partial_t G^>(t,t') &= \left[\omega_0 + \frac{i}{2}\left(\kappa_l(t) + \kappa_p(t)\right)\right] G^>(t,t') - i\kappa_l(t)\left[\Theta(t-t')G^>(t,t') + \Theta(t'-t)G^<(t,t')\right] \ . \end{aligned}$$

While it is not possible to compare them directly with (4.44), it can be argued that the imaginary terms of the right-hand-side are similar to time-dependent loss/pump rates – however, unlike the rates found in Markovian dynamics [126], these are not necessarily positive-definite.

Chapter 5

Non-equilibrium saddle-point theory

Saddle-point approximations are ubiquitous in condensed-matter theory. At heart, these theories approximate the quantum averaging of the partition function (1.49) by a single *classical* field contribution. That is, in the classical limit $\hbar \to 0$, the integral of the partition function

$$Z = \int D\left[\phi\right] e^{iS[\phi]/\hbar} \,, \tag{5.1}$$

is dominated by the extremum of $S\left[\phi\right]$, with the amplitudes from the other quantum paths destructively interfering with each other [127]. This results in Euler-Lagrange equations of motion for the now "classical" ϕ_0 field, which satisfies the saddle-point condition

$$\left.\frac{\delta S[\phi]}{\delta \phi}\right|_{\phi=\phi_0} = 0 \,. \tag{5.2}$$

Such theories have successfully described many complex phenomena, such as superconductivity [128] or Bose-Einstein condensates [129]. The caveat is that the approximation is only valid if the amplitude of the quantum fluctuations $\delta\phi \coloneqq \phi - \phi_0$ around the classical field ϕ_0 is small. In general, the saddle-point condition identically satisfies an associated mean-field theory, where a mean-field $\bar{\phi}$ extremises the free energy $F[\phi] = -\frac{1}{\beta}\log Z[\phi]$. Equivalently, the mean-field theory is only valid if the free energy associated with the fluctuations is much smaller than the mean-field free energy. The Ginzburg criterion dictates the validity of the mean-field approximation in equilibrium systems: fluctuations only become relevant when their length scale is longer than the system's correlation length. In non-equilibrium systems, however, much less is understood.

Saddle-point theories were among the earliest successes in describing Kondo regimes via auxiliary-particle techniques (Chapter 2). Seemingly counterintuitive, given the strongly-interacting nature of Kondo physics, there is a direct correspondence between the Kondo temperature and the fields' saddle points at zero temperature. This fortuitous coincidence makes saddle-point theory a powerful starting point when studying this class of problems as it offers a window into the underlying physics at a fraction of the cost of resolving the properly interacting[1] theory. However, it should be noted that auxiliary-particle saddle-point approximations suffer from severe fundamental problems, such as featuring a spurious phase transition (vanishing saddle-point solution) at finite temperatures [130] or displaying a Fermi liquid phase in multi-channel (non-Fermi liquid) models. Nevertheless, for an Anderson lattice model in the $U \to \infty$ regime in thermal equilibrium, the saddle-point approximation and

[1] Note that even at the saddle-point, auxiliary-particle theories are, in general, *strongly interacting* due to the constraint. What is meant is that the quantum fluctuations are neglected.

associated fluctuations are well-understood [92, 131]. For Anderson-impurity models in non-equilibrium regimes, some saddle-point formulations have been proposed. However, these have been applied only to quasi-equilibrium problems, such as quantum-dot steady-states [132, 133], high-frequency Floquet drive [134] and almost-adiabatic [135] drive. A proper solution in time – which requires the problem to be formulated and solved in the Keldysh contour – is still lacking. This is most likely due to the complicated form of the resulting equations of motion – a set of differential-algebraic equations. Driven by the non-separable timescales that dictate the time-evolution of the system (Section 4.4), a general non-equilibrium saddle-point theory of auxiliary particles for a time-resolved pulse of light interacting with an Anderson lattice is developed.

5.1 Non-equilibrium effective action

The partition function associated with the pulse of light interacting with an Anderson lattice has several field degrees of freedom that must be summed over. Ideally, the more these degrees of freedom are integrated, the more quantum effects are contained in the resulting effective action. Concerning the Hamiltonian of interest (6.1), one could integrate the auxiliary bosons and derive an effective theory with boson-mediated electron interactions. However, this theory would require further transformations, such as the Hubbard-Stratonovich, to decouple the new effective interacting terms between matter fields. This is not only more laborious, but it also dismisses the great appeal of treating the auxiliary bosons and constraint at the saddle-point: their amplitude is directly proportional [131] to the Kondo temperature (Section 4.1.1) of the system

$$\begin{aligned} V_0\rho_0^c(\varepsilon_F)|b_0|^2 &\approx T_K \qquad \text{for the single-impurity Anderson model,} \\ \lambda_0 - \varepsilon_0^f &\sim T_K^* \qquad \text{for the Anderson lattice model.} \end{aligned} \tag{5.3}$$

Fulfilling the constraint (4.5) at every lattice site j can conveniently be imposed via the path-integral formalism, with the introduction of several Lagrange multipliers λ_j. In essence, a *projection* [131] of the partition function onto the $U \to \infty$ subspace[2]

$$Z_{\text{physical}} = \left(\prod_j \mathbb{P}_j \right) Z \ , \tag{5.4}$$

via some projector $\mathbb{P}_j$

$$\mathbb{P}_j = \int_{-\pi}^{\pi} \frac{\mathrm{d}\lambda_j}{2\pi} e^{-i\lambda_j \left(\hat{Q}_j - \hat{\mathbb{1}}\right)} \ , \tag{5.5}$$

is required. Moreover, the introduction of the auxiliary particles adds a gauge degree of freedom

$$f_{j\sigma}(z) \to e^{i\phi_j(z)} f_{j\sigma}(z) \qquad b_j(z) \to e^{i\phi_j(z)} b_j(z) \ , \tag{5.6}$$

[2]Note that the action of the operator $\mathbb{P}$ amounts to the Abrikosov projection (Section 2.1). By a change of variables to the fugacity, where $\zeta = e^{-i\lambda}$, the projector reads

$$\mathbb{P} := \oint \frac{\mathrm{d}\zeta}{2\pi i} \frac{1}{\zeta^2} f(\zeta) = \lim_{\zeta \to 0} \frac{\mathrm{d}}{\mathrm{d}\zeta} f(\zeta) = \lim_{\zeta \to 0} \hat{Q} \zeta^{\hat{Q} - \hat{\mathbb{1}}} \ ,$$

with $f(\zeta) = \zeta^{\hat{Q}}$. The projection of the partition function $\mathbb{P}Z \equiv \lim_{\zeta \to 0} \hat{Q}\zeta^{\hat{Q}-\hat{\mathbb{1}}} Z_G$ is hence entirely equivalent to (2.7), modulo a scaling factor.

which is known [136] to produce divergences in the auxiliary-boson Green function. The radial gauge

$$\lambda_j \to \lambda_j - i\partial_z \phi_j(z) =: \lambda_j(z) \ , \tag{5.7}$$

promotes λ to a field while leaving the action invariant under gauge transformations

$$S[\cdot, \lambda_j(z)] \to S[\cdot, \lambda_j(z) - i\partial_z \phi_j] = S[\cdot, \lambda(z)] + \int_\gamma \mathrm{d}z \, i\partial_z \left(\frac{1}{2} \left| b_j(t) \right|^2 + \phi_j(z) \right) \ , \tag{5.8}$$

as the last term is a total derivative term and vanishes. The invariance under gauge transformations is especially important [130] since, according to Elitzur's theorem, a non-zero saddle-point solution of the b fields is only possible for gauge-invariant theories.

In anticipation of the saddle-point approximation and considering the system to be infinite and translational invariant, the constraint field λ, as well as b, are site-independent, i.e., $\lambda_i = \lambda$ and $b_i = b$. The resulting projected partition function (5.4), from now referred as Z, reads

$$Z = \int D\left[b^*, b\right] D\left[c^*, c\right] D\left[f^*, f\right] D\left[a^*, a\right] D\left[\lambda\right] e^{iS[b^*, b, c^*, c, f^*, f, a^*, a, \lambda]} \ , \tag{5.9}$$

where the Keldysh action $S\left[b^*, b, c^*, c, f^*, f, a^*, a, \lambda\right]$ is given by

$$\begin{aligned} S\left[b^*, b, c^*, c, f^*, f, a^*, a, \lambda\right] = \int_\gamma \mathrm{d}z \Bigg\{ & \mathcal{N} b^*(z) \left[i\partial_z - \lambda(t) \right] b(z) + a^*(z) G_a^{-1}(z, z) a(z) \\ & + \sum_{\boldsymbol{k}\sigma} \begin{bmatrix} c^*_{\boldsymbol{k}\sigma}(z) & f^*_{\boldsymbol{k}\sigma}(z) \end{bmatrix} \boldsymbol{G}^{-1}_{\boldsymbol{k}\sigma, \boldsymbol{k}\sigma}(z, z) \begin{bmatrix} c_{\boldsymbol{k}\sigma}(z) \\ f_{\boldsymbol{k}\sigma}(z) \end{bmatrix} + \mathcal{N}\lambda(z) \Bigg\} \ , \end{aligned} \tag{5.10}$$

where $\mathcal{N} =: \sum_j 1$ denotes the number of lattice sites, $G_a^{-1}(z, z')$ the inverse Green function of the photonic fields, and the fermionic inverse Green function $\boldsymbol{G}^{-1}_{\boldsymbol{k}\sigma, \boldsymbol{k}'\sigma'}(z, z')$ is given by

$$\boldsymbol{G}^{-1}_{\boldsymbol{k}\sigma, \boldsymbol{k}'\sigma'}(z, z') = \Bigg[\underbrace{\begin{bmatrix} i\partial_z - \varepsilon^c_{\boldsymbol{k}\sigma} & -V_0 b^*(z) \\ -V_0 b(z) & i\partial_z - \varepsilon^f_0 - \lambda(z) \end{bmatrix}}_{\boldsymbol{G}_0^{-1}} - ig_0 \underbrace{\left(a(z) - a^*(z) \right) \begin{bmatrix} 0 & b^*(z) \\ b(z) & 0 \end{bmatrix}}_{\boldsymbol{A}} \Bigg] \delta_\gamma(z, z') \delta_{\boldsymbol{k}\boldsymbol{k}'} \delta_{\sigma\sigma'} \ . \tag{5.11}$$

Note that while $\boldsymbol{G}^{-1}$ is block-diagonal in $\boldsymbol{k}$ and σ space, the time differential operator ∂_z is formally non-diagonal (Section 1.4), as the continuous-time notation is but an abbreviation of the discrete path integral. For this reason, $\boldsymbol{G}^{-1}$ and its inverse are labelled by one momentum and spin index but by two time indices. This has important implications in the evaluation of the saddle-point equations, where, due to the definition of the δ-distribution, $\boldsymbol{G}(z, z) = \boldsymbol{G}(z, z + 0^+)$ which evaluates to $\boldsymbol{G}^<(t, t)$ for any $z \in \gamma$ in the Keldysh contour γ.

By integrating out the Grassmann fields, the effective action S_{eff} reads

$$\begin{aligned} S_{\text{eff}}\left[b^*, b, a^*, a, \lambda\right] = & -i \operatorname{tr} \log \left[-i\boldsymbol{G}^{-1} \right] \\ & + \int_\gamma \mathrm{d}z \left\{ \mathcal{N} b^*(z) \left[i\partial_z - \lambda(z) \right] b(z) + a^*(z) G_a^{-1}(z, z) a(z) + \mathcal{N}\lambda(z) \right\} \ . \end{aligned} \tag{5.12}$$

Note that the first term traces over *all* degrees of freedom of $\boldsymbol{G}$, including time. Furthermore, unless explicitly denoted by its discrete or continuous components, any boldface symbol should

be considered to contain all respective degrees of freedom. For an invertible $\boldsymbol{G}_0^{-1}$, the logarithm can be expanded as

$$\operatorname{tr}\log -i\boldsymbol{G}^{-1} = \operatorname{tr}\log\left[-i\boldsymbol{G}_0^{-1}\left(\mathbb{1} - ig_0\boldsymbol{G}_0\boldsymbol{A}\right)\right] = \operatorname{tr}\log -i\boldsymbol{G}_0^{-1} - \sum_{n=1}^{+\infty}\frac{(ig_0)^n}{n}\operatorname{tr}\left(\boldsymbol{G}_0\boldsymbol{A}\right)^n \ , \quad (5.13)$$

with

$$\begin{aligned}\operatorname{tr}\left(\boldsymbol{G}_0\boldsymbol{A}\right) &= \sum_{\boldsymbol{k}\boldsymbol{k}'}\sum_{\sigma\sigma'}\int_\gamma \mathrm{d}z\,\mathrm{d}z'\ \operatorname{tr}\left\{\boldsymbol{G}_{0_{\boldsymbol{k}\sigma,\boldsymbol{k}'\sigma'}}(z,z')\boldsymbol{A}_{\boldsymbol{k}'\sigma',\boldsymbol{k}\sigma}(z',z)\right\} \\ &= \int_\gamma \mathrm{d}z \underbrace{\left[\sum_{\boldsymbol{k}\sigma}\left(G^{(cf)}_{0_{\boldsymbol{k}\sigma}}(z,z)b(z) + G^{(fc)}_{0_{\boldsymbol{k}\sigma}}(z,z)b^*(z)\right)\right]}_{\alpha(z)}\left[a(z)-a(z)^*\right] \ . \end{aligned} \quad (5.14)$$

For a light-matter coupling far away from the ultrastrong regime $g_0 < 1$ and a small photon number $\langle\hat{a}^\dagger(z)\hat{a}(z)\rangle \lesssim 1$, it is justified to truncate the expansion at linear order. The photon fields are integrated by *completing the square*

$$\begin{aligned} Z &= e^{\operatorname{tr}\log -i\boldsymbol{G}_0^{-1}}\int D\left[b^*,b\right]D\left[\lambda\right]e^{i\int_\gamma \mathrm{d}z\left\{\mathcal{N}b^*(z)\left[i\partial_z-\lambda(z)\right]b(z)+\mathcal{N}\lambda(z)\right\}} \\ &\times \int D\left[a^*,a\right]e^{i\int_\gamma \mathrm{d}z\left\{a^*(z)G_a^{-1}(z,z)a(z)+g_0\,\alpha(z)i\left[a(z)-a(z)^*\right]+\mathcal{O}(g_0^2)\right\}} \\ &\simeq \int D\left[b^*,b\right]D\left[\lambda\right]e^{iS_{\text{eff}}[b^*,b,\lambda]} \ , \end{aligned} \quad (5.15)$$

where

$$\begin{aligned} S_{\text{eff}}\left[b^*,b,\lambda\right] &= -i\operatorname{tr}\log -i\boldsymbol{G}_0^{-1} + i\operatorname{tr}\log -i\boldsymbol{G}_a^{-1} \\ &+ \int_\gamma \mathrm{d}z\ \left\{\mathcal{N}b^*(z)\left[i\partial_z-\lambda(z)\right]b(z)+\mathcal{N}\lambda(z)\right\} - \int_\gamma \mathrm{d}z\ \mathrm{d}z'\,g_0^2\,\alpha(z)G_a(z,z')\alpha(z') \ . \end{aligned} \quad (5.16)$$

Note that the truncation of the log term at linear order neglects the renormalisation of the photon pulse arising from higher order coupling terms, e.g.,

$$\begin{aligned} \operatorname{tr}\left(\boldsymbol{G}_0\boldsymbol{A}\boldsymbol{G}_0\boldsymbol{A}\right) &= \int_\gamma \mathrm{d}z\,\mathrm{d}z'\sum_{\boldsymbol{k}\sigma}\left[a^*(z)+a(z)\right]\left[a^*(z')+a(z')\right] \\ &\times\Big[b(z)G^{(fc)}_{0_{\boldsymbol{k}\sigma}}\left(z,z'\right)G^{(fc)}_{0_{\boldsymbol{k}\sigma}}\left(z',z\right)b(z') + b(z)G^{(ff)}_{0_{\boldsymbol{k}\sigma}}\left(z,z'\right)G^{(cc)}_{0_{\boldsymbol{k}\sigma}}\left(z',z\right)b^*(z') \\ &+ b^*(z)G^{(cf)}_{0_{\boldsymbol{k}\sigma}}\left(z,z'\right)G^{(cf)}_{0_{\boldsymbol{k}\sigma}}\left(z',z\right)b^*(z') + b^*(z)G^{(cc)}_{0_{\boldsymbol{k}\sigma}}\left(z,z'\right)G^{(ff)}_{0_{\boldsymbol{k}\sigma}}\left(z',z\right)b(z')\Big] \ . \end{aligned} \quad (5.17)$$

Despite neglecting the build-up of coherence in the incident pulse, including such a term in the equations of motion is of considerable technical challenge and ultimately should not change the results much in this specific problem.

5.2 Non-equilibrium saddle-point equations

Apart from the truncation of the photon interactions, the partition function remains exact and accounts for most of the quantum effects. The partition function is now approximated by the saddle-point approximation

$$Z = \int D\left[b^*, b\right] D\left[\lambda\right] e^{iS_{\text{eff}}\left[b^*, b, \lambda\right]} \approx e^{iS_{\text{eff}}\left[b_0^*, b_0, \lambda_0\right]} \ , \tag{5.18}$$

where

$$\left.\frac{\delta S_{\text{eff}}\left[b^*, b, \lambda\right]}{\delta\big(b^*(z), b(z), \lambda(z)\big)}\right|_{b^*(z)=b_0^*,\, b(z)=b_0,\, \lambda(z)=\lambda_0} = 0 \ . \tag{5.19}$$

In non-equilibrium, the saddle-point condition generates a set of self-consistent equations describing the saddle-points' time evolution. Noting that b_0^* and b are related by complex conjugation, the saddle-point equations read

$$i\partial_t b_0(t) = \lambda_0(t) b_0(t) + i\frac{1}{\mathcal{N}}\frac{\delta \operatorname{tr}\log -i\boldsymbol{G}_0^{-1}}{\delta b_0^*(t)} + g_0^2 \frac{\delta\alpha(t)}{\delta b_0^*(t)} \int_\gamma \mathrm{d}z \, \left[G_a(t,z) + G_a(z,t)\right] \alpha(z) \ , \tag{5.20a}$$

$$1 = \left|b_0(t)\right|^2 + i\frac{1}{\mathcal{N}}\frac{\delta \operatorname{tr}\log -i\boldsymbol{G}_0^{-1}}{\delta \lambda_0(t)} + g_0^2 \frac{\delta\alpha(t)}{\delta \lambda_0(t)} \int_\gamma \mathrm{d}z \, \left[G_a(t,z) + G_a(z,t)\right] \alpha(z) \ . \tag{5.20b}$$

Unlike the saddle-point equation for $b_0(t)$, the saddle-point equation for $\lambda_0(t)$ is not a differential equation but an algebraic one. The set of saddle-point equations is hence a differential-algebraic system of equations, where the equation for $\lambda_0(t)$ *constrains* the possible trajectories of $b_0(t)$. Moreover, since the Hamiltonian is equally defined on both Keldysh contours, the fields follow the same equations of motion on each contour branch. This highlights the *classical* nature of saddle-point equations, where the action on the forward path is cancelled by the one of the backward path [46].

Differentiating through the log term

$$\frac{\delta \operatorname{tr}\log -i\boldsymbol{G}_0^{-1}}{\delta x(t)} = \operatorname{tr} \boldsymbol{G}_0 \frac{\delta \boldsymbol{G}_0^{-1}}{\delta x(t)} = \sum_{\boldsymbol{k}\sigma} \operatorname{tr} \boldsymbol{G}_{0_{\boldsymbol{k}\sigma}}(t,t) \frac{\delta \boldsymbol{G}_{\boldsymbol{k}\sigma}^{-1}(t,t)}{\delta x(t)} \ , \tag{5.21}$$

yields

$$\frac{\delta \operatorname{tr}\log -i\boldsymbol{G}_0^{-1}}{\delta b^*(t)} = -\sum_{\boldsymbol{k}\sigma} V_0 G_{0_{\boldsymbol{k}\sigma}}^{(fc)}(t,t) \ , \qquad \frac{\delta \operatorname{tr}\log -i\boldsymbol{G}_0^{-1}}{\delta \lambda(t)} = -\sum_{\boldsymbol{k}\sigma} G_{0_{\boldsymbol{k}\sigma}}^{(ff)}(t,t) \ . \tag{5.22}$$

Differentiating through the α term, given $\frac{\delta}{\delta x}\boldsymbol{U} = \boldsymbol{U}\frac{\delta}{\delta x}\left(-\boldsymbol{U}^{-1}\right)\boldsymbol{U}$, yields

$$\frac{\delta\alpha(t)}{\delta b^*(t)} = \sum_{\boldsymbol{k}\sigma}\left[G_{0_{\boldsymbol{k}\sigma}}^{(fc)}(t,t) + V_0\left(G_{0_{\boldsymbol{k}\sigma}}^{(cc)}(t,t) G_{0_{\boldsymbol{k}\sigma}}^{(ff)}(t,t) b(t) + G_{0_{\boldsymbol{k}\sigma}}^{(fc)}(t,t) G_{0_{\boldsymbol{k}\sigma}}^{(fc)}(t,t) b^*(t)\right)\right] \ , \tag{5.23a}$$

$$\frac{\delta\alpha(t)}{\delta \lambda(t)} = \sum_{\boldsymbol{k}\sigma}\left[G_{0_{\boldsymbol{k}\sigma}}^{(cf)}(t,t) G_{0_{\boldsymbol{k}\sigma}}^{(ff)}(t,t) b(t) + G_{0_{\boldsymbol{k}\sigma}}^{(ff)}(t,t) G_{0_{\boldsymbol{k}\sigma}}^{(fc)}(t,t) b^*(t)\right] \ . \tag{5.23b}$$

Furthermore the approximation

$$\int_\gamma \mathrm{d}z \, \left[G_a(t,z) + G_a(z,t)\right] \alpha(z) \approx \left[G_a(t,t) + G_a(t,t)\right] \alpha(t) \ , \tag{5.24}$$

is employed, which holds for short pulses, turning the non-equilibrium saddle-point equations (5.20) of motion into a Markovian set of equations.

5.3 Initial conditions

The system is in thermal equilibrium before the pulse's arrival. Due to (5.18) being an effective non-interacting problem and the saddle-points fields 1-point functions, unlike in interacting problems of 2-point functions, the problem can be separated into two disjoint parts. First, solving the saddle-point equations on the Matsubara branch of the Konstantinov-Perel' contour (Figure 1.3). Second, solving the time-dependent saddle-point equations on the Keldysh branches of the Konstantinov-Perel' contour using the thermal solutions as initial conditions. This is also highlighted by the purely Markovian form of the saddle-point set of equations (5.18).

Considering the light pulse to vanish in the Matsubara branch and the fields to be static in imaginary time, the saddle-point equations for the system in thermal equilibrium read

$$0 = \lambda_0 b_0 - \frac{1}{\beta}\frac{1}{\mathcal{N}}\frac{\delta \operatorname{tr}\log \boldsymbol{G}_0^{-1}}{\delta b_0^*} \ , \tag{5.25a}$$

$$1 = |b_0|^2 - \frac{1}{\beta}\frac{1}{\mathcal{N}}\frac{\delta \operatorname{tr}\log \boldsymbol{G}_0^{-1}}{\delta \lambda_0} \ , \tag{5.25b}$$

where $\boldsymbol{G}_0^{-1} = \mathbb{1}\partial_\tau + \boldsymbol{H}$. Since $\boldsymbol{G}_0^{-1}$ is block-diagonal in imaginary time,

$$\operatorname{tr}\log \boldsymbol{G}_0^{-1} = \log\det \boldsymbol{G}_0^{-1} = \sum_{\boldsymbol{k}\sigma} \log\det\left(\mathbb{1}\partial_\tau + \boldsymbol{H}_{\boldsymbol{k}\sigma}\right) = \sum_{\boldsymbol{k}\sigma}\sum_{j} \log\det\left(\partial_\tau + \omega_j\right) \ , \tag{5.26}$$

where $\omega^j_{\boldsymbol{k}\sigma}$ are the eigenvalues of $\boldsymbol{H}_{\boldsymbol{k}\sigma}$. For Grassmann fields, it can be shown [47] that $\det\left(\partial_\tau + \omega^j_{\boldsymbol{k}\sigma}\right) = 1 + \rho(\omega^j_{\boldsymbol{k}\sigma})$, where $\rho(\omega)$ is the Boltzmann factor $e^{-\beta\omega}$. This non-trivial result can be attributed to the boundary terms from constructing the path integral (Section 1.4.1). In the limit of vanishing temperature

$$\lim_{\beta\to\infty} -\frac{1}{\beta}\log\left(1 + e^{-\beta\omega}\right) = \Theta(-\omega)\omega \ , \tag{5.27}$$

the saddle-point equations read

$$0 = \lambda_0 b_0 + \sum_{\boldsymbol{k}\sigma}\sum_{\omega_{\boldsymbol{k}\sigma}<0} \frac{\delta}{\delta b_0^*}\omega^j_{\boldsymbol{k}\sigma} \ , \tag{5.28a}$$

$$1 = |b_0|^2 + \sum_{\boldsymbol{k}\sigma}\sum_{\omega_{\boldsymbol{k}\sigma}<0} \frac{\delta}{\delta \lambda_0}\omega^j_{\boldsymbol{k}\sigma} \ . \tag{5.28b}$$

This unusual form of the saddle-point equations is due to the functional derivatives being taken through a log det instead of the typical tr log, which would result in a set of saddle-point equations dependent on 2-point averages instead of derivatives of eigenvalues of the Hamiltonian. The power hidden in the "unsual" derivatives is that the saddle-point equations can be obtained through automatic differentiation by specifying a single Hamiltonian instead of laborious and error-prone expansions of 2-point averages.

Furthermore, considering a d-dimensions lattice volume $\mathcal{V}$, the sum over the lattice momenta takes the form

$$\lim_{\mathcal{N}\to\infty}\frac{1}{\mathcal{N}}\sum_{\boldsymbol{k}} = \lim_{\mathcal{N}\to\infty}\frac{1}{\mathcal{N}\Delta k}\sum_{\boldsymbol{k}}\Delta k = \lim_{\mathcal{N},\mathcal{V}\to\infty}\frac{\frac{\mathcal{V}}{(2\pi)^d}}{\mathcal{N}}\sum_{\boldsymbol{k}}\Delta k = \frac{\mathcal{V}}{\mathcal{N}}\int\frac{\mathrm{d}\boldsymbol{k}}{(2\pi)^d} = \int_{\mathrm{FBZ}}\frac{\mathrm{d}\boldsymbol{k}}{(2\pi)^d} \ , \tag{5.29}$$

where in the last equality the momenta were rescaled as $a^d\boldsymbol{k} \to \boldsymbol{k}$, where a is the lattice constant and $\frac{\mathcal{V}}{\mathcal{N}a^d} \overset{!}{=} 1$. The last integral is taken over the first Brillouin zone with a unit lattice constant.

5.4 Non-equilibrium saddle-point solutions

Since the fluctuations of the boson field are expected to occur at frequencies associated with ε_0^f [137], the constraint field is shifted as $\lambda_0(t) \to \lambda_0(t) - \varepsilon_0^f$ such that $\lambda_0(t)$ is small and directly corresponds to the Kondo coherence temperature (5.3). Furthermore, the saddle-point approximation freezes out the b field, which encodes the state of an *empty* f-site. As a result, the f-electron degrees of freedom left in the system are of a singly-occupied f-site, and it is expected that f describes similar dynamics to the Kondo Hamiltonian [138], that is, spin-fluctuations at around the Fermi energy. Moreover, due to the approximation (5.24), the system of equations cannot "see" the carrier frequency of the photon pulse and the system is driven only by the intensity of the photon pulse. For these reasons, interpreting Kondo saddle-point results is quite challenging and serves only as a starting point for inspecting the physics of the problem.

In order to solve the non-equilibrium saddle-point equations (5.20), solutions to the non-interacting Green functions of matter fields can be obtained by

$$\boldsymbol{G}_0(t,t') = -i\,\mathbb{T}\left[e^{-i\int_{t_0}^{t}\mathrm{d}\bar{t}\,\boldsymbol{H}(\bar{t})}\right]\left[\Theta_\gamma(t,t')\mathbb{1} + \xi\boldsymbol{n}\right]\bar{\mathbb{T}}\left[e^{+i\int_{t_0}^{t'}\mathrm{d}\bar{t}\,\boldsymbol{H}(\bar{t})}\right] , \tag{5.30}$$

where $\boldsymbol{n}$ is the initial occupation of the fields, at time $t = t_0$. However, at equal times, it suffices to calculate

$$i\partial_t \boldsymbol{G}_0(t,t) = \left[\boldsymbol{H}(t), \boldsymbol{G}_0(t,t)\right] , \tag{5.31}$$

subject to $\boldsymbol{G}_0(t_0,t_0') = \left[\Theta_\gamma(t_0,t_0')\mathbb{1} + \xi\boldsymbol{n}\right]$.

For the following analysis, the system parameters are $\varepsilon_0^f = -0.35$, $g_0 = 0.045$ and $V_0 = 0.3$, in units of the conduction electron hopping v, in a Bethe lattice with infinite connectivity (Section 6.1), for congruency with later results. The set of differential-algebraic equations (5.20) is very unstable and solved via an *implicit Euler* scheme [139], with `rtol` $\sim 10^{-5}$ and `atol` $\sim 10^{-5}$. Until the system is perturbed by the external pulse, the saddle-point fields do not change in time since the system is in thermal equilibrium. Note that *thermal equilibrium* at the level of 1-point fields is a very loose term since the saddle-point fields only capture field averages and hence any n-point correlation that could encode thermal distributions – and fulfil, e.g. fluctuation-dissipation relations (Section 1.3.2) – are not available. Note, however, that thermal distributions can be encoded in the initial occupation of the matter fields $\boldsymbol{G}_0(t_0,t_0)$ but are *fixed* by the initial conditions since their time-evolution is dictated by a *non-interacting* Hamiltonian.

In Figure 5.1, the photon-pulse intensity is kept at a reasonable value $n_a = 1.0$, which is expected to drive the system out of equilibrium, however, without collapsing the Kondo ground-state. Here, it is evident how a larger Kondo coherence temperature, set by the hybridisation strength V_0, generates faster oscillations in the relaxation of λ_0 towards its thermal-equilibrium value. Despite the magnitude of the perturbation to the saddle-point fields being similar whether the pulse is short (Figure 5.1a) or long (Figure 5.1b), two slightly different relaxation scenarios arise. For large Kondo temperatures, under a short pulse, the system is driven out of equilibrium and relaxes back to its ground state with intrinsic fast oscillations. However, for pulses longer than the period of the oscillations, the pulse drive is effectively adiabatic, resulting in a smooth, oscillation-free relaxation. For systems with small Kondo temperatures, both short and long pulses have shorter durations than the oscillation period, resulting in a long and slow oscillatory relaxation to $\lambda_0(t_0)$.

In Figure 5.2, it is revealed that the system responds rather strongly to the pulse's intensity. As expected at the saddle-point level, the recovery of the λ_0 field is modulated by a single frequency, independent of the pulse's intensity. For values of intermediate pulse intensity $n_a \gtrsim 0.5$, the value of $\lambda_0(t)$ changes significantly, and for $n_a = 8.0$, the value of $\lambda_0(t)$ increases

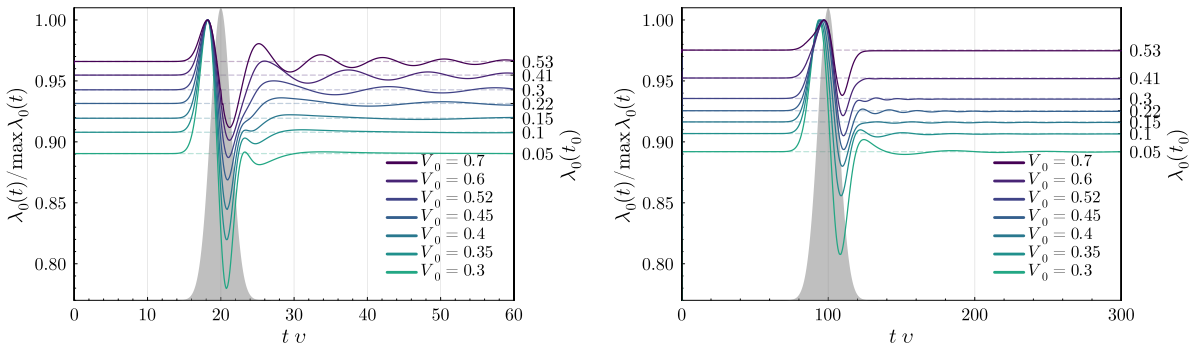

(a) A gaussian pulse with width $\Omega_0 = 0.5$ and pulse maximum at $t\,v = 20$, shaded in grey.

(b) A gaussian pulse with width $\Omega_0 = 0.1$ and pulse maximum at $t\,v = 100$, shaded in grey.

Figure 5.1: Time dependence of $\lambda_0(t)$ for different values of the hybridisation strength V_0, with maximum pulse intensity $n_a = 1$.

to almost double its equilibrium value. Moreover, for long pulses and a large photon-pulse intensity (Figure 5.2b) the system relaxes to a different value of λ_0. This is indeed surprising since the saddle-point equations (5.3) in thermal equilibrium are thought to have a unique solution within the physical regime ($b_0^2 \leq 1$ and $\lambda_0 \sim 0$), which should imply that $\lim_{t\to\infty} \lambda_0(t) = \lambda_0(t_0)$. Despite not appearing to be a numerical problem, as running the differential-equation solver with different tolerances yields similar results, this cannot be ruled out since the tolerances cannot be set to lower values without incurring numerical instabilities. In this regime, however, the Kondo ground state is expected to collapse due to a strong interaction with the photon pulse. Since that is not verified, in the form of no solution for $\lambda_0(t)$, there could be a dynamical breakdown of the saddle-point approximation. That is, for time-dependent problems, the assumption that the fluctuations of the b fields are small most likely does not hold, and further investigation into criteria for the validity of non-equilibrium saddle points is warranted.

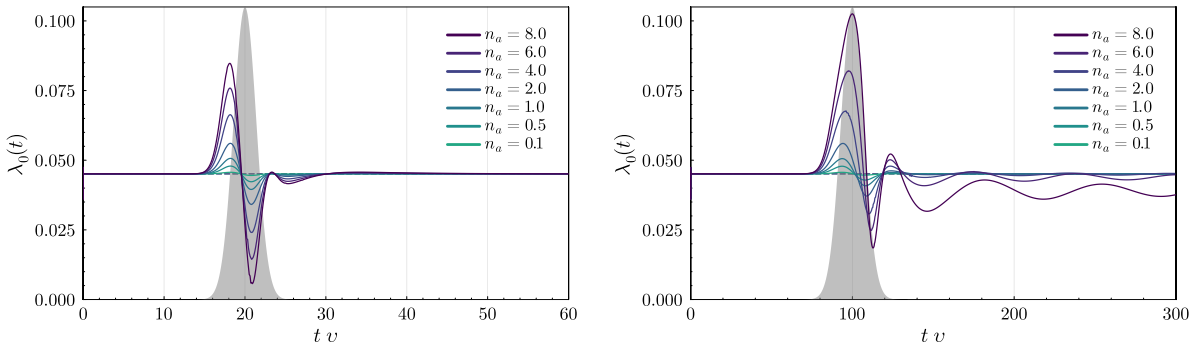

(a) A gaussian pulse with width $\Omega_0 = 0.5$ and pulse maximum at $t\,v = 20$, shaded in grey.

(b) A gaussian pulse with width $\Omega_0 = 0.1$ and pulse maximum at $t\,v = 100$, shaded in grey.

Figure 5.2: Time dependence of $\lambda_0(t)$ for different values of the maximum photon intensity n_a.

Chapter 6

Non-equilibrium interacting theory

The driven-dissipative lattice problem is straightforward: a pulse of electromagnetic radiation arrives, interacts with a heavy-fermion system and propagates away, carrying some information acquired in the interaction. The model is given by the auxiliary-particle light-matter Anderson lattice Hamiltonian (Section 4.2.2)

$$\hat{H} = -\sum_{\langle i,j\rangle} t_{ij}^{c} \hat{c}_{i\sigma}^{\dagger} \hat{c}_{j\sigma} + \sum_{i\sigma} \varepsilon_0^{f} \hat{f}_{i\sigma}^{\dagger} \hat{f}_{i\sigma} + \left[V_0 - i g_0 \left(\hat{a} - \hat{a}^{\dagger} \right) \right] \sum_{i\sigma} \left(\hat{c}_{i\sigma}^{\dagger} \hat{b}_i^{\dagger} \hat{f}_{i\sigma} + \text{h. c.} \right) \tag{6.1}$$

where the hopping of the f electrons was set to zero and $\hat{a}$ is the annihilation operator of the photons of the pulse of radiation that drives the system (Section 4.4). Furthermore, the conduction electrons c are coupled to a fermionic heat bath (Section 4.3.1) at the temperature of the cryostat. Upon tracing out the reservoir, an additional non-interacting effective action term appears

$$iS_{\text{eff}}^{\text{bath}} = \int_{\gamma} \mathrm{d}z\, \mathrm{d}z' \sum_{i\sigma} c_{i\sigma}^{*}(z) \left[\alpha^2 \Delta_c(z, z') \right] c_{i\sigma}(z') \ , \tag{4.22}$$

where the density of states of the bath is taken to be the same as the c electrons'. The term $\alpha^2 \Delta_c(z, z')$ can be regarded as an additional hybridisation function of conduction electrons, containing thermal correlations from the interaction with the heat bath and serving as a dissipative/thermalising channel for the lattice system. The remaining (non-pulse) modes of the electromagnetic field are also treated as a reservoir (Section 4.3.3), for which the interacting action of the system gains the additional term upon tracing out the reservoir's degrees of freedom

$$iS_{\text{eff}}^{\text{bath}} = \int_{\gamma} \mathrm{d}z\ \mathrm{d}z' \sum_{i\sigma} \left[c_{i\sigma}^{*}(z) b_i^{*}(z) f_{i\sigma}(z) + \text{h. c.} \right] i g_0^2 \eta \left[\Pi_a(z, z') + \Pi_a(z', z) \right] \left[c_{i\sigma}^{*}(z') b_i^{*}(z') f_{i\sigma}(z') + \text{h. c.} \right] \ . \tag{4.35}$$

In free space, the coupling with the environment is typically much stronger than with the pulse, as there are many more modes with which the system can couple. This is controlled by the dimensionless parameter $\eta \approx \frac{4\pi}{\Omega_{\text{p}}} \left(1 - \frac{\Omega_{\text{p}}}{4\pi} \right)$, which can be thought as a geometric factor that covers the solid angle of all modes except the pulse's [140]. After the excitation, the system will hence predominantly spontaneously emit into the modes of the environment [141].

In its current form, it is hopeless to solve the problem as it is a lattice of interacting particles, for which not only is there no closed-form solution, brute-forcing perturbative expansions would unearth a diagrammatic hydra, requiring careful summations of non-local interacting terms. For this reason, two *herculean* approximations are yet to be employed: dynamical mean-field theory, which will map the problem to an effective single-site problem and the non-crossing

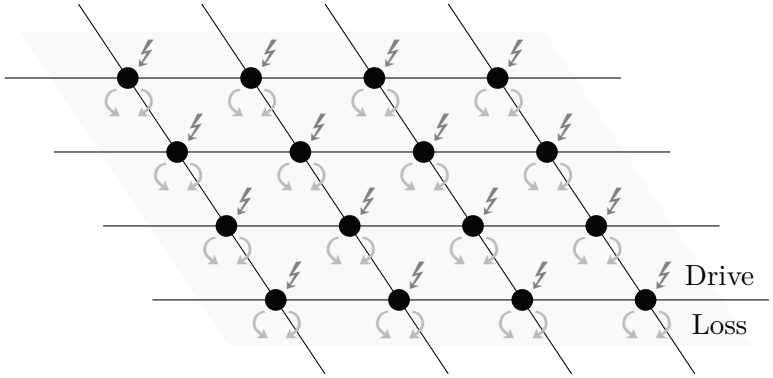

Figure 6.1: Driven-dissipative lattice problem. Figure adapted from [142].

approximation, which will truncate the perturbative expansion of the single-site, or local, problem.

6.1 Dynamical mean-field theory

Dynamical mean-field theory (DMFT) heavily contributed to the understanding of many-body strongly-interacting lattice systems in thermal equilibrium [143], especially Mott physics. In its heart lies the observation [144] that the self-energy of itinerant systems becomes local in the limit of infinite dimensions. This, in turn, allows the mapping [145] of a lattice problem into an Anderson-impurity problem of a single-site embedded in a renormalised conduction electron sea. Even though the renormalised sea neglects *all* quantum spatial fluctuations[1], it retains the full information about quantum temporal fluctuations. Fortuitously, due to the DMFT construction being solely dependent on the real-space properties of n-point functions, the extension of DMFT to non-equilibrium settings [48, 147] is straightforward.

6.1.1 The limit of infinite dimensions

In the limit of infinite dimensions $d \to \infty$, the hopping amplitude t in Hamiltonians such as the Hubbard or Anderson lattice model must be re-scaled such that its competition with local effects such as the Coulomb interaction remains non-trivial, as otherwise, the kinetic energy density would be infinite. The re-scaling

$$t \to \frac{t}{\sqrt{Z}} \,, \tag{6.2}$$

where Z is the lattice connectivity/coordination-number ($Z = 2d$ in a d-dimensional hyper-cubic lattice) has its most important consequence on the scaling of the non-interacting lattice Green function

$$G_{0,ij} \overset{d\to\infty}{=} \mathcal{O}(\sqrt{1/Z}^{d(i,j)}) \,, \tag{6.3}$$

where $d(i,j)$ denotes the distance between sites i and j. The scaling, however, does not imply that the system becomes localised – from a probabilistic perspective, it simply means that for a lattice with infinite connectivity, the probability density of going from the site i to j is infinitesimal – and summing over all lattice sites can counteract the decay. However, it does

[1] Refer to [146] for a review on the inclusion of non-local effects.

suppress all kinds of self-energy processes beyond the local term

$$\Sigma_{ij} \overset{d\to\infty}{=} \delta_{ij}\Sigma_{ii} + \mathcal{O}(\sqrt{1/Z}^{d(i,j)}) \ . \tag{6.4}$$

This can be shown via simple power-counting: any two internal vertices with a lattice index summation scale as $\mathcal{O}(Z^{d(i,j)})$ are connected by at least three Green functions, each scaling as (6.3). Thus, only $i = j$ contributions are non-vanishing. Despite the then *local* nature of the self-energy, without further considerations, it would still be required to sum up all diagrams that could contribute to the local Σ_{ii}. However, via the same power-counting argument, and noting that, due to (6.3) and (6.4), the lattice Green function must also scale as

$$G_{ij} \overset{d\to\infty}{=} \mathcal{O}(\sqrt{1/Z}^{d(i,j)}) \ , \tag{6.5}$$

for self-energies derived through (1.64a), only Γ_2 expansions with local Green functions are non-vanishing

$$\Gamma_2\left[G_{ij}\right] \overset{d\to\infty}{=} \Gamma_2\left[G_{ii}\right] \ . \tag{6.6}$$

Hence, all contributions from (1.68) have the same internal and external lattice indices, and the complex lattice interactions reduce to single-site interactions. This is the critical idea [145] behind DMFT, where a lattice problem is mapped[2] to an effective single-site problem.

6.1.2 The cavity construction

The cavity construction of DMFT is based on a formulation where the Dyson series is written in terms of Green functions where a single site is removed from the lattice. Consider a general lattice Hamiltonian $H(z) = \sum_{ij}\left[h_{ii}(z)\delta_{ij} + h_{ij}(z)\left(1-\delta_{ij}\right)\right]$ composed of non-interacting and interacting local terms $h_{ii}(z) = h_{0,ii}(z) + h_{\mathrm{int},ii}(z)$, diagonal in real-space indices, as well as non-local non-interacting hopping terms $h_{ij}(z)$, with real-space matrix elements t_{ij}. By defining the *single-site* Green function

$$g^{-1}_{ij}(z,z') = \delta_{ij}\delta_\gamma(z,z')\left[i\partial_z - h_{ii}(z)\right] \equiv \delta_{ij}\left\{\delta_\gamma(z,z')\left[i\partial_z - h_{0,ii}(z)\right] - \bar{\Sigma}_{ii}(z,z')\right\} \ , \tag{6.7}$$

which is diagonal in real-space $g_{ij}(z,z') = \delta_{ij}g_{ii}(z,z')$ by definition, the Dyson series for the *lattice* Green function of the system reads

$$G_{ij} = \delta_{ij}g_{ii} + g_{ii}\sum_{k_1\ldots k_n} t_{ik_1}g_{k_2k_2}\,t_{k_2k_3}\,g_{k_3,k_3}\ldots t_{k_nj}\,g_{jj} \ , \tag{6.8}$$

where $\sum_{k_1\ldots k_n} = \sum_{k_1} + \sum_{k_1k_2} + \ldots$. The Dyson series is expressed in terms of the *cavity* Green function $G^{[i]}_{jk}$, which is the lattice Green function with site i removed

$$G_{ij} = \delta_{ij}g_{ii} + \underbrace{\left(\sum_{k_1\ldots k_n} g_{ii}\,t_{ik_1}\,g_{k_1k_1}\,\ldots\,t_{k_ni}\,g_{ii}\right)}_{G_{ii}}\sum_{q_1\neq i} t_{iq_1}\underbrace{\left(\sum_{q_2\ldots q_n\neq i} g_{q_1q_1}\,t_{q_1q_2}\ldots g_{q_nq_n}\right)}_{G^{[i]}_{q_1q_n}}t_{q_nj}\,g_{jj} \ . \tag{6.9}$$

[2] Regarding the treatment of Anderson lattice models, the works [148, 149] preceded the DMFT, ending up with descriptions of single-impurities interacting with an effective conduction sea. However, these overestimated the role of local interactions [150] in comparison with DMFT, which is exact for any lattice problem with on-site interactions in infinite dimensions.

Re-iterating the same procedure on the cavity Green function yields

$$G_{ij} = \delta_{ij} g_{ii} + G_{ii} \underbrace{\sum_{q_1} t_{iq_1} \left(\sum_{q_2 \dots q_n} G^{[i]}_{q_1 q_1} \, t_{q_1 q_2} \, G^{[i,q_1]}_{q_2 q_2} \, t_{q_2 q_3} \, G^{[i,q_1,q_2]}_{q_3 q_3} \dots \right) t_{q_n j}}_{\Delta_{ij}} \, g_{jj} \ , \tag{6.10}$$

for which the *hybridisation* function Δ_{ii} enters the Dyson series for the *local* Green function as

$$G_{ii} = g_{ii} + G_{ii} \, \Delta_{ii} \, g_{ii} \ , \tag{6.11}$$

and hence

$$G^{-1}_{ii}(z, z') \overset{\text{(DMFT)}}{=} \delta_\gamma(z, z') \left[i\partial_z - h_{0,ii}(z) \right] - \bar{\Sigma}_{ii}(z, z') - \Delta_{ii}(z, z') \ , \tag{6.12}$$

the local Green function is formulated as a local problem interacting with a renormalised sea. The hybridisation function Δ_{ii} contains the temporal *correlations* of hopping from the site i to the rest of the lattice and then back to site i at a different time. Within DMFT, the lattice problem is reduced to a set of effective sites which act as independent local scattering centres [148]. The equivalence of the *lattice* Green function

$$\begin{aligned} G^{-1}_{ij}(z, z') &= \delta_\gamma(z, z') \left[\delta_{ij} \left(i\partial_z - h_{0,ii}(z) \right) - t_{ij} \right] - \Sigma_{ij}(z, z') \\ &\overset{\text{(DMFT)}}{=} \delta_\gamma(z, z') \left[\delta_{ij} \left(i\partial_z - h_{0,ii}(z) \right) - t_{ij} \right] - \bar{\Sigma}_{ii}(z, z') \ , \end{aligned} \tag{6.13}$$

commonly expressed in the momentum basis, with (6.11) or (6.12) composes the set of DMFT equations. Note that the self-energies Σ_{ii} and $\bar{\Sigma}_{ii}$ of (6.13) are two very different objects, which are only equivalent if (6.6) holds: whereas the former is the local self-energy of a lattice problem at site i, the latter is the self-energy of a local problem defined at site i (6.7).

6.1.3 Formulation on the Bethe lattice

A Bethe lattice is an infinitely connected (cycle-free) graph (Figure 6.2) with connectivity Z. The density of states (distribution of the momentum energy in crystal lattices) for a Bethe lattice with hopping matrix element t and infinite connectivity

$$\rho_{Z \to \infty}(\varepsilon) = \frac{1}{\pi t} \sqrt{1 - \left(\frac{\varepsilon}{2t} \right)^2} \, \Theta(4t^2 - \varepsilon^2) \ , \tag{6.14}$$

or any $Z > 2$, shares similar features with the ones found in three-dimensional lattices, namely the square-root behaviour near the band edges. Even though specific features of the density of states are of great importance in quantitative calculations, capturing its broader features is generally enough for qualitative analysis, which makes the Bethe lattice a suitable approximation for 3-dimensional systems [151].

A remarkable property of Bethe lattices is their self-similarity, resulting in equivalence between the *cavity* and the *local* Green function. Consider a Bethe lattice with a re-scaled (6.2) hopping matrix element t and the contour-ordered local Green function (6.12) at the site i

$$G^{-1}_{ii}(z, z') = \delta_\gamma(z, z') i\partial_z - \bar{\Sigma}_{ii}(z, z') - Z \frac{t}{\sqrt{Z}} G^{[i]}_{j_\alpha j_\alpha}(z, z') \frac{t}{\sqrt{Z}} \ , \tag{6.15}$$

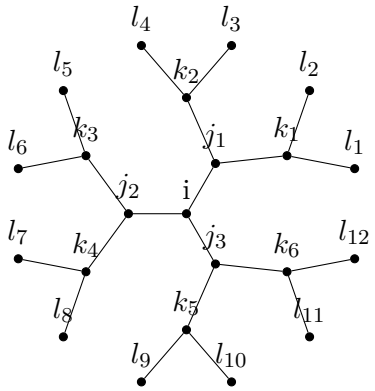

Figure 6.2: A Bethe lattice with connectivity $Z = 3$. For $Z > 2$, the ratio of boundary sites and the total number of sites becomes one when the latter approaches the thermodynamic limit. For this reason, the Bethe lattice is considered to be formed by the sites deep within the Z-Cayley tree, i.e., infinitely far away from the boundary. In this region, all sites become equivalent, with connectivity Z.

Due to being a cycle-free graph, the hybridisation function $\Delta_{ii}(z, z')$ (6.10) simplifies since there is just one possible path of connecting the site i to each of its Z neighbours. The cavity Green function reads

$$G^{[i]\,-1}_{j_\alpha j_\alpha}(z, z') = \delta_\gamma(z, z') i\partial_z - \bar{\Sigma}_{j_\alpha j_\alpha}(z, z') - (Z-1)\,\frac{t}{\sqrt{Z}} G^{[i,j_\alpha]}_{k_\alpha k_\alpha}(z, z')\frac{t}{\sqrt{Z}} \,. \tag{6.16}$$

In the $Z \to \infty$ limit, due to the self-similarity and cycle-free properties of the lattice, $G^{[i]}_{j_\alpha j_\alpha}(z, z') = G^{[i,j_\alpha]}_{k_\alpha k_\alpha}(z, z')$ and (6.16) can be inverted

$$G^{[i]}_{j_\alpha j_\alpha}(z, z') = \frac{y \pm \sqrt{y^2 - 4t^2}}{2t^2} \,, \quad \text{with } y = i\partial_z - \bar{\Sigma}(z, z') \,, \tag{6.17}$$

where $\bar{\Sigma}_{ii}(z, z') = \bar{\Sigma}_{j_\alpha j_\alpha}(z, z') = \bar{\Sigma}(z, z')$. Inserting this result back in (6.15) yields

$$G_{ii}(z, z') = G^{[i]}_{j_\alpha j_\alpha}(z, z') \,, \tag{6.18}$$

and, ultimately, a closed expression for the hybridisation function

$$\Delta_{ii}(z, z') = t\, G_{ii}(z, z')\, t \,, \tag{6.19}$$

thus reducing the DMFT equations to a single-equation for the local problem (6.12).

6.2 The non-crossing approximation

Given that in infinite dimensions the lattice problem is reduced to a local problem (6.6), the lowest-order terms of the 2PI loop expansion (1.68) of (6.1) and (4.35) read

$$\begin{aligned}\Gamma_2 \overset{\text{(DMFT)}}{=} -i \int \mathrm{d}z\, \mathrm{d}z' \sum_\sigma i G_{c_\sigma}(z, z') i G_b(z, z') i G_{f_\sigma}(z', z) \left[V_0^2 + i g_0^2 \Xi_a(z, z')\right] \\ = -i \sum_\sigma \Bigg[\quad V_0 \quad V_0^* \quad + \quad g_0 \quad g_0 \quad \Bigg] \,.\end{aligned} \tag{6.20}$$

The driven-dissipative lattice problem is hence reduced to an effective single-impurity Anderson problem, where the bare coupling vertex V_0^2 becomes dressed by interactions with the electromagnetic field

$$V_0^2 \to V_0^2 + ig_0^2 \Xi_a(z,z') = V_0^2 + ig_0^2 \left[G_a(z,z') + G_a(z',z) + \eta \Pi_a(z,z') + \eta \Pi_a(z',z) \right] \ , \quad (6.21)$$

containing the incident pulse and photonic reservoir dynamics.

Due to the absence of *crossing* lines, the approximation was coined [152] the non-crossing approximation (NCA[3]). This approximation is the simplest term arising from the loop expansion. It involves the maximum number of intermediate states for each order of the perturbation [152] due to the non-crossing lines. Similarly to the dimensionality scaling of DMFT, the NCA becomes exact in the limit of infinite f-level degeneracy N. By rescaling the hybridisation strength, $V \to V/\sqrt{N}$, as the number of crossing lines increases, less intermediate spin states are summed over, and the $\frac{1}{\sqrt{N}^n}$ becomes dominant for an n-order expansion. The NCA qualitatively predicts the emergence of the Kondo effect and some properties of the Kondo resonance [148] and is accurate for high-energy features. However, it does not fully capture all low energy properties and can pathologically diverge at the Fermi energy in the limit of vanishing temperature.

6.2.1 ζ-scaling of contour-ordered self-energies

Due to the projection requirements (Section 2.1), the Green functions are to be calculated in the $\zeta \to 0$ limit of the enlarged Hilbert space. The self-energies are obtained by taking the functional derivative (1.64a) of (6.20)

$$\begin{aligned}
\lim_{\zeta\to 0} \Sigma_{b_\zeta}(z,z') &= \lim_{\zeta\to 0} -i \left[V_0^2 + ig_0^2 \Xi(z,z') \right] \sum_\sigma G_{f_{\zeta,\sigma}}(z,z') G_{c_{\zeta,\sigma}}(z',z) \\
\lim_{\zeta\to 0} \Sigma_{f_{\zeta,\sigma}}(z,z') &= \lim_{\zeta\to 0} +i \left[V_0^2 + ig_0^2 \Xi(z,z') \right] G_{c_{\zeta,\sigma}}(z,z') G_{b_\zeta}(z,z') \\
\lim_{\zeta\to 0} \Sigma_{c_{\zeta,\sigma}}(z,z') &= \lim_{\zeta\to 0} +i \left[V_0^2 + ig_0^2 \Xi(z,z') \right] G_{f_{\zeta,\sigma}}(z,z') G_{b_\zeta}(z',z) \\
\lim_{\zeta\to 0} \Sigma_{a_\zeta}(z,z') &= \lim_{\zeta\to 0} -i\, g_0^2 \sum_\sigma \left\{ G_{c_{\zeta,\sigma}}(z,z') \left[iG_{f_{\zeta,\sigma}}(z',z) G_{b_\zeta}(z,z') \right] + \left((z,z') \to (z',z) \right) \right\} \ .
\end{aligned} \quad (6.22)$$

Due to the self-energies of the conduction electrons c and the pulse-photons a containing auxiliary-particle loops, their components have an *additional* ζ pre-factor in comparison with the auxiliary-particle self-energies

$$\begin{aligned}
\lim_{\zeta\to 0} \Sigma_{b_\zeta}(z,z') &\sim \Theta_\gamma(z,z')\mathcal{O}(1) + \Theta_\gamma(z',z)\mathcal{O}(\zeta) \\
\lim_{\zeta\to 0} \Sigma_{f_{\zeta,\sigma}}(z,z') &\sim \Theta_\gamma(z,z')\mathcal{O}(1) + \Theta_\gamma(z',z)\mathcal{O}(\zeta) \\
\lim_{\zeta\to 0} \Sigma_{c_{\zeta,\sigma}}(z,z') &\sim \mathcal{O}(\zeta) \\
\lim_{\zeta\to 0} \Sigma_{a_\zeta}(z,z') &\sim \mathcal{O}(\zeta) \ .
\end{aligned} \quad (6.23)$$

[3]This technique is also cynically known as the "Never Correct Approximation", due to its shortcomings versus behemoths such as Quantum Monte Carlo. However, as foretold by Philip Anderson [153]

> The better the machinery, the more likely it is to conceal the workings of nature, in the sense that it simply gives you the experimental answer without telling you why the experimental answer is true

the weaknesses of the NCA in *exact* numerics strengthen the fine control and understanding of the underlying physics. And despite requiring a numerical solution due to its non-linear nature, its solutions are well understood, and extensions beyond the NCA have shown good quantitative agreement with exact methods.

Since the conduction and photon-pulse Green functions do not share the same scaling as auxiliary-particle Green functions and scale as $\mathcal{O}(1)$, their self-energies arising from (6.20) are vanishing in the $\zeta \to 0$ limit. Consequently, the c and a Green functions are not *renormalised* by local interactions with the auxiliary particles. Note that for conduction electrons c within DMFT, despite the *local* self-energy vanishing, there are still temporal fluctuations encoded in the hybridisation function $\Delta(z, z')$ that may renormalise $\lim_{\zeta\to 0} G_{c_{\zeta,\sigma}}(z, z')$. For the photon pulse, unlike in a closed cavity where coherent excitations between the electronic system and the electromagnetic field can build up, in free space, the photon pulse propagates past the lattice, interacts with it and flies away. Physically, it is then expected that the pulse photons are not renormalised due to the lack of a DMFT-like procedure, as there is no mechanism to build up temporal correlations. Therefore, the photon-pulse Green function is reduced to the non-interacting Green function (Section 4.4) $\lim_{\zeta\to 0} G_{a_\zeta}(z, z') \to G_{a_0}(z, z')$. Note, however, that this only holds in the $\zeta \to 0$ limit, which is used for calculations. The conduction and the photon-pulse Green functions will be renormalised locally by interactions with *physical* particles. However, these renormalisation effects, encoded in the local self-energies, do not play a role in the $\zeta \to 0$ limit.

6.2.2 Projection of physical observables

Apart from the self-energies generated by the approximation, one must also formulate how to project to the original Hilbert space within the NCA (6.20). The Green function for physical f electrons can be obtained by the projection (2.8) of the auxiliary particles

$$\begin{aligned} G_{f_\sigma}(z, z') \coloneqq -i\langle \mathbb{T}_\gamma \hat{f}^\dagger_\sigma(z)\hat{f}_\sigma(z')\rangle_{\text{physical}} &\equiv \lim_{\zeta\to 0} \frac{-i\langle \mathbb{T}_\gamma \hat{f}^\dagger_\sigma(z)\hat{b}(z)\hat{b}^\dagger(z')\hat{f}_\sigma(z)\rangle_\zeta}{\langle \hat{Q}\rangle_\zeta} \\ &\overset{\text{(NCA)}}{=} \lim_{\zeta\to 0} \frac{iG_{f_{\zeta,\sigma}}(z, z')G_{b_\zeta}(z', z)}{\langle Q\rangle_\zeta} \,. \end{aligned} \tag{6.24}$$

This is because the auxiliary-particle 4-point function factorises at the NCA level

$\langle \mathbb{T}_\gamma \hat{f}^\dagger_\sigma(z)\hat{b}(z)\hat{b}^\dagger(z')\hat{f}_\sigma(z)\rangle_\zeta =$ 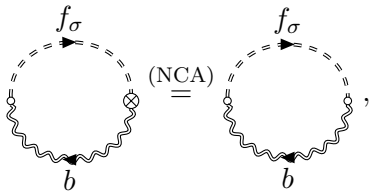

, (6.25)

since the non-trivial *connected* vertex contributions, described by a Bethe-Salpeter equation[4] containing *crossing* diagrams beyond the NCA (6.20)

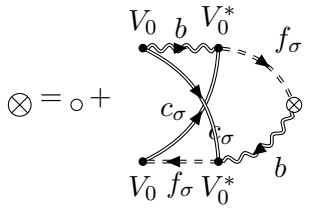

(6.26)

The literature [130] had taken a different route for calculating other physical observables. For an Anderson lattice model without photon coupling, the only other physical observables are related to the conduction electron. In this model, there is an exact known expression for the t-matrix T_{c_σ} of the local conduction electrons

$$G_{c_\sigma}(z,z') = \lim_{\zeta\to 0} G_{c_{\zeta,\sigma}}(z,z') + \left[\left(\lim_{\zeta\to 0} G_{c_{\zeta,\sigma}}\right) * T_{c_\sigma} * \left(\lim_{\zeta\to 0} G_{c_{\zeta,\sigma}}\right)\right](z,z') \;, \tag{6.27}$$

with $T_{c_\sigma} = V_0^2 G_{f_\sigma}$. However, the situation is far more complicated when photons are also coupled to the system, as it is unclear how to obtain a similar t-matrix expression for conduction electron or photon observables compatible with the NCA (6.20). Noting that $\hat{Q}$ does *not* factorise in interacting theories, these observables can be calculated via the *t-matrix* formulation of the Bethe-Salpeter equation and the projection (2.7)

$$\begin{aligned} G_{c_\sigma}(z,z') &\equiv -i \lim_{\zeta\to 0} \frac{\langle \mathbb{T}_\gamma \hat{c}_\sigma^\dagger(z)\hat{c}_\sigma(z')\hat{Q}\rangle_\zeta}{\langle\hat{Q}\rangle_\zeta} \\ &\overset{\text{(NCA)}}{=} \lim_{\zeta\to 0}\left\{ G_{c_{\zeta,\sigma}}(z,z') + \left[G_{c_{\zeta,\sigma}} * \frac{\Sigma_{c_{\zeta,\sigma}}}{\langle\hat{Q}\rangle_\zeta} * G_{c_{\zeta,\sigma}}\right](z,z')\right\} \;. \end{aligned} \tag{6.28}$$

The t-matrix formulation Bethe-Salpeter equation for the 4-point function

$$\langle \mathbb{T}_\gamma \hat{c}^\dagger(z)\hat{c}(z')\hat{Q}\rangle_\zeta = \;\underset{c}{\rightarrow}\; \times \langle\hat{Q}\rangle_\zeta + \;\underset{c\quad c\quad Q}{}\; \;, \tag{6.29}$$

is a function of the Bethe-Salpeter equation for the 4-point *reducible* vertex

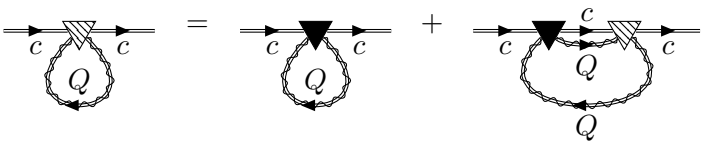

(6.30)

[4]The Bethe-Salpeter equation is the analogue of a Dyson series for a 4-point function X

$$X = X_0 + X_0\,\Gamma_{\text{irreducible}}\,X \;,$$

where X_0 denotes a non-interacting ensemble average of the 4-point function and $\Gamma_{\text{irreducible}}$ is the 4-point *irreducible* vertex of the theory. Similar to a t-matrix series (6.27), the Bethe-Salpeter equation can be related to a *reducible* vertex $\Gamma_{\text{reducible}}$ via

$$X = X_0 + X_0\,\Gamma_{\text{reducible}}\,X_0 \;,$$

where

$$\Gamma_{\text{reducible}} = \Gamma_{\text{irreducible}} + \Gamma_{\text{irreducible}}\,X_0\,\Gamma_{\text{reducible}} \;.$$

For more details, refer to [154–156].

Due to $\langle \hat{Q} \rangle_\zeta \sim \mathcal{O}(\zeta)$, the denominator in (6.28) cancels at most one Q loop. Auxiliary-particle loops also scale as $\mathcal{O}(\zeta)$ and hence, to leading order of the ζ-expansion, the reducible vertex reduces to

$$\lim_{\zeta\to 0}$$ 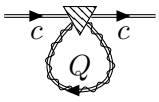

$$= \lim_{\zeta\to 0}$$ 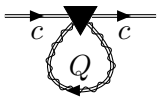

$$\overset{\text{(NCA)}}{=} \lim_{\zeta\to 0}$$ 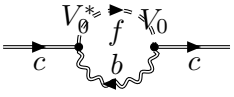

, (6.31)

where the Q insertion is dropped by noting that the resulting interaction, composed of contractions of auxiliary-particle operators with $\hat{Q}$, is equivalent to the same contraction without $\hat{Q}$ (2.8). The projected photon-pulse Green function is similar to (6.28) and reads

$$G_a(z,z') \overset{\text{(NCA)}}{=} \lim_{\zeta\to 0} \left\{ G_{a_\zeta}(z,z') + \left[G_{a_\zeta} * \frac{\Sigma_{a_\zeta}}{\langle \hat{Q} \rangle_\zeta} * G_{a_\zeta} \right](z,z') \right\} . \tag{6.32}$$

6.2.3 Dynamical mean-field theory and auxiliary particles

The usual non-equilibrium DMFT formulation results in a set of integral equations [48]. However, semi-analytic methods such as the NCA make it possible to express these equations in a Kadanoff-Baym form, despite generally not being possible to obtain an expression for the local self-energies – it would be required to find an expression for their projection (Section 6.2.2). For the sake of brevity, it is assumed that the f electrons do not hop, and all Green functions concerning the DMFT are related to the c conduction electrons. Since auxiliary-particle observables are calculated as grand-canonical ensemble averages in the $\zeta \to 0$ limit (Section 2.1), the DMFT-derived observables entering such calculations must be considered in the same limit.

Bethe-lattice DMFT Kadanoff-Baym form In a Bethe lattice, the explicit dependency of the hybridisation can be removed through (6.19). For an effective single-impurity Anderson model defined at some site i, the auxiliary particles are defined *only* at said site. By definition, the hybridisation function $\Delta_{c_{ii\sigma}}$ is traced over all states *not* pertaining to site i, and hence, the canonical ensemble average of $\Delta_{c_{ii\sigma}}$ is the same as the grand-canonical one

$$\lim_{\zeta\to 0} \Delta_{c_{\zeta,ii\sigma}}(z,z') = \Delta_{c_{ii\sigma}}(z,z') . \tag{6.33}$$

Assuming translational symmetry, the site index subscripts can now be dropped. The equation of motion for the local conduction electron grand-canonical Green function that enters the NCA self-energies (6.22) is directly obtained from (6.12)

$$\left[i\partial_z - h_{c_0}(z) \right] \left(\lim_{\zeta\to 0} G_{c_{\zeta,\sigma}}(z,z') \right) = \delta_\gamma(z,z') + \left[t\, G_{c_\sigma}\, t * \left(\lim_{\zeta\to 0} G_{c_{\zeta,\sigma}} \right) \right](z,z') , \tag{6.34}$$

where the self-energy of the local problem is vanishing in the $\zeta \to 0$ limit (6.23). The equation that generates the canonical local conduction electron Green function is obtained by convolving the local Green function (6.28) with the inverse Green function of (6.34), resulting in

$$\left[i\partial_z - h_{c_0}(z) \right] G_{c_\sigma}(z,z') = \delta_\gamma(z,z') + \left[\lim_{\zeta\to 0} \left(\frac{\bar{\Sigma}_{c_{\zeta,\sigma}}}{\langle \hat{Q} \rangle_\zeta} * G_{c_{\zeta,\sigma}} \right) + t\, G_{c_\sigma}\, t * G_{c_\sigma} \right](z,z') . \tag{6.35}$$

General DMFT Kadanoff-Baym form For a general problem in a crystal lattice, consider the equation of motion of the lattice Green function (6.13) in the momentum basis

$$\left[i\partial_z - \varepsilon^c_{\boldsymbol{k}}\right] G_{c_{\boldsymbol{k}\sigma}}(z,z') = \delta_\gamma(z,z') + \left[\bar{\Sigma}_{c_\sigma} * G_{c_{\boldsymbol{k}\sigma}}\right](z,z') \;, \tag{6.36}$$

where tight-binding was assumed $\varepsilon^c_{\boldsymbol{k}} = \sum_{ij} t^c_{ij} e^{i\boldsymbol{k}\cdot(\boldsymbol{R}_i - \boldsymbol{R}_j)}$, $h_{c_0}(z) = 0$. The local Green function is obtained by summing[5] all the $\boldsymbol{k}$-modes

$$G_{c_\sigma}(z,z') = \sum_{\boldsymbol{k}} G_{c_{\boldsymbol{k}\sigma}}(z,z') \;, \tag{6.37}$$

and the equation of motion for the local conduction electron grand-canonical Green function, that enters the NCA self-energies (6.22), is obtained by the Dyson series of the local conduction electron Green function

$$i\partial_z \left(\lim_{\zeta\to 0} G_{c_{\zeta,\sigma}}(z,z')\right) = i\partial_z \left[G_{c_\sigma} * \left(\delta_\gamma - \bar{\Sigma}_{c_\sigma} * \left(\lim_{\zeta\to 0} G_{c_{\zeta,\sigma}}\right)\right)\right](z,z') \;. \tag{6.38}$$

Finally, the self-energy is either obtained by the relation between the t-matrix equation (cf. (6.27)) and the Dyson series

$$\left[T_{c_\sigma} * \left(\lim_{\zeta\to 0} G_{c_{\zeta,\sigma}}\right)\right](z,z') = \left[\bar{\Sigma}_{c_\sigma} * G_{c_\sigma}\right](z,z') \;, \tag{6.39}$$

or, e.g., for $\bar{\Sigma}_{c_\sigma}(z,z') = V_0\, g_{f_\sigma}(z,z')\, V_0$, by differentiating the Dyson series for f electrons

$$i\partial_z \bar{\Sigma}_{c_\sigma}(z,z') = i\partial_z \left[\left(V_0\, G_{f_\sigma}\, V_0\right) * \left(\delta_\gamma - G_{c_\sigma} * \bar{\Sigma}_{c_\sigma}\right)\right](z,z') \;. \tag{6.40}$$

6.3 Numerical procedure

The non-equilibrium driven-dissipative lattice is solved at the level of 2-point functions (Section 1.3), and all presented results were obtained using the same numerical procedure – the only difference being the model parameters. The auxiliary-particle Hamiltonian (6.1) is solved in a Bethe lattice at the level of DMFT (Section 6.1) and NCA (Section 6.2), and is always coupled to fermionic and photonic heat baths (Section 4.3) as well as the photon-pulse mode (Section 4.4). Because of the auxiliary particles, the 2-point functions are calculated in the $\zeta \to 0$ limit (Section 2.1) in both thermal equilibrium and non-equilibrium regimes and only after time-integration are projected to the physical Hilbert space. Solutions of the 2-point functions

[5] Discretising the momenta creates an infrared momentum cut-off, equivalent to considering a finite but periodic lattice. Despite such discretisations being far away from the discretisation found in the real world, where typically one finds 10^{23} cm^{-3} atoms, it is generally good enough to capture most physics, including phase transitions – which are defined only in the thermodynamic limit. However, when summing up plane-wave-like states, such as when calculating local Green functions, one can find an unexpected coherence revival at long times. Consider summing n 1-dimensional plane waves distributed over the first Brillouin zone equidistantly

$$\frac{1}{n} \sum_{k\in\underbrace{[-\pi,\ldots,\pi]}_{n \text{ elements}}} e^{ik\tau} = \cos(\pi\tau) + \cot\left(\frac{\pi\tau}{n-1}\right)\sin(\pi\tau) \;.$$

Due to the finite number of k states, the plane waves become resonant and return to their initial state after a *finite* time, a phenomenon known as the *Poincaré recurrence time*.

in thermal equilibrium are used as initial conditions (Section 1.3.4) for the non-equilibrium time-evolution. Hence, both regimes are described by the same effective action, with the only difference being in the time contour (Section 1.2). This is then reflected in the resulting equations of motion of the 2-point functions and the occupation of the photon pulse, which is taken as constant for all times before the beginning of the time evolution, at time $t = t_0$.

Solutions in thermal equilibrium

Due to the inherent time-translational invariance of systems in thermal equilibrium, the equations of motion of the 2-point functions are transformed into a problem in real-frequency, resulting in a series of self-consistent Dyson equations for auxiliary-particle (Section 2.3.2) and DMFT observables (Section 6.2.3). Due to the fluctuation-dissipation relation (Section 1.3.2), thermal distributions can be enforced for *all* observables. However, to ensure that the heat baths can thermalise the system, the distributions are enforced *only* for bath observables. This safeguard ensures the system can thermalise *numerically*, since too small bath coupling strengths can be washed out due to finite precision and tolerances of the equilibrium and non-equilibrium solvers. Note that the occupation of the fields can be indeterminate when solving self-consistent equations without enforcing distribution functions. For example, the occupation of the electrons is only (indirectly) fixed if the system is coupled to a fermionic heat bat. Otherwise, there is no mechanism to fix the chemical potential (this problem is not present in the time evolution since the occupation number is determined by the system's initial condition and conserved by the dynamics generated by the Hamiltonian). The self-consistent equations are solved via a simple fixed-point iteration scheme, namely Anderson mixing [157], which has shown to be quite robust, fast, and more than adequate for this class of problems. Convergence of the self-consistent equations is achieved when the infinity-norm between the residuals is below the square of the tolerances of the non-equilibrium solver.

Leveraging time and frequency representations in thermal equilibrium Problems of the NCA family in thermal equilibrium are commonly solved on a fixed basis, typically in real-frequency or imaginary time. However, the locality of the Dyson equations in frequency or of the self-energies in time can be maximally exploited with a Fourier transformation between bases. Solutions for the NCA in thermal equilibrium are hence be found by finding the fixed-point of

1. Compute the Dyson equations (2.20) and (2.22) in real frequency,
2. Inverse Fourier transform (1.40) the Green functions to relative time,
3. Compute the self-energies (6.22) in relative time,
4. Fourier transform the self-energies to real frequency.

Finding solutions of NCA equations in real frequency is notoriously difficult [130, 158] due to the sharp features of the functions at low temperatures. Finding solutions in their Fourier dual space is, however, a more stable procedure as the highly-peaked functions in frequency are transformed into slow decaying functions in relative time. Furthermore, relations such as Kramers-Kronig

$$G^R(\tau) = \int \frac{\mathrm{d}\omega}{2\pi} e^{-i\omega\tau} \int \frac{\mathrm{d}\varepsilon}{\pi} \frac{-\operatorname{Im} G^R(\varepsilon)}{\omega - \varepsilon + i\eta} = \Theta(\tau) \int \frac{\mathrm{d}\varepsilon}{2\pi} e^{-i\varepsilon\tau} \left[2i \operatorname{Im} G^R(\varepsilon)\right] \tag{6.41a}$$

$$G^R(\omega) = \int \mathrm{d}\tau\, e^{i\omega\tau} \Theta(\tau) \int \frac{\mathrm{d}\varepsilon}{2\pi} e^{-i\varepsilon\tau} \left[2i \operatorname{Im} G^R(\varepsilon)\right] \ . \tag{6.41b}$$

are elegantly satisfied when changing between bases.

Solutions in non-equilibrium

Instead of using mixed Green functions (Section 1.3.1) to encode vestigial thermal correlations, the thermal equilibrium Green functions are inverse Wigner-Ville FFT'ed[6] (Section 1.3.4), and encode the system in thermal equilibrium for all times *before* the beginning of the time-integration. The resulting initial conditions for the Green functions have an infinite size and must be truncated at some time $t \ll t_0$. The truncation is only validated if the right-hand side of the diagonal equations of motion (Section 3.1) at $t = t_0$ are approximately zero within the numerical tolerances of the non-equilibrium solver. This ensures that despite possibly not retaining the whole information of the system in thermal equilibrium (at the level of 2-point functions), enough information is retained such that the system is integrated as if it had started with the full information. Another possible validation is confirming that the system stays in thermal equilibrium for all times $t > t_0$ when the coupling strength to the driving field is zero. The non-equilibrium equations of motion for auxiliary-particle (Section 2.2.1) and DMFT observables (Section 6.2.3) are Kadanoff-Baym equations (Section 1.4.3) which are solved via an adaptive Kadanoff-Baym solver [32] with tolerances $\texttt{rtol} = 10^{-5}$ and $\texttt{atol} = 10^{-8}$ (Section 3.3).

Why truncation is ruled out Truncation of the integral kernels (Section 3.5.2) found in the Kadanoff-Baym equations of motion (1.67) can greatly reduce the computational effort, however, are not viable for the total integration-time of interest $t_{\max}$. In quantum many-body systems, temperature provides a natural cut-off timescale

$$\tau_{\text{cutoff}} \sim \frac{\hbar}{k_{\text{B}} T} \,, \tag{6.42}$$

beyond which coherent quantum processes are washed out by thermal fluctuations [5]. Given the Kondo lattice coherence developing only when the system is at a temperature below the Kondo coherence temperature (Section 4.1.1) and $t_{\max} \sim \frac{\hbar}{k_{\text{B}} T_K^*}$, any advantageous truncation would spuriously induce high-temperature effects.

Note that for very low temperatures – lower than the smallest intrinsic energy scale of the problem, the Green function components displaying the most extended tails in the relative-time direction (Section 1.3.2) are not spectral components but components related with the occupation of particles. From the viewpoint of thermal equilibrium, this can be understood by the sharp features of the distribution functions at low temperatures in frequency being translated to very long tails in the dual (relative-)time basis.

Projection and Wigner transformation

After time integration, the physical Green functions are computed by projecting the auxiliary particles out (Section 6.2.2). A naive application of the Langreth rules (Section 1.3.3) would be very time-consuming, and these are accelerated by expressing the time-integrals as matrix

[6] For a function $f(x)$ discretised on an equidistant grid $x_i = x_0 + i\Delta x$, for $i \in [0, n-1]$, its discretised Fourier transform (cf. (1.40))

$$\hat{f}(\xi_k) = \frac{\Delta x}{2\pi} e^{-ix_0\xi_k} \,\text{FFT}\left(f(x)\right)_k \,,$$

where $\xi_k = \frac{2\pi}{\Delta x} k/n$, can efficiently be calculated with recourse to a fast Fourier transformation (FFT)

$$\text{FFT}(f(x))_k \coloneqq \sum_{j=0}^{n-1} f(x_j) e^{-2\pi i j k/n} \,.$$

products. The Green functions are then linearly interpolated into an equidistant time grid and Wigner-Ville FFT'ed. The interpolation is the only step in the whole procedure that could introduce significant errors in the data, typically as spurious small oscillatory terms, which are easily identified visually.

6.4 Kondo collapse and revival by pulsed light

Consider (6.1), (4.22) and (4.35) with the parameters of Table 6.1. These parameters constitute the base of the following analyses and are kept constant throughout unless explicitly denoted. A large value of the inverse temperature β and the f-electron ground-state energy ε_0^f and hybridisation V_0 are associated with the Kondo regime ($J_K \sim 0.5$). Due to the DMFT freezing out all spatial fluctuations, the system is in a heavy Fermi liquid phase, very far away from magnetic instabilities brought by criticality (Figure 4.1). The system is dipole-coupled to the electromagnetic field with coupling strength g_0. The coupling to the electromagnetic-field vacuum modes is η times stronger than the coupling to the external pulse, where Λ is a soft cut-off of the coupling to high-energy vacuum modes. The coupling strengths to the fermionic and photonic reservoirs, α and $\sqrt{\eta}g_0$, respectively, are small enough that the system's qualitative properties remain unchanged. For example, too large α can change the quasiparticles' lifetime and wash out the Kondo lattice coherence of the conduction electrons, and too large $\sqrt{\eta}g_0$ can induce a significant Lamb shift of the single-particle peak at ε_0^f. However, α is chosen sufficiently large for thermalisation times – associated with the timescale $\sim \frac{\pi\upsilon}{\alpha^2}$ – to be accessible through numerical integration, where υ is the Bethe lattice hopping. The external pulse has a small central frequency ω_0 and frequency-bandwidth Ω_0, both associated with the THz regime, and a maximum photon intensity of $\bar{n}_a$. The effective coupling strength of the external pulse to matter, $g_0^2\bar{n}_a$, is small since the non-equilibrium dynamics are intended not to be very violent.

Anderson model	Fermionic reservoir	Electromagnetic field	External pulse
$\varepsilon_0^f/\upsilon = -0.35 \quad V_0/\upsilon = 0.3$	$\beta\upsilon = 150 \quad \alpha/\upsilon = 0.04$	$g_0/\upsilon = 0.04 \quad \eta = 10 \quad \Lambda/\upsilon = 0.25$	$\omega_0/\upsilon = 0.001 \quad \Omega_0/\upsilon = 0.06 \quad \bar{n}_a = 10$

Table 6.1: Parameters in units of the Bethe lattice hopping υ.

To understand the collapse[7] and revival of the Kondo coherence, one must first know how to identify it. In a system with many f sites, below the Kondo coherence temperature T_K^*, the f electrons which scatter into the conduction band and later scatter back into the same site have partaken in the build-up of Kondo resonances (Section 4.1.1) in other lattice sites. Such excitations can be detected by an enhancement of the local density-of-states of the *cavity* Green function (6.34) near the Fermi energy, which influences the Kondo temperature (4.6) exponentially[8]. Similarly, the *local* Green function of the f electrons (6.24) exhibits a Kondo

[7]There had been some previous attempts [159, 160] at observing some sort of Kondo collapse on a Kondo lattice driven by a strong pulse of radiation. However, the studies suffered several limitations. First, the Kondo lattice model contains no charge fluctuations, which, according to the investigations of Chapter 5, appear critical in non-equilibrium dynamics. Second, long-time dynamics could not be investigated since only short-time evolutions could be resolved. Additionally, only large pulse frequencies could be considered, which are too energetic and strongly excite the system, which ends up at a very high temperature due to being a closed formulation. Lastly, the light was treated classically and hence could not induce intra-band transitions and spontaneous emission into experimentally-accessibly electromagnetic field modes.

[8]Within DMFT, (4.6) could be used to estimate the Kondo coherence temperature, as the problem is reduced to a single-site problem – with the non-interacting density of states entering the equation being replaced the density of states of the *cavity* Green function (6.34). However, this is a crude approximation since the cavity density of states is energy- and temperature-dependent and all *spatial* fluctuations were neglected. Within this approximation, the Kondo lattice-coherence temperature T_K^* is expected to be *higher* than the single-impurity

resonance at the Fermi energy and the *local* Green function of the c electrons (6.35) a dip, as conduction electrons are removed from the Fermi surface as they hybridise with the f electrons.

6.4.1 Time-resolved collapse and revival of the heavy quasiparticles

The time evolution of the spectral function of the f electrons in Figure 6.3 shows in great detail how a THz light pulse induces strong non-equilibrium dynamics and leads to the collapse of Kondo coherence. At first, the THz pulse has not interacted with the system, which remains in thermal equilibrium at a low temperature, as evidenced by the sharp Kondo peak and thermal distribution function. However, as the THz pulse starts interacting with the system, the Kondo peak is immediately affected as the pulse excites the low-energy states near zero frequency. As the intensity of the external THz pulse grows, two main physical mechanisms of action of the pulse on the electronic system can be identified: enhanced hybridisation and correlation decoherence.

Enhanced hybridisation Without coupling to the electromagnetic fields, the width Δ of the single-particle peak around ε_0^f is given by $\Delta \sim \pi V_0^2 \rho_0^c(\varepsilon_F)$. The dressing of the bare hybridisation vertex (6.21) by the coupling to the electromagnetic field can considerably change Δ near the THz pulse maximum $\Delta \sim \pi \left(V_0^2 + g_0^2 \bar{n}_a\right) \rho_0^c(\varepsilon_F)$, where the last term is obtained by convolving a sharp THz spectral function with ρ_0^c. The enhanced hybridisation shifts the problem from the Kondo regime to a mixed-valence regime, where the average occupation of the f level can drop significantly, highlighting the importance of including charge fluctuations (encoded in the dynamics of the b auxiliary particle) in the dynamics. Apart from the direct effect on the spectral content of the fields, a larger hybridisation strength results in a larger Kondo temperature and hence a broader and smaller Kondo peak. The coupling to the electromagnetic-field reservoir has a negligible effect on the single-particle peak's frequency (Lamb) shift and width.

Correlation decoherence Despite DMFT signifying the presence of an *infinite* reservoir of particles, its temperature is only fixed at all times before t_0. At any time $T > t_0$, the temperature is an indefinite quantity and is only possible to infer through a generalisation of the fluctuation-dissipation relation (Section 1.3.2). While driven out of equilibrium by the incident THz pulse, there is a light-mediated energy transfer from the valence band to the conduction band – interband heating, creating hot charge carriers. As possible to infer from the distributions functions in Figure 6.3, the THz pulse induces a non-thermal hot distribution function which washes out the Kondo coherence that was present in the system before the interaction with the THz pulse. This process induces decoherence of the Kondo correlations and fundamentally differs from the heating encountered experimentally when using long light pulses. A pulse interacting for a long time with a material excites all the sub-bands and phononic degrees of freedom, resulting in a heat-up of the reservoirs, which also provides correlation decoherence through thermal fluctuations. However, the correlation decoherence described here is simply an extreme deviation of the microscopic system from a thermal state, as high-energy states from the THz pulse mix with the low-energy thermal electronic states.

Without a coupling to a reservoir, the system would reach a stationary-state effective temperature far above the initial temperature. By coupling to a reservoir at the same temperature as the system at initial times, the system first reaches a quasi-equilibrium state at some high

T_K due to the spectral enhancement of the cavity Green function at the Fermi energy, in agreement with several compounds [161]

temperature[9] due to the coherence time of conduction electrons being $\sim v^{-1}$, before a proper transfer of the excess energy to the environment, with a rate entirely determined by the coupling to the reservoir(s). This can be evidenced by the fast recovery of the single-particle peak at ε_0^f and a Fermi-Dirac-like distribution well before the Kondo peak is reformed, which takes longer because of two reasons. One, the effective temperature must drop below the Kondo temperature – through interband cooling, with electronic transitions from the conduction to the valence band – for the Kondo effect to become dominant. And second, because Kondo coherence – associated with a sharp resonance in frequency around the Fermi energy – takes a long time to build up because of the intrinsic low-energy effects associated with Kondo physics.

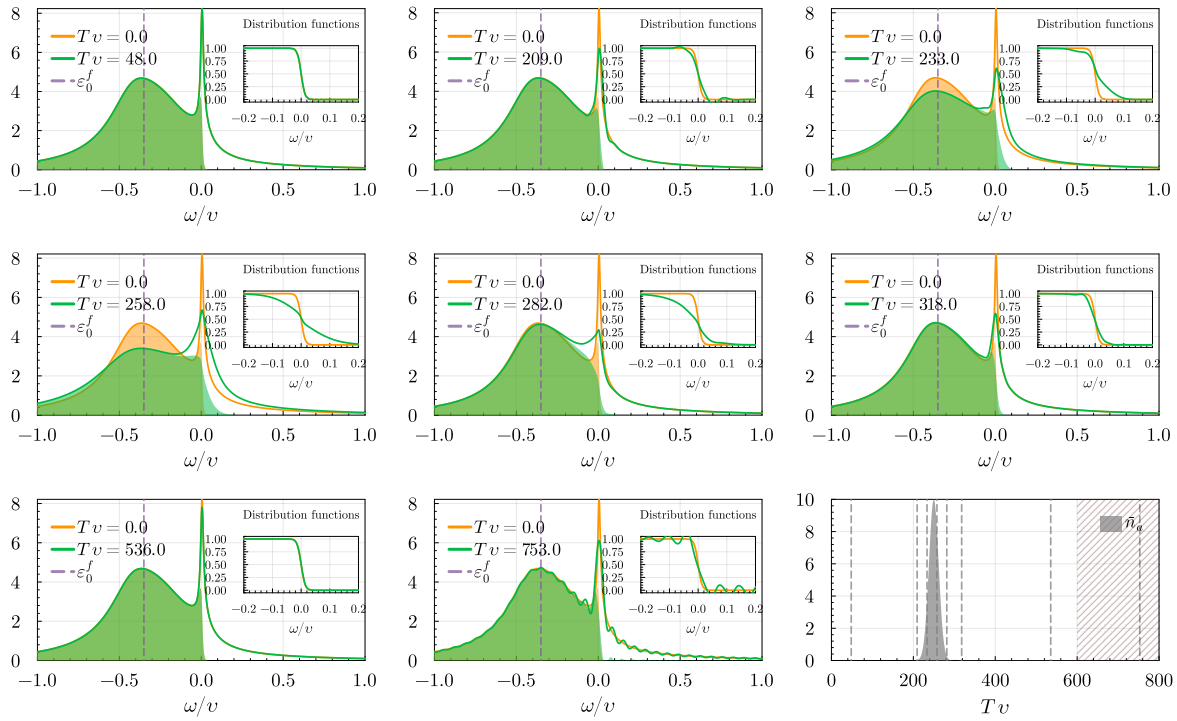

Figure 6.3: Time evolution of the spectral $-2\,\mathrm{Im}\,G^R_{f_\sigma}(T,\omega)_\mathrm{W}$ and distribution (1.31) (insets) function components of the local f Green function upon drive by a Gaussian THz pulse. The bottom right plot denotes the intensity profile of the THz pulse, and the vertical lines show the time at which the different plots take place. The second to last plot exhibits oscillations due to not existing enough points in the τ-direction (1.25) at late centre-of-mass times T to resolve the sharp spectral features, a region shaded in red. A similar effect is not seen in the first plot because the Green functions are defined for times $T < 0$, and there are enough points to resolve the Green functions properly.

Time-resolved view of the heavy quasiparticles

A solution to the lattice Green function (6.36) for all momenta is necessary to obtain a time-resolved view of the heavy quasiparticles. However, the DMFT problem was formulated in a Bethe lattice to avoid the elevated computational cost of separately resolving each $\boldsymbol{k}$-point.

[9]The behaviour of the distribution function around zero frequency is in agreement with a hot temperature, but is in itself a weak heuristic, as the definition of temperature or thermal distribution can only re-emerge at long times, after thermalisation.

Since the data is interpreted in a Wigner-Ville transformed basis, which already has some caveats in strong non-equilibrium regimes (Section 1.3.2), to add insult to injury, the lattice Green functions are calculated as

$$G^{-1}_{c_{\boldsymbol{k}\sigma}}(T,\omega)_{\tilde{\mathrm{W}}} \overset{!}{=} \left[\omega - \varepsilon^{c}_{\boldsymbol{k}} - \Sigma_{c_\sigma}(T,\omega)_{\tilde{\mathrm{W}}}\right], \tag{6.43}$$

where the local self-energy of conduction electrons is calculated through

$$T_{c_\sigma}(T,\omega)_{\tilde{\mathrm{W}}}\left(\lim_{\zeta\to 0} G_{c_{\zeta,\sigma}}(T,\omega)_{\tilde{\mathrm{W}}}\right) \overset{!}{=} \Sigma_{c_\sigma}(T,\omega)_{\tilde{\mathrm{W}}} G_{c_\sigma}(T,\omega)_{\tilde{\mathrm{W}}} \,. \tag{6.44}$$

The self-energy $\Sigma_{c_\sigma}(T,\omega)_{\tilde{\mathrm{W}}}$ is, of course, not the *true* local self-energy of the system (6.39). However, for qualitative assessment, it should contain the most important features, especially since when Kondo coherence collapses, the system loses its low-energy features and the timescales of the pulse drive are much slower than the intrinsic timescales of the system (Section 1.3.2). Away from transient effects, it is expected[10] that the self-energy renormalises the momenta close to the Fermi energy strongly. For vanishing light-matter coupling, the lattice Green function of f electrons can be calculated as

$$G_{f_{\boldsymbol{k}\sigma}}(T,\omega)_{\tilde{\mathrm{W}}} \overset{!}{=} \frac{1}{V_0^2}\left[\Sigma_{c_\sigma}(T,\omega)_{\tilde{\mathrm{W}}} + \Sigma_{c_\sigma}(T,\omega)_{\tilde{\mathrm{W}}} G_{c_{\boldsymbol{k}\sigma}}(T,\omega)_{\tilde{\mathrm{W}}} \Sigma_{c_\sigma}(T,\omega)_{\tilde{\mathrm{W}}}\right] \,. \tag{6.45}$$

In Figure 6.4 the collapse and revival of the heavy quasiparticles can be seen in detail. Before the interaction of the THz pulse, the system exhibits heavy quasiparticles, identified by the flat and thin spectral intensity near zero frequency ω for most values of κ. Despite NCA + DMFT being unable to capture a Kondo insulating phase ($J_K \gtrsim 1.0$) without introducing doubly-occupied f-level states, the heavy quasiparticles form a many-body indirect gap near $\omega = 0$, bordered by two peaks of width $\sim T_K^*$. Furthermore, a single-particle hybridisation gap near $\omega = \varepsilon_0^f$, also arising from the hybridisation of f and c particles, is also visible. The THz pulse induces a momentary mixed-valence regime and subsequent loss of the large effective electron mass as the hybridisation and indirect gap smear out entirely, and the latter shifts towards the Fermi energy. This signals the collapse of the heavy quasiparticles as Kondo coherence melts, the large Fermi surface shrinks and the system is characterised by a higher metallic character. Upon the disappearance of the THz pulse, the system starts its thermalisation process. The single-particle hybridisation gap recovers first, as it is a single-particle effect with an associated fast timescale $\sim V_0^2 \rho_c^0(\varepsilon_F)$. Only long after the interaction of the THz pulse is the Kondo effect recovered, and the heavy quasiparticles reformed again around the edges of the indirect gap.

[10] Consider the rotation $G_{c_{\boldsymbol{k}\sigma}}(t,t') = e^{-i\varepsilon^c_{\boldsymbol{k}}(t-t')}\bar{G}_{c_{\boldsymbol{k}\sigma}}(t,t')$, where (6.36) reads

$$i\partial_t \bar{G}_{c_{\boldsymbol{k}\sigma}}(t,t') = \int_\gamma \mathrm{d}\bar{t}\, \Sigma_{c_\sigma}(t,\bar{t}) e^{+i\varepsilon^c_{\boldsymbol{k}}(t-\bar{t})} \bar{G}_{c_{\boldsymbol{k}\sigma}}(\bar{t},t') \,.$$

The Bogolyubov principle states that the temporal correlations in a system decay within a period with characteristic time Λ. This is translated directly into 2-point functions such as $G_{c_{\boldsymbol{k}\sigma}}(t,t')$ or self-energies $\Sigma_{c_\sigma}(t,t')$, which should have negligible values for outside the strip $|t-t'| \lesssim \Lambda$. Hence,

$$i\partial_t \bar{G}_{c_{\boldsymbol{k}}}(t,t') \approx \int_\gamma \mathrm{d}\bar{t}\, \bar{\Sigma}(t,\bar{t}) e^{-\frac{(t-\bar{t})^2}{2\Lambda^2}} e^{+i\varepsilon_{\boldsymbol{k}}(t-\bar{t})} \bar{G}_{\boldsymbol{k}}(\bar{t},t') \approx \bar{\Sigma}(t,t)\bar{G}_{c_{\boldsymbol{k}}}(t',t') e^{-\frac{1}{2}\varepsilon^2_{\boldsymbol{k}}\Lambda^2}\sqrt{2\pi\Lambda^2}$$

Given that $\Lambda \sim \frac{\hbar}{k_\mathrm{B} T_K^*} \gg 1$, the conduction electrons that get renormalised are the ones with small kinetic energy, namely the ones with energy close to $k_\mathrm{B} T_K^*$.

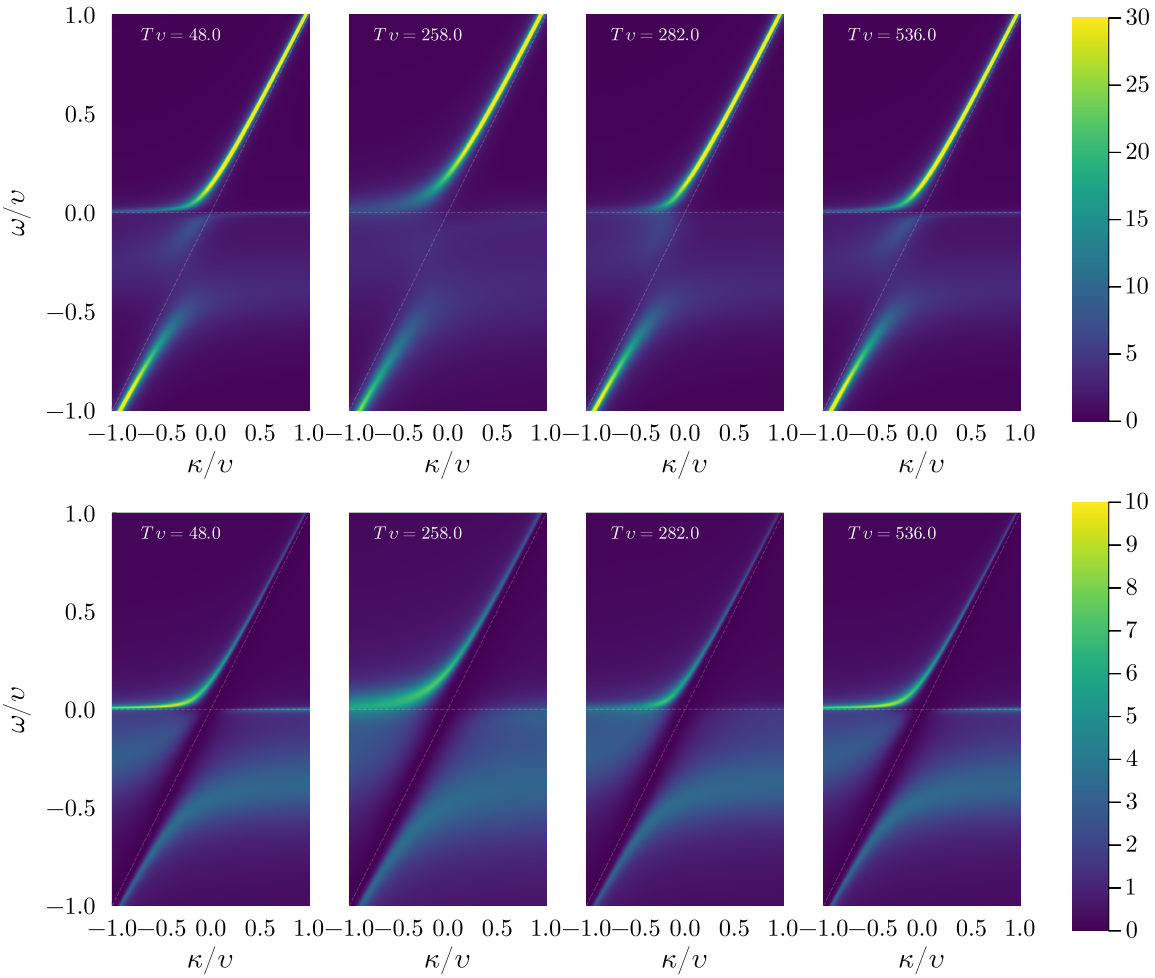

Figure 6.4: Time-resolved collapse and revival of the heavy quasiparticles. In the top panel, the spectral function of the charge carriers $-2\,\mathrm{Im}\left[G_{c_{\boldsymbol{k}}}(T,\omega)_{\tilde{\mathrm{W}}} + G_{f_{\boldsymbol{k}}}(T,\omega)_{\tilde{\mathrm{W}}}\right]$, and in the bottom panel the spectral function of the f electrons $-2\,\mathrm{Im}\,G_{f_{\boldsymbol{k}}}(T,\omega)_{\tilde{\mathrm{W}}}$, where $\varepsilon^{\mathcal{C}}_{\boldsymbol{k}} \coloneqq \kappa$, are plotted for different centre-of-mass times, denoted in Figure 6.3.

6.4.2 Photon re-emission

In a reflection geometry, such as in the THz experimental setting of [12], an incident THz pulse arrives, interacts with the system, is reflected, and propagates away, carrying some information about the system (Figure 4.2). There is an *instantaneous* reflection originating from stimulated intra-band excitations within the conduction bands, which leave the heavy quasiparticles intact – and are even decoupled from the model (6.1), which only contains the conduction electrons which interact with the f electrons. Additionally, a *delayed* – echo-like – reflection response is observed, originating from inter-band transitions between hybridised conduction and f electrons and understood as stemming from the recovery of the Kondo singlets after their destruction by the THz pulse.

Establishing a faithful correspondence between theory and such experiments is somewhat complicated: unlike the latter, which can only measure reflection and not incidence intensity, the former can only compute local temporal *distortions* of the incident intensity. Geometrical and dispersive aspects of the THz pulse cannot be fully considered given the local description

of light interacting with matter, namely the light-matter Hamiltonian (6.1) and the associated equations of motion of the non-interacting part of pulse (4.44). Nonetheless, despite resulting in a small distortion due to the smallness of g_0, the intensity of the renormalised incident pulse shows interesting dependence on the system parameters, corroborating the experimental observations. For short times $T \ll 1/g_0$ upon the pulse interacting with the system, the incident pulse mode is not distorted, as spontaneous emission either into the pulse mode or into the environment is negligible. At later times, emission by one-photon transitions drives the system back to its original state through radiative recombination, renormalising the temporal mode of the incident pulse, which develops a macroscopic *delayed* secondary pulse. This long sought-after experimental signature encodes and carries information about the ground state and possibly physics hidden within the underlying system (Chapter 4). The dependence of the delayed pulse on several system parameters strongly indicates its relation with low-energy Kondo physics, decisively explaining in great part the time-resolved THz experimental observations of [12].

In the following analyses, the renormalised photon intensity – obtained through the lesser component of (6.32) – is shifted by its background value $G_a^<(T,\tau)_{\mathrm{W}} \to G_a^<(T,\tau=0)_{\mathrm{W}} - \lim_{\Gamma\to\infty} G_a^<(\Gamma,\tau=0)_{\mathrm{W}}$. Since the electronic system is always coupled to the electromagnetic field, the renormalisation of the latter always results in a finite but experimentally unmeasurable background photon number. Similarly, the normalised intensity of the delayed pulse of the inset plots is obtained via $-\operatorname{Im}\frac{G_a^<(T,\tau=0)_{\mathrm{W}}}{\lim_{\Gamma\to\infty} G_a^<(\Gamma,\tau=0)_{\mathrm{W}}} - 1$, and measures how much brighter the delayed pulse is in comparison with the background noise. The incident pulse intensity $-\operatorname{Im} G_{a_0}^<(T,\tau=0)_{\mathrm{W}}$, shaded in grey, is visible in all plots, but due to the large zoom of the vertical axis, its Gaussian profile (4.41) is not visible. Finally, a red-shaded area indicates where some results may become inaccurate due to the lack of points in the τ direction to resolve sharp spectral features.

Delayed pulse vs pulse intensity (Figure 6.5) Experiments with light interacting with matter are typically performed in two different regimes: the low-fluence regime, where the system is perturbed as gently as possible to minimise heating effects and the high-fluence regime, where the system is perturbed as strongly as required, possibly non-perturbatively, to induce phase transitions or create non-thermally-accessible metastable states [162]. Experiments such as [12] are within the former regime, with a low photon flux hitting the heavy-fermion compounds. However, there is a long-standing question on whether the observed experimental delayed pulse is not related to Kondo physics but instead to superradiant decay. The archetype example of superradiance is when a dense ensemble of incoherently excited two-level systems lock their dipoles in phase and develop a macroscopic dipole proportional to the number of inverted atoms N [163]. The dipole decays at an accelerated rate, emitting a delayed pulse with intensity $I(t) \approx \gamma \left(\frac{N}{2}\right)^2 \operatorname{sech}^2\left[\gamma\frac{N}{2}(t-t_{\mathrm{D}})\right]$, for some decay rate γ and delay time t_{D} [164]. The intensity of the emitted light is characterised by being proportional to the *square* of the number of excited atoms N and its duration inversely proportional to N. These characteristics are in strong opposition with the *linear* dependence of the delayed pulse on the intensity of the incident pulse, controlled by $\bar{n}_a$. This parameter should also increase the number of excited electrons in the system, even though a heavy-fermion lattice is undoubtedly more complicated than an ensemble of weakly interacting two-level systems. An estimate of the *fraction* of excited atoms is given by

$$N \approx \max_t \left[G_{c_\sigma}^>(t,t) + G_{f_\sigma}^>(t,t)\right] \ , \tag{6.46}$$

which measures the charge carriers' maximum depopulation (or hole number) upon interaction with the external pulse. Here, the delayed pulse's intensity also depends linearly on N. Finally,

the duration of the delayed pulse does not depend on the inverse of N, another definitive indication that the obtained delayed pulse is fundamentally different from superradiant emission.

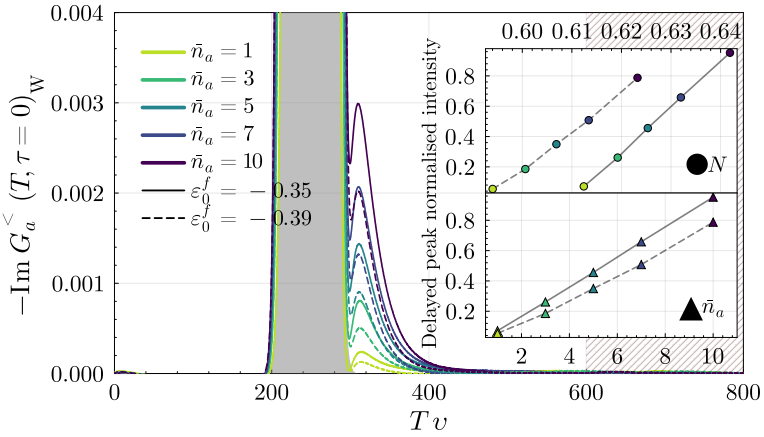

Figure 6.5: Time trace of the renormalised photon pulse as a function of the incident pulse's maximum intensity $\bar{n}_a$ and f electron energy ε_f^0. The insets show a linear dependence of the maximum intensity of the delayed pulse on the incidence intensity $\bar{n}_a$ and on the fraction of excited electrons N.

Delayed pulse vs pulse frequency (Figure 6.6) Another key dependence of the delayed pulse is on the incident pulse central frequency ω_0. For a large frequency ω_0, the pulse distortion appears to be a longer – or more extended – exponential-like decay rather than a secondary pulse. Upon lowering ω_0 to a physical regime[11] more closely related to the experimental settings [12], the delayed pulse, with a slightly longer decay time, is recovered. The reason why this happens is encoded in the inset of Figure 6.6, which shows how the retarded component of the t-matrix T_a of the photon pulse looks like in thermal equilibrium (or, equivalently for the purpose of this analysis, when Kondo coherence is fully developed). The t-matrix T_a comprises a fast decaying rapid oscillation (related to the broad single-particle peak centred at ε_f^0) and a slow decaying slow oscillation (associated with the sharp Kondo peak centred almost at 0). The renormalisation of the photon pulse, obtained through time convolutions (6.32), results in vastly different outcomes depending on the oscillations of the photon Green functions. For a large central frequency ω_0, the slow decaying part of T_a roughly averages to zero and hence temporal information about Kondo coherence is lost, and only single-particle information is retained. Conversely, for a small ω_0, the slow decaying part of T_a is retained, resulting in an echo-like distortion of the incident temporal pulse mode. This shows how Kondo coherence is required for a secondary echo-like pulse to form, as opposed to an exponential-like decay, characteristic of single-particle relaxations.

Delayed pulse vs bath temperature (Figure 6.7) Ultimately, the delayed pulse is strongly temperature dependent, vanishing at high temperatures and growing as the bath temperature is lowered – both in qualitative agreement with experiments [12]. At high temperatures, the

[11] Despite being possible to generate results for larger ω_0, the simplifying assumptions on the dipole matrix element (Section 4.2.2), such as zero-momentum transfer on light-mediated electronic transitions, become unfounded. For a conduction bandwidth $D \sim 4v \sim 4$ eV, a photon frequency of $\omega_0 = 0.1v \sim 25$ THz is already roughly 100 times larger than in the experiments.

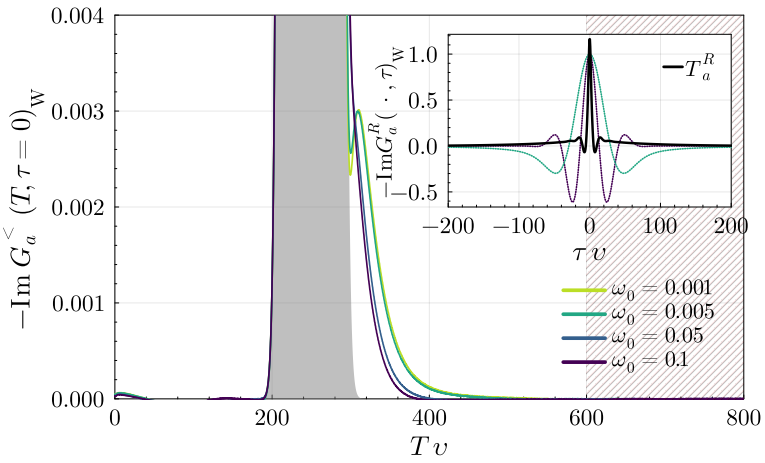

Figure 6.6: Time trace of the renormalised photon pulse as a function of the incident pulse's central frequency ω_0. The inset shows the time trace in the relative time τ direction of the retarded components of the incident photon's Green functions and (rescaled) t-matrix T_a in thermal equilibrium, hence centre-of-mass time T independent.

electronic system is described by single-particle physics, with the system being composed of localised f particles interacting weakly with delocalised conduction electrons. Here, there are no heavy quasiparticles since thermal fluctuations wash out many-body quantum effects, and light-induced effects have a negligible impact on the system. However, as the bath temperature approaches and is set below T_K^*, there is a pronounced renormalisation of the incident pulse, resulting in a secondary, *delayed* pulse. The amplification of the delayed pulse's intensity with the lowering of the bath temperature is another indication of its relation with low-energy physics, appearing to plateau as $\beta \to \infty$, as the Kondo effect saturates (much lower temperatures cannot be reached numerically within DMFT + NCA and these Anderson lattice model parameters).

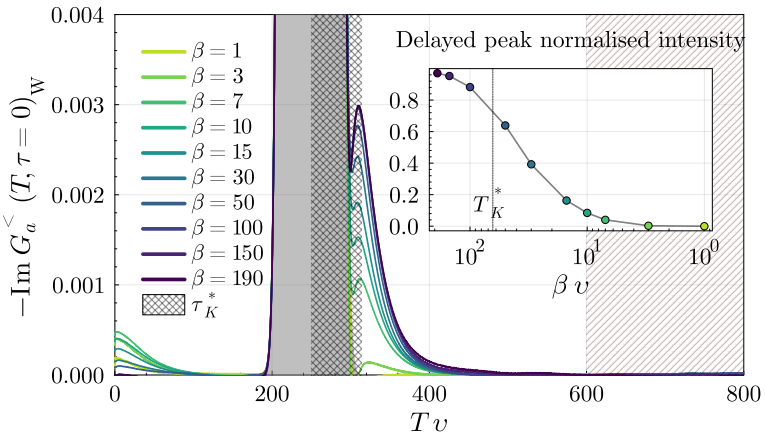

Figure 6.7: Time trace of the renormalised photon pulse as a function of the bath temperature β. The inset shows a logarithmic dependence of the maximum intensity of the delayed pulse on β. The Kondo timescale τ_K^* is defined as $\tau_K^* = \frac{\hbar}{k_\mathrm{B} T_K^*}$.

Delayed pulse vs bath coupling (Figure 6.8) A larger bath coupling strength α induces more decoherence in conduction electrons, which washes out some of the Kondo coherence, directly influencing the delayed pulse, which becomes less intense and with a shorter tail. Furthermore, α sets the timescale for thermalisation, controlling how long it takes for the system to build back its in-equilibrium coherence, estimated by the Kondo peak relative height. A system with a lower T_K^*, related to a larger ε_0^f, is more stable to the interaction with the incident pulse, noting a considerably weaker collapse of the Kondo peak height and a less intense delayed pulse. This indicates that the delayed pulse is related not only to the Kondo coherence but also to how much of it is destroyed. Despite the height roughly measuring how much Kondo coherence there is, it never vanishes entirely (cf. Figure 6.3) as it is just the value of the spectral function at $\omega = 0$ and is not an isolated measurement of the spectral weight of Kondo quasiparticles.

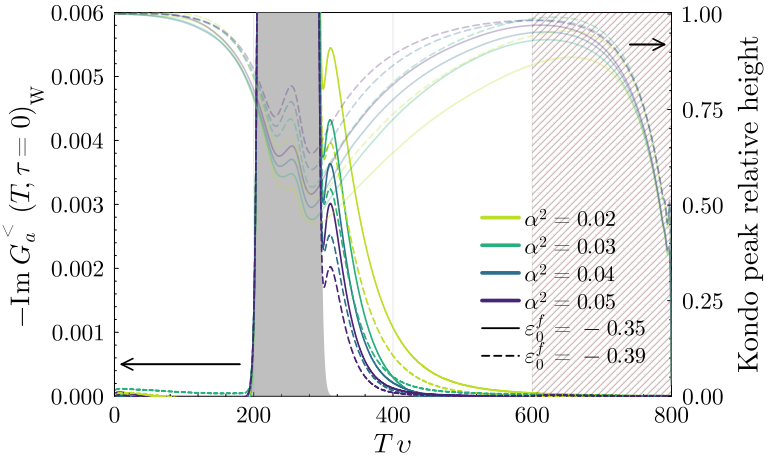

Figure 6.8: Time trace of the renormalised photon pulse as a function of the bath coupling strength α and f electron energy ε_f^0. The time trace of the relative Kondo peak height (unity when the system is in thermal equilibrium with the bath) is juxtaposed. Its drop-off at large times T is related to the lack of points in the relative-time direction to properly resolve the sharp spectral features of Kondo observables (cf. Figure 6.3).

Afterword

The interaction of light with matter is not a new problem. In fact, it is pretty old, going back all the way to the foundations of quantum mechanics, with the theory of blackbody radiation by Max Planck and the photoelectric effect by Albert Einstein. Yet, more than a hundred years after these pioneering works, the problem has transformed itself into countless new ones, re-inventing the world on the way. Motivated by recent experiments [12, 13], one of those problems lies at the intersection of quantum optics and many-body physics – both emerging from the exchange of light quanta with matter – and is the subject matter of this thesis. It is on how Kondo lattice coherence, a delicate many-body effect, is disrupted out-of-equilibrium by a travelling quantum pulse of light. Even though Kondo, non-equilibrium and quantum radiation physics are well-known problems, the theoretical journey was on *how* to properly unite them from first principles. Then, too, from its onset, two technical challenges that ought to be overcome were already known: low temperatures and long timescales had to be resolved for Kondo physics to emerge.

Despite an abundance of different methods in the theoretical condensed-matter toolbox, only a few can take on a Kondo problem – i.e., a strongly-interacting continuum system – driven out-equilibrium. Two-point (Green) functions, generated from non-equilibrium field theory, offer a good trade-off between accuracy – they are perturbative, hence approximate, and system size – the formalism is semi-analytic, which allows transformations and summing over continuous degrees of freedom. This thesis's inaugural application of non-equilibrium field theory techniques is with auxiliary particles, introduced to embed strongly-interacting models, typically non-perturbative, with a perturbative expansion. There were already extensions of auxiliary particles to non-equilibrium field theory at the level of Green functions [65–67]. However, in Chapter 2, this is reformulated in a modern yet comprehensible manner, congruous with their equilibrium formulation. This is particularly important for non-equilibrium problems which start from an equilibrium configuration. First, the main components of the auxiliary particle's non-equilibrium Green function are identified by their "ζ-scaling". Secondly, a connection is established between the Matsubara Green function and the ζ-scaled non-equilibrium Green function components. Finally, a formulation of the components of the non-equilibrium Green function related to thermal observables as a function of real frequencies is obtained, which precludes the use of (numerical) analytic continuation methods.

A significant difficulty in calculating non-equilibrium Green functions – which measure correlations between two points in time – is that general non-equilibrium regimes contain no time symmetries, and the two-point functions are hence dense matrices, of elevated computational cost, in time. In Chapter 3, adaptivity is extended to the two-time integrodifferential solvers of non-equilibrium Green functions. This critical improvement can dynamically adjust the step size to the non-equilibrium regime and dramatically reduce the time-steps required in long-time integrations, allowing Kondo coherence timescales to be reached with a laptop.

In Chapter 4, the centrepiece model of this thesis – which revolves around formalisms and approximations to solve it – is finally brought to light. First, an Anderson lattice model

is expressed with recourse to auxiliary particles due to a non-perturbative interaction term related to the repulsion between neighbouring electrons. Then, the Anderson lattice model is coupled to the electromagnetic field, namely to a time-dependent external quantum pulse of radiation. Furthermore, dissipative channels are introduced to counteract spurious heating from the interaction of the external pulse of light with the system.

The model is solved by two different techniques. First, in Chapter 5, it is solved by non-equilibrium saddle-point theory. The use of the Konstantinov-Perel' contour results in two different sets of equations, one describing an initial thermal state and another describing the dynamical evolution of the auxiliary saddle-point fields, which are known to capture the Kondo coherence in the limit of vanishing temperature. Despite not being discussed in the thesis, the set of equations in thermal equilibrium is obtained via automatic differentiation, which may prove to be a valuable resource for aiding theoreticians in generating saddle-point equations for large systems. The theory, however, ended up being quite limited, as it requires a series of approximations that make it independent of the frequency content of the external pulse. Still, this is not a fundamental limitation of the formalism, and, together with decoherence processes such as those found in open Markovian systems, could be added in further studies. However, the fact the solutions are found in strong-perturbation regimes is unphysical, and some sort of criterion that can gauge whether the saddle-point approximation remains valid throughout the time evolution is yet required to validate the theory. Finally, in Chapter 6, the driven-dissipative Anderson lattice model is solved in its full glory. The generalised formalism of non-equilibrium auxiliary-particle Green functions, introduced in medias res, is employed to treat dynamical mean-field theory and the non-crossing approximation properly. The resulting formulation can reach the low temperatures required for Kondo-coherent regimes, and observables of general physical particles can be computed. Aspects regarding the non-equilibrium mechanisms that collapse and later allow the revival of Kondo coherence, namely enhanced hybridisation and decoherence, are discussed. Moreover, the intensity of the renormalised incident light pulse after interacting with the system is studied as a function of several system parameters. It is shown that the system can emit a non-superradiant echo pulse at low temperatures. The Kondo-related origin of the echo pulses observed in experiments [12, 13] is confirmed, legitimising the theoretical formalism developed for studying future experiments of low-energy pulses of light interacting with many-body systems.

In conclusion, the work presented provides, most importantly, a complete theoretical description of how to tackle non-equilibrium Kondo physics at the level of 2-point functions. It required consolidating several existing ideas and techniques that had to work in unison to resolve the low temperature and long timescales of Kondo physics in non-equilibrium. Theoretical condensed-matter physicists would most likely go extinct if it were possible to solve a strongly-interacting, 3-dimensional, non-equilibrium problem exactly in finite time. In present times, however, things could not be more different. The physics of Kondo coherence melting is a breadbasket of profound and fascinating transient many-body effects which this thesis could only scratch the surface of – hopefully serving as a starting point for future pilgrimages through the beautiful world of non-equilibrium Kondo physics.

Outlook

Prosperous times lay ahead for theoreticians and experimentalists, with the matrimony of the old and vast fields of non-equilibrium and many-body physics. For one, time-resolved terahertz (THz) spectroscopy experiments such as [12–15] will continue delivering access to previously inaccessible physical regimes and unveil the secrets of many-body systems. Second, there is

yet a world of fertile and unexplored physics, with exotic steady or transient non-equilibrium quantum phases harbouring new physics and technological potential.

The most evident and pressing case where a similar analysis to this thesis could be applied, both at the saddle-point [165] or fully-interacting [166] level, is in the study of transients in high-Tc superconductors. Possible research avenues in these systems perfectly capture the possibilities borne by the *pair*ing of non-equilibrium and many-body physics. First, it is possible to probe these systems with electromagnetic radiation to gain insight into the nature of their ground state. Namely, recovering superconductivity dynamics following photo-excitation could give a definite answer to the open question of what is the pairing mechanism, or "glue", which binds electron pairs in high-Tc superconductors. Second, it has also been reported [167] to be possible to either enhance or induce superconductivity with low-frequency pulses at temperatures far above the superconducting critical temperature, which could be technologically significant.

From a numerical standpoint, there are yet two crucial improvements to the adaptive Kadanoff-Baym solver, which could radically slash computation time and memory requirements by orders of magnitude, especially for very long integration times. The first is a direct critique and revision of the adaptive scheme presented in Chapter 3. The stepping scheme is formulated with a *global* time-step in the vertical and centre-of-mass time directions. However, the natural direction for controlling adaptivity is the relative-time direction since Green functions and self-energies typically decay in this direction. For most systems, the Green functions decay in any direction away from the time-diagonal – a signal of loss of correlation over time – however, the relative-time direction is the most natural direction to inspect decay. Therefore, a more refined adaptive algorithm could have a *local* time-step for each relative-time direction. This would significantly increase efficiency by allowing larger time-steps or even stopping the integration in a particular direction if correlations have completely died out. Secondly, a compression scheme similar to [168] could be extended to non-equidistant time grids. The compression scheme was introduced as an alternative representation of the dense two-time grid due to the decay property along the relative-time direction. Extension of the technique to a non-equidistant two-time grid would allow it to be used directly with the developed time-stepper, and implementing a compression similar to the hierarchical mesh of [169] would properly leverage the decay along the relative-time direction.

From a theoretical standpoint, there is yet some work to be resolved. For example, ultrafast THz pulses are somewhat incompatible with the mono-chromatic/narrow-band approximation, i.e., the pulse bandwidth being smaller than the carrier frequency. This approximation greatly simplified the treatment of the external pulse in Chapter 4 as a *single* mode / quantum field but may not yield accurate quantitative results. It would be interesting to see how the results change when many pulse modes are coupled to matter – or an alternative treatment that can consider fast-varying amplitude envelopes. In a similar vein, a DMFT-like formulation of the THz pulse could be formulated for intense pulses, where there could be transient but coherent effects that require temporal correlations to be considered, identical to quantum theories of superfluorescence [170]. Finally, a comparison between the intensity of the output pulse coming from the auxiliary-particle projection and from an ensemble average of jump operators when the input pulse is treated within a Markovian master equation [124, 171] would be of interest, especially regarding the validation of the non-crossing approximation to treat such systems.

Finally, the "holy grail" [172] of Kondo physics would be a conserving approximation that includes the non-local Ruderman–Kittel–Kasuya–Yosida interaction. Given the challenges associated with resolving Kondo physics and adding non-local extensions to DMFT, capturing criticality-induced breakdown of Kondo regimes is a pipedream. However, renormalisation-group theory [11] hints at a feasible introduction of a magnetic-instability channel within a conserving approximation. Such a theory could provide equilibrium and non-equilibrium descriptions of

the breakdown of the Kondo effect in microscopic detail and bring definitive answers to – or, suspecting to be victims of some sort of Poincare recurrence, *revive* [1] once again – the field of "irresistible" [2] physics.

Bibliography

[1] L. Kouwenhoven and L. Glazman, "Revival of the kondo effect", Phys. World **14** (2001).

[2] "Still irresistible", Nature Phys **10** (2014).

[3] W. de Haas, J. de Boer, and G. van dën Berg, "The electrical resistance of gold, copper and lead at low temperatures", Physica **1** (1934).

[4] J. Kondo, "Resistance minimum in dilute magnetic alloys", Prog. Theor. Phys. **32** (1964).

[5] P. Coleman, C. Pépin, Q. Si, and R. Ramazashvili, "How do fermi liquids get heavy and die?", J. Phys.: Condens. Matter **13** (2001).

[6] A. Schröder et al., "Onset of antiferromagnetism in heavy-fermion metals", Nature **407** (2000).

[7] S. Doniach, "The kondo lattice and weak antiferromagnetism", Physica B+C **91** (1977).

[8] S. Seiro et al., "Evolution of the kondo lattice and non-fermi liquid excitations in a heavy-fermion metal", Nat Commun **9** (2018).

[9] I. V. Borzenets et al., "Observation of the kondo screening cloud", Nature **579** (2020).

[10] M. Klein et al., "Signature of quantum criticality in photoemission spectroscopy", Phys. Rev. Lett. **101** (2008).

[11] A. Nejati, K. Ballmann, and J. Kroha, "Kondo destruction in RKKY-coupled kondo lattice and multi-impurity systems", Phys. Rev. Lett. **118** (2017).

[12] C. Wetli et al., "Time-resolved collapse and revival of the kondo state near a quantum phase transition", Nature Phys **14** (2018).

[13] S. Pal et al., "Fermi volume evolution and crystal-field excitations in heavy-fermion compounds probed by time-domain terahertz spectroscopy", Phys. Rev. Lett. **122** (2019).

[14] C.-J. Yang et al., "Terahertz conductivity of heavy-fermion systems from time-resolved spectroscopy", Phys. Rev. Research **2** (2020).

[15] C.-J. Yang et al., *Critical slowing down of fermions near a magnetic quantum phase transition*, 2022.

[16] P. Nordlander, M. Pustilnik, Y. Meir, N. S. Wingreen, and D. C. Langreth, "How long does it take for the kondo effect to develop?", Phys. Rev. Lett. **83** (1999).

[17] J. Kroha and A. Zawadowski, "Nonequilibrium quasiparticle distribution induced by kondo defects", Phys. Rev. Lett. **88** (2002).

[18] A. Rosch, J. Paaske, J. Kroha, and P. Wölfle, "The kondo effect in non-equilibrium quantum dots: perturbative renormalization group", J. Phys. Soc. Jpn. **74** (2005).

[19] R. S. Souto, R. Avriller, A. L. Yeyati, and A. Martín-Rodero, New J. Phys. **20** (2018).

[20] A. Zangwill, "The pope of condensed matter physics", in *A mind over matter* (Oxford University Press, 2021).

[21] P. W. Anderson, "Why do they leave physics?", Physics Today **52** (1999).

[22] C. J. Thompson, "The Gibbs Ensembles and the Thermodynamic Limit", in *Mathematical Statistical Mechanics* (Princeton University Press, 1979).

[23] J. Berges, S. Borsányi, and C. Wetterich, "Prethermalization", Phys. Rev. Lett. **93** (2004).

[24] J. Berges, "Introduction to nonequilibrium quantum field theory", AIP Conf. Proc. **739** (2004).

[25] N. E. Bickers, "Review of techniques in the large-N expansion for dilute magnetic alloys", Rev. Mod. Phys. **59** (1987).

[26] H. Bruus and K. Flensberg, "Linear Response Theory", in *Many-Body Quantum Theory in Condensed Matter Physics: An Introduction* (Oxford University Press, 2004).

[27] R. Kaindl and R. Averitt, "Time-resolved terahertz studies of carrier dynamics in semiconductors, superconductors, and strongly correlated electron materials", in *Optical science and engineering* (CRC Press, 2007).

[28] P. Salén et al., "Matter manipulation with extreme terahertz light: progress in the enabling THz technology", Phys. Rep. **836-837** (2019).

[29] H. J. Carmichael, "Dissipation in Quantum Mechanics: The Master Equation Approach", in *Statistical Methods in Quantum Optics 1: Master Equations and Fokker-Planck Equations* (Springer Berlin Heidelberg, 1999).

[30] P. A. M. Dirac, "Quantum Mechanics of Many-Electron Systems", Proc. R. Soc. Lond. A **123** (1929).

[31] F. Meirinhos, M. Kajan, T. Bode, and J. Kroha, *Auxiliary particles in closed and open systems*, in preparation.

[32] F. Meirinhos, M. Kajan, J. Kroha, and T. Bode, "Adaptive Numerical Solution of Kadanoff-Baym Equations", SciPost Phys. Core **5** (2022).

[33] G. Wilson et al., "Best practices for scientific computing", PLOS Biology **12** (2014).

[34] J. Schwinger, "Brownian motion of a quantum oscillator", J. Math. Phys. **2** (1961).

[35] A. Kamenev, "Introduction", in *Field Theory of Non-Equilibrium Systems* (Cambridge University Press, 2011).

[36] P. Danielewicz, "Quantum theory of nonequilibrium processes, i", Ann. Phys. **152** (1984).

[37] V. Špička, B. Velický, and A. Kalvová, "Electron systems out of equilibrium: nonequilibrium green's function approach", Int. J. Mod. Phys. B **28** (2014).

[38] L. V. Keldysh, "Diagram technique for nonequilibrium processes", Zh. Eksp. Teor. Fiz. **47** (1964).

[39] B. Velický, A. Kalvová, and V. Špička, "Correlated initial condition for an embedded process by time partitioning", Phys. Rev. B **81** (2010).

[40] M. Wagner, "Expansions of nonequilibrium green's functions", Phys. Rev. B **44** (1991).

[41] F. Schwabl, "Equilibrium ensembles", in *Statistical mechanics* (Springer Berlin Heidelberg, 2006).

[42] T. Matsubara, "A new approach to quantum-statistical mechanics", Prog. Theor. Phys. **14** (1955).

[43] G. Stefanucci and R. van Leeuwen, "The contour idea", in *Nonequilibrium many-body theory of quantum systems* (Cambridge University Press, 2013).

[44] V. Morozov and G. Röpke, "The "mixed" green's function approach to quantum kinetics with initial correlations", Ann. Phys. **278** (1999).

[45] M. Garny and M. M. Müller, "Kadanoff-baym equations with non-gaussian initial conditions: the equilibrium limit", Phys. Rev. D **80** (2009).

[46] A. Kamenev, "Bosons", in *Field Theory of Non-Equilibrium Systems* (Cambridge University Press, 2011).

[47] A. Kamenev, "Fermions", in *Field Theory of Non-Equilibrium Systems* (Cambridge University Press, 2011).

[48] H. Aoki et al., "Nonequilibrium dynamical mean-field theory and its applications", Rev. Mod. Phys. **86** (2014).

[49] M. Bonitz, "Correlations and their dynamics", in *Quantum kinetic theory* (Springer International Publishing, 2016).

[50] J. Maciejko, *An Introduction to Nonequilibrium Many-Body Theory*, 2007.

[51] A. Picano, J. Li, and M. Eckstein, "Quantum boltzmann equation for strongly correlated electrons", Phys. Rev. B **104** (2021).

[52] M. J. Hyrkäs, D. Karlsson, and R. van Leeuwen, "Contour calculus for many-particle functions", J. Phys. A **52** (2019).

[53] J. M. Cornwall, R. Jackiw, and E. Tomboulis, "Effective action for composite operators", Phys. Rev. D **10** (1974).

[54] T. Bode, "The two-particle irreducible effective action for classical stochastic processes", J. Phys. A **55** (2022).

[55] M. E. Carrington, "The 4pi effective action for ϕ^4 theory", Eur. Phys. J. C **35** (2004).

[56] G. Baym and L. P. Kadanoff, "Conservation laws and correlation functions", Phys. Rev. **124** (1961).

[57] G. Baym, "Self-consistent approximations in many-body systems", Phys. Rev. **127** (1962).

[58] E. A. Calzetta and B.-L. B. Hu, "Functional methods in nonequilibrium QFT", in *Nonequilibrium Quantum Field Theory* (Cambridge University Press, 2008).

[59] H.T.C.Stoof, K.B.Gubbels, and D.B.M.Dickerscheid, "Gaussian Integrals", in *Ultracold Quantum Fields* (Springer Netherlands, 2009).

[60] K. Fraboulet, "Path-integral approaches to strongly-coupled quantum many-body systems", PhD thesis (Université Paris-Saclay, 2021).

[61] J. Rammer, "Effective action", in *Quantum Field Theory of Non-equilibrium States* (Cambridge University Press, 2007).

[62] A. A. Abrikosov, "Electron scattering on magnetic impurities in metals and anomalous resistivity effects", Physics Physique Fizika **2** (1965).

[63] N. Read and D. M. Newns, "On the solution of the coqblin-schreiffer hamiltonian by the large-n expansion technique", J. Phys. C **16** (1983).

[64] P. Coleman, "New approach to the mixed-valence problem", Phys. Rev. B **29** (1984).

[65] D. C. Langreth and P. Nordlander, "Derivation of a master equation for charge-transfer processes in atom-surface collisions", Phys. Rev. B **43** (1991).

[66] N. S. Wingreen and Y. Meir, "Anderson model out of equilibrium: noncrossing-approximation approach to transport through a quantum dot", Phys. Rev. B **49** (1994).

[67] M. Eckstein and P. Werner, "Nonequilibrium dynamical mean-field calculations based on the noncrossing approximation and its generalizations", Phys. Rev. B **82** (2010).

[68] A. Zawadowski and P. Fazekas, "Dynamics of impurity spin above the kondo temperature", Z. Phys. A **226** (1969).

[69] T. Lappe, "Non-markovian dynamics of open bose-einstein condensates", PhD thesis (Rheinische Friedrich-Wilhelms-Universität Bonn, 2021).

[70] G. Baym and N. D. Mermin, "Determination of thermodynamic green's functions", J. Math. Phys. **2** (1961).

[71] J. Rammer, "Quantum dynamics and Green's functions", in *Quantum Field Theory of Non-equilibrium States* (Cambridge University Press, 2007).

[72] A.-M. Wazwaz, "Fredholm Integral Equations", in *Linear and Nonlinear Integral Equations: Methods and Applications* (Springer Berlin Heidelberg, 2011).

[73] H. Brunner, "A survey of recent advances in the numerical treatment of Volterra integral and integro-differential equations", J. Comp. Appl. Math. **8** (1982).

[74] P. J. van der Houwen and H. J. J. te Riele, "Linear multistep methods for Volterra integral and integro-differential equations", Math. Comp. **45** (1983).

[75] P. J. van der Houwen and H. J. J. te Riele, "Backward differentiation type formulas for Volterra integral equations of the second kind", Numer. Math. **37** (1981).

[76] E. Hairer, S. Norsett, and G. Wanner, "Multistep Methods and General Linear Methods", in *Solving Ordinary Differential Equations I: Nonstiff Problems* (Springer Berlin Heidelberg, 1993).

[77] M. Puig von Friesen, C. Verdozzi, and C.-O. Almbladh, "Kadanoff-Baym dynamics of Hubbard clusters: Performance of many-body schemes, correlation-induced damping and multiple steady and quasi-steady states", Phys. Rev. B **82** (2010).

[78] H. M. Jones and S. McKee, "Variable step size predictor-corrector schemes for second kind volterra integral equations", Math. Comp. **44** (1985).

[79] N. Schlünzen, S. Hermanns, M. Scharnke, and M. Bonitz, "Ultrafast dynamics of strongly correlated fermions — nonequilibrium Green functions and selfenergy approximations", J. Phys.: Condens. Matter **32** (2019).

[80] S. Weinberg, "The Cluster Decomposition Principle", in *The Quantum Theory of Fields*, Vol. 1 (Cambridge University Press, 1995).

[81] T. Banks, "Interacting field theory", in *Modern Quantum Field Theory: A Concise Introduction* (Cambridge University Press, 2008).

[82] J. Berges and J. Cox, "Thermalization of quantum fields from time-reversal invariant evolution equations", Physics Letters B **517** (2001).

[83] M. Schüler, M. Eckstein, and P. Werner, "Truncating the memory time in nonequilibrium dynamical mean field theory calculations", Phys. Rev. B **97** (2018).

[84] N. Schlünzen, J.-P. Joost, and M. Bonitz, "Achieving the scaling limit for nonequilibrium Green functions simulations", Phys. Rev. Lett. **124** (2020).

[85] C. Wetli, "Time-resolved collapse and revival of the kondo state near a quantum phase transition", PhD thesis (ETH Zurich, 2017).

[86] E. Knoesel, A. Hotzel, and M. Wolf, "Ultrafast dynamics of hot electrons and holes in copper: excitation, energy relaxation, and transport effects", Phys. Rev. B **57** (1998).

[87] J. S. Briggs, "A derivation of the time-energy uncertainty relation", J. Phys.: Conf. Ser. **99** (2008).

[88] M. Matsumoto, "Magnetism trends in doped ce-cu intermetallics in the vicinity of quantum criticality: realistic kondo lattice models based on dynamical mean-field theory", Phys. Rev. Materials **4** (2020).

[89] D. Ehm et al., "High-resolution photoemission study on low-T_K ce systems: kondo resonance, crystal field structures, and their temperature dependence", Phys. Rev. B **76** (2007).

[90] O. Gunnarsson and K. Schönhammer, "Double occupancy of the f orbital in the anderson model for ce compounds", Phys. Rev. B **31** (1985).

[91] P. W. Anderson, "Localized magnetic states in metals", Phys. Rev. **124** (1961).

[92] A. J. Millis and P. A. Lee, "Large-orbital-degeneracy expansion for the lattice anderson model", Phys. Rev. B **35** (1987).

[93] C.-I. Kim, Y. Kuramoto, and T. Kasuya, "Self-consistent dynamical theory for the anderson lattice", J. Phys. Soc. Jpn. **59** (1990).

[94] P. Coleman, "Heavy electrons", in *Introduction to Many-Body Physics* (Cambridge University Press, 2015).

[95] K. Kummer et al., "Temperature-independent fermi surface in the kondo lattice $YbRh_2Si_2$", Phys. Rev. X **5** (2015).

[96] F. Anders, "The Kondo Effect", in *Correlated Electrons: From Models to Materials* (Forschungszentrum Jülich, 2012).

[97] O. Dmytruk and M. Schiró, "Gauge fixing for strongly correlated electrons coupled to quantum light", Phys. Rev. B **103** (2021).

[98] R. Loudon, "Quantization of the radiation field", in *The Quantum Theory of Light* (Oxford University Press, 2000).

[99] S. Weinberg, "Electrodynamics", in *The Quantum Theory of Fields*, Vol. 1 (Cambridge University Press, 1995).

[100] J. Skolimowski, A. Amaricci, and M. Fabrizio, "Misuse of the minimal coupling to the electromagnetic field in quantum many-body systems", Phys. Rev. B **101** (2020).

[101] J. Garrison and R. Chiao, "Field quantization", in *Quantum Optics* (Oxford University Press, 2008).

[102] J. Li et al., "Electromagnetic coupling in tight-binding models for strongly correlated light and matter", Phys. Rev. B **101** (2020).

[103] M. O. Scully and M. S. Zubairy, "Atom-field interaction – quantum theory", in *Quantum Optics* (Cambridge University Press, 1997).

[104] A. Amaricci, C. Weber, M. Capone, and G. Kotliar, "Approach to a stationary state in a driven hubbard model coupled to a thermostat", Phys. Rev. B **86** (2012).

[105] H.-P. Breuer and F. Petruccione, "Quantum Master Equations", in *The Theory of Open Quantum Systems* (Oxford University Press, 2007).

[106] C. Gardiner and P. Zoller, "Photon counting", in *Quantum noise* (Springer Berlin Heidelberg, 2004).

[107] H. M. Wiseman and G. J. Milburn, "Open quantum systems", in *Quantum Measurement and Control* (Cambridge University Press, 2009).

[108] P. Werner and M. Eckstein, "Relaxation dynamics of the kondo lattice model", Phys. Rev. B **86** (2012).

[109] L. M. Sieberer, M. Buchhold, and S. Diehl, "Keldysh field theory for driven open quantum systems", Rep. Prog. Phys. **79** (2016).

[110] Y. Murakami, N. Tsuji, M. Eckstein, and P. Werner, "Nonequilibrium steady states and transient dynamics of conventional superconductors under phonon driving", Phys. Rev. B **96** (2017).

[111] F. Peronaci, O. Parcollet, and M. Schiró, "Enhancement of local pairing correlations in periodically driven mott insulators", Phys. Rev. B **101** (2020).

[112] H.-T. Chen, G. Cohen, A. J. Millis, and D. R. Reichman, "Anderson-holstein model in two flavors of the noncrossing approximation", Phys. Rev. B **93** (2016).

[113] M. Eckstein and P. Werner, "Photoinduced states in a mott insulator", Phys. Rev. Lett. **110** (2013).

[114] F. Grandi, J. Li, and M. Eckstein, "Ultrafast mott transition driven by nonlinear electron-phonon interaction", Phys. Rev. B **103** (2021).

[115] J. Demsar, J. L. Sarrao, and A. J. Taylor, "Dynamics of photoexcited quasiparticles in heavy electron compounds", J. Phys.: Condens. Matter **18** (2006).

[116] I. H. Deutsch and J. C. Garrison, "Paraxial quantum propagation", Phys. Rev. A **43** (1991).

[117] K. J. Blow, R. Loudon, S. J. D. Phoenix, and T. J. Shepherd, "Continuum fields in quantum optics", Phys. Rev. A **42** (1990).

[118] L. Ko, R. L. Cook, and K. B. Whaley, "Dynamics of photosynthetic light harvesting systems interacting with N-photon Fock states", J. Chem. Phys. **156** (2022).

[119] A. Silberfarb and I. H. Deutsch, "Continuous measurement with traveling-wave probes", Phys. Rev. A **68** (2003).

[120] C. W. Gardiner and M. J. Collett, "Input and output in damped quantum systems: quantum stochastic differential equations and the master equation", Phys. Rev. A **31** (1985).

[121] A. H. Kiilerich and K. Mølmer, "Input-output theory with quantum pulses", Phys. Rev. Lett. **123** (2019).

[122] J. E. Gough, M. R. James, H. I. Nurdin, and J. Combes, "Quantum filtering for systems driven by fields in single-photon states or superposition of coherent states", Phys. Rev. A **86** (2012).

[123] J. Combes, J. Kerckhoff, and M. Sarovar, "The SLH framework for modeling quantum input-output networks", Adv. Phys. X **2** (2017).

[124] A. H. Kiilerich and K. Mølmer, "Quantum interactions with pulses of radiation", Phys. Rev. A **102** (2020).

[125] Y. Wang, J. ř. Miná ř, L. Sheridan, and V. Scarani, "Efficient excitation of a two-level atom by a single photon in a propagating mode", Phys. Rev. A **83** (2011).

[126] D. Bacon et al., "Universal simulation of markovian quantum dynamics", Phys. Rev. A **64** (2001).

[127] H. Kleinert, "Semiclassical Time Evolution Amplitude", in *Path Integrals in Quantum Mechanics, Statistics, Polymer Physics, and Financial Markets* (World Scientific, 2009).

[128] Z. Sun, M. M. Fogler, D. N. Basov, and A. J. Millis, "Collective modes and terahertz near-field response of superconductors", Phys. Rev. Research **2** (2020).

[129] T. Lappe, A. Posazhennikova, and J. Kroha, "Fluctuation damping of isolated, oscillating bose-einstein condensates", Phys. Rev. A **98** (2018).

[130] J. Kroha and P. Wölfle, "Fermi and Non-Fermi Liquid Behavior of Quantum Impurity Models: A Diagrammatic Pseudo-Particle Approach", in *Theoretical Methods for Strongly Correlated Electrons* (Springer New York, 2004).

[131] R. Frésard, J. Kroha, and P. Wölfle, "The Pseudoparticle Approach to Strongly Correlated Electron Systems", in *Strongly Correlated Systems: Theoretical Methods* (Springer Berlin Heidelberg, 2012).

[132] B. H. Wu and J. C. Cao, "Noise of quantum dots in the ac kondo regime: slave-boson mean-field method and floquet theorem", Phys. Rev. B **77** (2008).

[133] Z. Ratiani and A. Mitra, "$\frac{1}{N}$ Expansion of the nonequilibrium infinite-U anderson model", Phys. Rev. B **79** (2009).

[134] K. Takasan, M. Nakagawa, and N. Kawakami, "Laser-irradiated kondo insulators: controlling the kondo effect and topological phases", Phys. Rev. B **96** (2017).

[135] F. Romeo and R. Citro, "Parasitic pumping currents in an interacting quantum dot", Phys. Rev. B **82** (2010).

[136] E. Arrigoni, C. Castellani, M. Grilli, R. Raimondi, and G. Strinati, "Functional-integral formulation of the slave-boson approach: beyond the mean-field treatment with the correct continuum limit", Phys. Rep. **241** (1994).

[137] P. Coleman, "Mixed valence, fluctuations, and topology", in *Introduction to Many-Body Physics* (Cambridge University Press, 2015).

[138] J. R. Schrieffer and P. A. Wolff, "Relation between the anderson and kondo hamiltonians", Phys. Rev. **149** (1966).

[139] C. Rackauckas and Q. Nie, "Differentialequations.jl–a performant and feature-rich ecosystem for solving differential equations in julia", Journal of Open Research Software **5** (2017).

[140] A. Silberfarb and I. H. Deutsch, "Entanglement generated between a single atom and a laser pulse", Phys. Rev. A **69** (2004).

[141] F. Albarelli, E. Bisketzi, A. Khan, and A. Datta, *Fundamental limits of pulsed quantum light spectroscopy of a two-level atom*, 2022.

[142] O. Scarlatella, A. A. Clerk, R. Fazio, and M. Schiró, "Dynamical mean-field theory for markovian open quantum many-body systems", Phys. Rev. X **11** (2021).

[143] A. Georges, G. Kotliar, W. Krauth, and M. J. Rozenberg, "Dynamical mean-field theory of strongly correlated fermion systems and the limit of infinite dimensions", Rev. Mod. Phys. **68** (1996).

[144] W. Metzner and D. Vollhardt, "Correlated lattice fermions in $d = \infty$ dimensions", Phys. Rev. Lett. **62** (1989).

[145] A. Georges and G. Kotliar, "Hubbard model in infinite dimensions", Phys. Rev. B **45** (1992).

[146] G. Rohringer et al., "Diagrammatic routes to nonlocal correlations beyond dynamical mean field theory", Rev. Mod. Phys. **90** (2018).

[147] P. Schmidt and H. Monien, *Nonequilibrium dynamical mean-field theory of a strongly correlated system*, 2002.

[148] N. Grewe, "A theory for the anderson lattice", Z. Phys. B **67** (1987).

[149] Y. Kuramoto and T. Watanabe, "Theory of momentum-dependent magnetic response in heavy-fermion systems", Physica B+C **148** (1987).

[150] T. Pruschke, D. L. Cox, and M. Jarrell, "Hubbard model at infinite dimensions: thermodynamic and transport properties", Phys. Rev. B **47** (1993).

[151] E. N. Economou, "Green's Functions for Tight-Binding Hamiltonians", in *Green's Functions in Quantum Physics* (Springer Berlin Heidelberg, 2006).

[152] Y. Kuramoto and H. Kojima, "Self-consistent perturbation theory for dynamics of valence fluctuations", Z. Phys. B **57** (1984).

[153] R. O. Jones, "Density functional theory: its origins, rise to prominence, and future", Rev. Mod. Phys. **87** (2015).

[154] A. A. Abrikosov, I. Dzyaloshinskii, L. P. Gorkov, and R. A. Silverman, "Methods of Quantum Field Theory for $T = 0$", in *Methods of Quantum Field Theory in Statistical Physics* (Dover, 1975).

[155] R. Haussmann, "Self-consistent quantum-field theory", in *Self-consistent Quantum Field Theory and Bosonization for Strongly Correlated Electron Systems* (Springer Berlin Heidelberg, 1999).

[156] N. E. Bickers, "Self-Consistent Many-Body Theory for Condensed Matter Systems", in *Theoretical Methods for Strongly Correlated Electrons* (Springer New York, 2004).

[157] H. F. Walker and P. Ni, "Anderson acceleration for fixed-point iterations", SIAM J. Numer. Anal. **49** (2011).

[158] T. A. Costi, J. Kroha, and P. Wölfle, "Spectral properties of the anderson impurity model: comparison of numerical-renormalization-group and noncrossing-approximation results", Phys. Rev. B **53** (1996).

[159] B. Fauseweh and J.-X. Zhu, "Laser pulse driven control of charge and spin order in the two-dimensional kondo lattice", Phys. Rev. B **102** (2020).

[160] W. Zhu, B. Fauseweh, A. Chacon, and J.-X. Zhu, "Ultrafast laser-driven many-body dynamics and kondo coherence collapse", Phys. Rev. B **103** (2021).

[161] S. Kirchner et al., "Colloquium: Heavy-electron quantum criticality and single-particle spectroscopy", Rev. Mod. Phys. **92** (2020).

[162] D. N. Basov, R. D. Averitt, D. van der Marel, M. Dressel, and K. Haule, "Electrodynamics of correlated electron materials", Rev. Mod. Phys. **83** (2011).

[163] K. Cong et al., "Dicke superradiance in solids", J. Opt. Soc. Am. B **33** (2016).

[164] M. G. Benedict, A. M. Ermolaev, V. A. Malyshev, I. V. Sokolov, and E. D. Trifonov, "The elementary theory of super-radiance", in *Super-radiance: Multiatomic Coherent Emission* (CRC Press, 2018).

[165] A. Secchi and M. Polini, "Adiabatic perturbation theory of nonequilibrium light-controlled superconductivity", Phys. Rev. B **98** (2018).

[166] M. A. Sentef, A. F. Kemper, A. Georges, and C. Kollath, "Theory of light-enhanced phonon-mediated superconductivity", Phys. Rev. B **93** (2016).

[167] J. Demsar, "Non-equilibrium phenomena in superconductors probed by femtosecond time-domain spectroscopy", J Low Temp Phys **201** (2020).

[168] J. Kaye and D. Golež, "Low rank compression in the numerical solution of the nonequilibrium Dyson equation", SciPost Phys. **10** (2021).

[169] J. Dölz, H. Egger, and V. Shashkov, "A fast and oblivious matrix compression algorithm for Volterra integral operators", Adv Comput Math **47** (2021).

[170] A. Benediktovitch, V. P. Majety, and N. Rohringer, "Quantum theory of superfluorescence based on two-point correlation functions", Phys. Rev. A **99** (2019).

[171] H. C. H. Chan, O. E. Gamel, G. R. Fleming, and K. B. Whaley, "Single-photon absorption by single photosynthetic light-harvesting complexes", J. Phys. B **51** (2018).

[172] Ammar Nejati, "Quantum Phase Transitions in Multi-Impurity and Lattice Kondo Systems", PhD thesis (Rheinische Friedrich-Wilhelms-Universität Bonn, 2017).